ALMA MATER STUDIORUM · UNIVERSITÀ DI BOLOGNA

Scuola di Scienze
Dipartimento di Fisica e Astronomia
Corso di Laurea Magistrale in Fisica

Study of the Electronic Recoil Background of the XENON1T Experiment

Relatrice:

Prof.ssa Gabriella Sartorelli

Presentata da:
Francesco Toschi

Correlatori:

Dott. Marco Selvi
Dott. Pietro Di Gangi

Anno Accademico 2016/2017

A chi non mi ha mai conosciuto,
ma mi è sempre stato accanto

Abstract

One of the main protagonists of the Dark Matter quest is the XENON Project at the Laboratori Nazionali del Gran Sasso, aiming at the detection of WIMPs interacting with the Xenon nuclei of the detector target. Relying on the experience coming from the previous phases of the project, the current XENON1T detector is the first tonne-scale double-phase TPC, filled with 2 tonnes of Xenon, and it is characterized by the lowest background rates for this kind of experiments. In 2017, with an exposure time of only 34.2 live days, XENON1T set one of the best exclusion limits on the spin-independent WIMP-nucleon interaction cross section. The minimum at $7.7 \cdot 10^{-47}\,\mathrm{cm}^2$ at 90% CL for a 35 GeV/c^2 WIMP mass is currently the lowest cross section ever excluded.

In the first part of this work, I investigate on the possibility that the neutron generator (NG), a neutron calibration source used to characterize the detector response to nuclear recoils (NR), located near the TPC, can be a background source for the detector. By estimating the event rate when the NG is present and when it is not, no difference in the low energy electronic recoil (ER) event rate has been observed. Evaluating the activity of ^{238}U and ^{232}Th in the NG materials it is possible to estimate the expected NR background induced by radiogenic neutrons coming from it: since it is two order of magnitudes lower than what is expected from other materials, it can be considered negligible.

In the last part, an overview of all the ER background sources for the XENON1T detector and its GEANT4 simulation are presented. In particular, the new implementation of the simulation for the double beta decay of ^{136}Xe is discussed. The state-of-art of the matching of Monte Carlo simulations with the real data is shown at the end of the work: the preliminary results show a good knowledge of the ER background in the XENON1T detector.

Sommario

Uno dei principali protagonisti della caccia alla Materia Oscura è il progetto XENON presso i Laboratori Nazionali del Gran Sasso, con l'obiettivo di rivelare l'interazione delle WIMP con i nuclei di xeno che compongono il bersaglio del rivelatore. Forti dell'esperienza proveniente dalle precedenti fasi del progetto, l'attuale rivelatore XENON1T è la prima TPC a doppia fase con una massa attiva superiore alla tonnellata, in quanto contiene 2 tonnellate di xeno liquido, ed è caratterizzato dal più basso livello di background tra tutti gli esperimenti di questo tipo. Nel 2017, con un tempo di esposizione di appena 34.2 giorni, XENON1T ha ottenuto uno dei miglior limiti di esclusione per la sezione d'urto dell'interazione WIMP-nucleo non dipendente dallo spin. Il minimo a $7.7 \cdot 10^{-47}\,\mathrm{cm}^2$ con livello di confidenza al 90% per una WIMP di massa 35 GeV/c^2 è attualmente la sezione d'urto più piccola mai esclusa.

Nella prima parte del presente lavoro di tesi, verifico la possibilità che il neutron generator (NG), una sorgente di neutroni per la calibrazione della risposta del rivelatore ai rinculi nucleari (NR), possa essere una sorgente di background per il detector essendo posizionato vicino alla TPC. Dalla stima del rate di eventi in presenza o meno del NG, nessuna differenza è stata osservata per gli eventi da rinculo elettronico (ER) a bassa energia. Successivamente alla valutazione dell'attività di ^{238}U e ^{232}Th nei materiali del NG, è possibile stimare il background indotto da neutroni radiogenici atteso dal NG: poiché risulta essere due ordini di grandezza inferiore a quanto atteso dai materiali del detector, può essere considerato un contributo trascurabile.

Nella parte finale, tutte le possibili sorgenti di background per eventi ER nel rivelatore di XENON1T e la sua simulazione usando GEANT4 sono presentati. In particolare, la nuova implementazione della simulazione per il doppio decadimento beta dell'isotopo ^{136}Xe è discussa. Lo stato dell'arte del confronto delle simulazioni Monte Carlo con i dati reali è mostato alla fine del lavoro di tesi: i risultati preliminari evidenziano una buona conoscenza dell'ER background nel rivelatore XENON1T.

Contents

Introduction

Humans have been observing and studying the Universe surrounding us for millennia, but only in the last century we became aware that what we can see is just a minimal fraction of it. Since the first measurements of an anomalous distribution of the speed of galaxies in the Coma cluster, carried out by F. Zwicky in the 30's, the need to take into account some missing matter in the Universe has been a fascinating and challenging problem for the entire scientific community.

Nowadays, many evidences of the so-called Dark Matter (DM) have been provided and several theories about its nature have been proposed. Among them, the existence of massive and neutral new particles named WIMPs (Weakly Interacting Massive Particles) is the most promising. The number of experiments hunting for them has grown in the last years, with liquid rare gases detectors heading the search so far. Currently, the XENON1T experiment is the most sensitive experiment for the detection of WIMP interactions with nuclei and it is the first tonne-scale double-phase TPC based on liquid Xenon.

The present work is based on the study of the electronic recoil background in the XENON1T detector and its matching with simulations.

In the first chapter, after a brief description of the origin of the idea of Dark Matter (Sec. 1.1), the astronomical and cosmological evidences of its existence are presented (Sec. 1.2). As these evidences are based on the assumption of General Relativity as the universal gravitational theory, a possible explanation for them may come from the modification of the theory of gravity, as described in Sec. 1.3. Assuming the General Relativity to hold, several possible candidates have been proposed to explain the nature of DM and they are discussed in Sec. 1.4. At the end of the chapter the main current experiments are described. They are based on two different detection techniques: indirect search, relying on the detection of DM annihilation products, and direct search, aiming at detecting DM particles scattering off nuclei. The first are presented in Sec. 1.5, the latter in Sec. 1.6.

In the second chapter, the properties of liquid Xenon as a detection medium are described (Sec. 2.1). Among the liquid Xenon based detectors, the double-phase Time Projection Chamber (TPC) technology has been widely used for the direct search of WIMPs because of its simple scalability and the ability to discriminate between electronic recoils (ER) and nuclear recoils (NR). Its detection principle is described in Sec. 2.2. The first working example of a double-phase TPC with Xenon for DM detection was designed and built during the first phase of the XENON project, XENON10, located at the Laboratori Nazionali del Gran Sasso (LNGS) in Italy. The good results from this first phase led to the XENON100 experiment, as described in Sec. 2.3. The current phase of the XENON Project is represented by the XENON1T detector, the first tonne-scale double-phase TPC ever built. After only 34 live days of data taking, the collaboration published the most stringent exclusion limits on the spin-independent WIMP-nucleon interaction cross section for WIMP masses above 10 GeV/c^2. An overview of the experiment and of its first results is given in Sec. 2.4. The near future upgrade XENONnT is presented in Sec. 2.5.

The third chapter is dedicated to the study of the background induced by the presence of the neutron generator (NG), deployed close to the XENON1T TPC. The NG is a D-D fusion chamber used as neutron source for NR calibration: its working principle is described in Sec. 3.1. Since it was displaced close to the TPC not only for calibration runs, but also during Dark Matter search data taking, it is necessary to know its influence on the total background. In Sec. 3.2 the contribution to the low energy ER background coming from the NG is shown to be negligible, as the difference between the event rate when the NG was deployed and when it was not is compatible with zero. Radioactive chains in the materials making up the NG can produce neutrons via spontaneous fission or (α, n) reactions. The contribution of radiogenic neutrons coming from the NG to the NR background is shown in Sec. 3.3: after estimating the activity of the main radioactive chains (^{238}U and ^{232}Th), the neutron background from NG is estimated to be less than two orders of magnitude lower than what expected from the other materials. Therefore the NG is excluded to be a dangerous background source for both electronic and nuclear recoils. The high energy γ ray peaks in the spectrum are used to estimate the Thorium and Uranium activities and also to study the charge and light yield stability over time, as shown in Appendix A.

In the fourth and final chapter, the comparison between the observed ER spectrum and the Monte Carlo (MC) simulations is presented and the preliminary results are shown. The GEANT4 implementation of the XENON1T detector is briefly described in Sec. 4.1. All the possible sources of ER background to be taken into account for the simulation and the comparison are discussed in Sec. 4.2. In particular, details about the simulation of the double beta decay are given in Sec. 4.3, as ^{136}Xe is an intrinsic double beta emitter. A dedicated code was developed and integrated with GEANT4 to simulate the correct spectrum of the electronic pair produced by the decay. At the end, the matching between the MC simulations and the real data is shown in Sec. 4.4 and the preliminary results are presented.

The results achieved in this work are summarized in the conclusion and they are discussed in the context of the background study of the XENON1T detector.

Chapter 1

The Dark Matter problem

Dark Matter (DM) has been representing one of the main problems of modern Physics and Cosmology in the last century. Since the first observations of the Coma cluster carried out by F. Zwicky during the 30's [1], considered the first proof of the DM existence, many different evidences of its existence have been found. Among them the leading examples are represented by anomalous rotational curves of spiral galaxies, CMB anisotropies and lensing effects.

Many hypothesis have been proposed to explain the DM nature: nowadays, the most viable candidates come from extensions of the Standard Model (SM), as no known particle has the characteristics to account for it. Such candidates are known as *Weakly Interacting Massive Particles* (WIMPs): they are non-baryonic massive particles interacting only via gravitational and weak interactions. The most quoted example of WIMP is the lightest particle coming from the supersymmetric extension of the SM, the *neutralino*. Along with these hypotheses, many alternative theories have been developed to explain the astronomical observations by modifying Newtonian dynamics or General Relativity, without the need of introducing any new particle.

In the last years several experiments have been designed aiming at detecting and discovering elusive DM. These experiments are based on different detection principles and their joint contribution allows to explore the DM properties.

1.1 Prehistory of Dark Matter

In its most general meaning, astronomers refer to Dark Matter to describe the matter in the Universe which can be detected only by its gravitational effects. The father of this term is the French mathematician and physicist Henri Poincaré who used the words *matière obscure* discussing Lord Kelvin's description of the Milky Way in terms of molecular dynamics during one of his Baltimore Lectures at the beginning of XX century [2]. He established a simple relation between the size of the system, therefore its mass, and the dispersion speed of the stars in it. In order to do it, he thought Milky Way as a monoatomic gas applying molecular dynamics theory to the motion of stars within. In view of a possible difference between the visible mass and the inferred one based on this theory, he proposed that "*many of our stars, perhaps a great majority of them, may be dark bodies*" [3]. Even if Poincaré was impressed by the idea of applying molecular dynamics to study the structure of Milky Way, he rejected the existence of such "dark bodies". He pointed out that the mass inferred by Lord Kelvin and the observed one were of the same order of magnitude, therefore the discrepancy was not enough to require the presence of unobserved mass.

One of the most important examples of dark object identified by its gravitational effects on a visible body is the discovery of Neptune. In order to explain the anomalies of Uranus' orbit, Urbain Le Verrier and Couch Adams independently proposed in 1864 the existence of a new outer planet. Le Verrier's calculation were so precise that astronomers were able to identify Neptune within 1 degree of the predicted position the same evening they received the letter with the results from the French astronomer [4]. Later, Le Verrier tried to explain the anomalous precession of Mercury's perihelion by introducing a new perturbing planet he called "Vulcan". Unlike the previous case, no such planet was found: this anomaly was not due to an unobserved object, but it was a hint to a new universal theory of gravitation, the General Relativity.

1.2 Observational evidences

Since the beginning of the last century, astronomical observations have been providing strong evidences for the presence of DM on different scales: from the rotational curves of galaxies up to the CMB anisotropies. While effects on galaxies or clusters may reveal the spatial distribution of DM, cosmological evidences coming from CMB show the fraction of it in the energy-mass composition of the Universe.

1.2.1 The Coma cluster

The first hint of Dark Matter existence comes from the observations carried out by the Swiss astronomer Fritz Zwicky during the 30's: he noticed that the speed of galaxies inside the Coma cluster was not consistent with the

Figure 1.1: NASA/ESA Hubble Space Telescope picture of the Coma cluster, one of the densest known galaxy collection in the Universe.

gravitational stability given by its visible mass.

A galaxy cluster is a set of galaxies bounded together because of their own gravitational attraction. Zwicky studied the motion of galaxies inside 9 different clusters [1] inferring their speed by measuring the redshift of their spectra: for each cluster he obtained a mean value and by the speed dispersion he was able to determine the mean speed of galaxies inside a single cluster. He focused on the 45 million light years distant Coma cluster (Fig. 1.1), the biggest of his study with more than 800 galaxies making up the system. The speed spread of galaxies inside the Coma cluster was up to 2000 km/s, a high value if compared to its center of mass moving at 7500 km/s. Since Zwicky knew the mean square speed of galaxies inside the cluster along the line of sight, he was able to derive the total mean square speed and by applying the *virial theorem* he deduced the mass of the cluster [5]. As he measured the luminosity of the cluster, he compared the mass-to-light ratio of the Coma cluster to the one of the local Kapteyn stellar system: the former was more than two orders of magnitude lager than the latter. Zwicky introduced the presence of DM to explain this strong discrepancy and to account for the high speed of the galaxies inside a cluster with such a low visible mass.

Virial theorem

A galaxy cluster is made up by N galaxies. Using the center of mass frame, each galaxy σ is defined by its mass M_σ and position $\vec{r}_\sigma$. The law of motion for each galaxy is given by

$$M_\sigma \frac{d^2\vec{r}_\sigma}{dt^2} = \vec{F}_\sigma, \tag{1.1}$$

where $\vec{F}_\sigma$ is the total force acting on the galaxy σ. Scalar multiplication of (1.1) with $\vec{r}_\sigma$ and summing over all galaxies gives

$$\frac{1}{2}\frac{d}{dt^2}\Theta = \sum_{\sigma=1}^{N} \vec{r}_\sigma \cdot \vec{F}_\sigma + \sum_{\sigma=1}^{N} M_\sigma \left(\frac{d\vec{r}_\sigma}{dt}\right)^2 , \tag{1.2}$$

where $\Theta = \sum_{\sigma=1}^{N} M_\sigma r_\sigma^2$ is the total moment of inertia of the galaxy cluster, $V = \sum_{\sigma=1}^{N} \vec{r}_\sigma \cdot \vec{F}_\sigma$ is the virial of the cluster and the last term is twice its kinetic energy $K = \frac{1}{2}\sum_{\sigma=1}^{N} M_\sigma \left(\frac{d\vec{r}_\sigma}{dt}\right)^2$ [5]. If the cluster is stationary its polar moment of inertia fluctuates around a constant value Θ_0: by averaging Eq. (1.2) over time its derivative cancels out and it becomes

$$\langle V \rangle = -2\langle K \rangle. \tag{1.3}$$

For power-law forces like Newton's inverse square law, the time average of the virial is equal to the total potential energy of the system $\langle V \rangle = \langle U \rangle$ and so the virial theorem is

$$\langle K \rangle = -\frac{1}{2}\langle U \rangle. \tag{1.4}$$

Modeling the considered cluster as a uniform spherical distribution with total mass $\mathcal{M}$ and radius R, the mean potential energy is $\langle U \rangle = -\frac{3}{5}G_N\frac{\mathcal{M}^2}{R}$ and the kinetic energy $\langle K \rangle = \frac{1}{2}\mathcal{M}\langle\langle v^2 \rangle\rangle$, where the double averaging is over time and over all the galaxies of the cluster. Therefore, the cluster mass derived from the virial theorem is

$$\mathcal{M} = \frac{3}{5}\frac{\langle\langle v^2 \rangle\rangle R}{G_N}. \tag{1.5}$$

For the Coma cluster $R = 2\times 10^{24}$ cm and $\langle\langle v^2 \rangle\rangle = 1.5\times 10^{16}\ \mathrm{cm}^2/\mathrm{s}^2$ the total mass is roughly $\mathcal{M}_{VT} = 10^{14}M_\odot$. The derived value is strongly inconsistent with the mass inferred by the cluster's luminosity $\mathcal{M}_L = 10^{12}M_\odot$.

1.2.2 Spiral galaxies' rotation curve

After Zwicky's discovery, new issues concerning spiral galaxies' rotation curves arose: several observations pointed out a slow decreasing of the rotation speed of stars with radial distance, slower than Newtonian predictions. Nevertheless, in the years following Zwicky's discovery there was not any sense of crisis among astronomers and the Coma cluster discrepancy was thought to be due to an underestimation of the mass-to-light ratio of elliptical galaxies [6]. Moreover, the techniques used to measure the rotation speed of stars inside galaxies were affected by huge uncertainties and this led astronomers

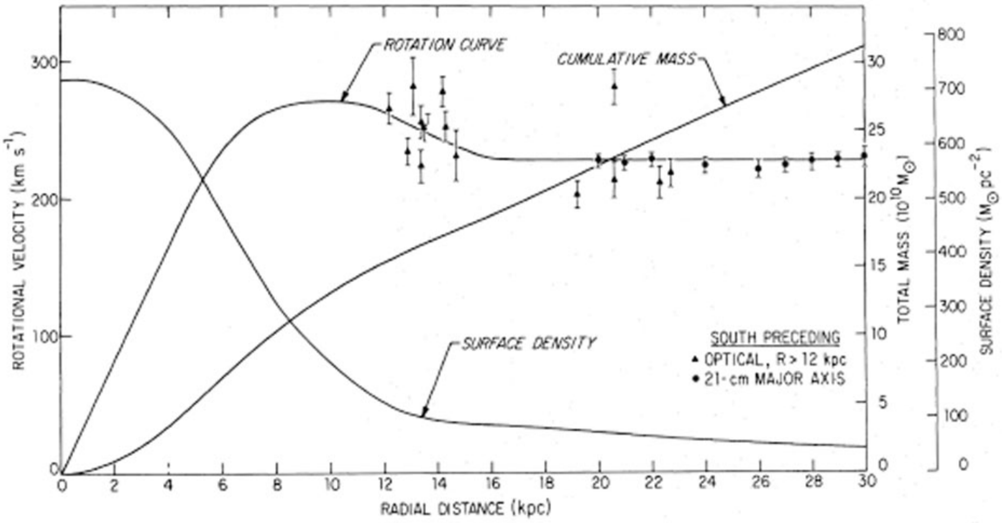

Figure 1.2: Andromeda rotation curve measured using the HI 21 cm line [8]. The constant trend for higher radius is one of the main evidences for the existence of DM.

into considering these discrepancies not alarming as more accurate observations were thought to be the solution to the problems.

By 1970 radioastronomy had emerged as a major tool for exploring galactic and extra-galactic phenomena. This new field allowed astronomers to have a precise measurement of galaxies' rotation curves by measuring the Doppler shift of the 21 cm line of neutral hydrogen (HI). This emission line comes from the spin-flip transition of the electron between the two hyperfine levels of the hydrogen 1s ground state: both the abundance of neutral hydrogen and its high penetrating power makes this signal a better choice than traditional optical observations [7].

The turning point in DM history comes from the combined measurements of the *Andromeda* spiral galaxy (M31) carried out by Rubin and Ford [9] in the optical region and by Roberts and Whitehurst [8] observing the 21 cm hydrogen line. The former allowed a precise measurement of the rotation speed of stars in the optical inner part of the galaxy, while the latter extended the observation to the outer non-optical region. Both the techniques confirmed a constant rotation speed for stars as the distance from the galactic center increases, as shown in Fig. 1.2. By modeling a spiral galaxy as an inner massive bulge and an outer flattened disk, the mass distribution $M(r)$ is constant for radii lager than the bulge's radius and the Newtonian dynamic predicts a decreasing trend for the rotation curve:

$$v(r) = \sqrt{\frac{G_N M(r)}{r}} \propto r^{-1/2} \, (r > R_{\text{bulge}}) \, . \tag{1.6}$$

This result is inconsistent with the observed constant speed for stars far away from the galactic bulge: this would require a mass density profile $\rho(r) \propto r^{-2}$ outside the core

$$M(r) = 4\pi \int_0^r \rho(x) x^2 dx \propto r \qquad \Rightarrow \qquad v(r) \propto \text{const.} \tag{1.7}$$

Such a mass density distribution could be explained by assuming that galaxies are enveloped in *dark halos* expanding far beyond the luminous matter distribution and whose effects dominate the outer region of the galaxies. The existence of a dark halo had been already proposed by Ostriker and Peebles [10] during the 70's to explain the stability of spiral galaxies. Indeed, numerical N-bodies simulations showed that these structures could not be stable just because of their own gravitational field [11]. The most famous and used density distribution for halos of cold DM is the Navarro-Frenk-White (NFW) profile [12]:

$$\rho(r) = \frac{\rho_s}{\frac{r}{r_s}\left(1 + \frac{r}{r_s}\right)^2}, \tag{1.8}$$

where ρ_s is the characteristic density and r_s the halo scale radius varying galaxy by galaxy.

1.2.3 Bullet cluster

A strong but controversial evidence for DM comes from the study of the Bullet cluster (1E 0657-558), shown in Fig. 1.3a. It consists of a smaller galaxy subcluster acting as a bullet passing through a bigger cluster: in this collision stars and gas act differently. Stars are just slowed down by the gravitational pull, while gas of the colliding clusters interact electromagnetically, slowing down with a huge emission of X-rays. This radiation can be measured and used to trace the baryonic mass distribution of the colliding subclusters. The evidence for the existence of DM lies in the fact that the gravitational field, mapped using the weak gravitational lensing effect described in Section 1.4.1, is separated from the baryonic mass distribution: the former is almost coincident with the galaxies distribution [13]. Since galaxies cannot account for most of the mass in the cluster, a possible explanation comes from the

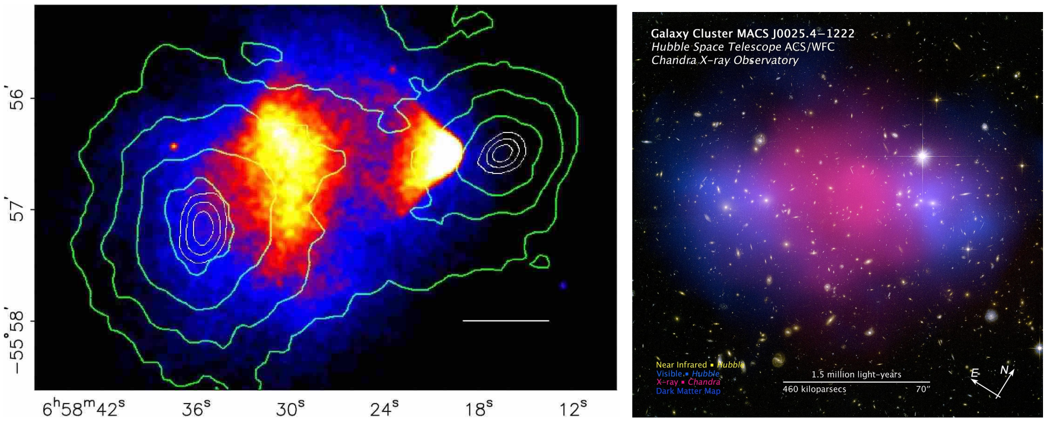

(a) **(b)**

Figure 1.3: (a) X-ray image of the Bullet cluster from the Chandra X-ray Observatory showing the baryonic matter distribution. The green lines represent the contour of the mass distribution inferred by weak gravitational lensing techniques. The displacement between the distribution could be explained by the presence of DM. (b) MACS J0025.4-1222 shows the same feature of the Bullet cluster. X-ray distribution is shown in pink, while mass distribution is in blue.

presence of DM: its low interacting power let DM halos to pass through each other without being disturbed along their path. Bullet cluster is not the only one with such feature: Fig. 1.3b shows a similar cluster from the Massive Cluster Survey (MACS) called MACS J0025.4-1222, where the baryonic mass distribution and the gravitational field are well separated.

The controversy about this evidence comes from numerical simulations of the Bullet cluster: accepting the ΛCDM cosmological model described in Section 1.4.2, the results are in disagreement with the observations [14]. Simulations show that Bullet cluster is an unlikely event for a cold DM dominated Universe since the necessary colliding speed to account for the X-ray emission is far higher than what expected in a ΛCDM scenario. These results are still subject of a fervent discussion as more precise simulations are available.

1.2.4 Cosmic Microwave Background

In 1964 Arno Penzias and Robert Woodrow Wilson detected a $\sim 3\,\mathrm{K}$ microwave background filling the space with no defined source [15]: this is the *Cosmic Microwave Background* (CMB) and it represents the remnant of the Big Bang. It consists of relic photons from the early Universe stage at which photons decoupled with matter and the Universe became transparent, when

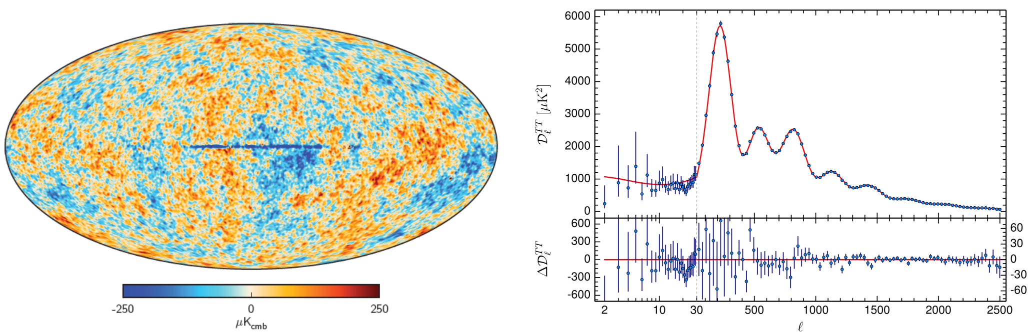

(a) **(b)**

Figure 1.4: (a) CMB map as measured by the Planck space observatory (2015). (b) Power angular spectrum of the CMB: on the y-axis the value $\mathcal{D}_\ell^{TT} = \ell(\ell+1)C_\ell/2\pi$ is given as a function of ℓ.

temperature dropped to about 3000 K. This discovery was a landmark evidence for the Big Bang theory of an inflationary Universe, since it shows the expected black-body spectrum. The Steady State theory, the main alternative to the Big Bang, was not able to explain this spectrum and it was discarded.

The CMB is a highly isotropic background radiation with an almost perfect black-body spectrum with temperature $T_0 = 2.72548 \pm 0.00057\,\mathrm{K}$, as given by combined results from COBE/FIRAS and WMAP [16]. As the measurements got more and more precise, CMB temperature map showed little variations: these anisotropies give fundamental information on the origin of the Universe and its composition. They are quantum fluctuations stretched to cosmic scale during the inflationary exponential expansion: variations in the CMB are given by the combined effect of gravitational pull, radiation pressure and gravitational redshift. During the early stage of the Universe, quantum fluctuations of the primordial photon-baryon fluid yielded to density fluctuations: matter was pulled towards these higher density regions causing the formation of gravitational potential wells and hills. These were the seed of large scale structures we see in the Universe today. A higher density region corresponds to a hotter one: the matter pulled inside the potential wells by gravity feels a stronger radiation pressure and this leads to a temperature increase. Nowadays, the most accurate measurements of such anisotropies are given by the ESA space observatory Planck with a resolution $\Delta T/T \sim 10^{-6}$: the 2015 map is shown in Fig. 1.4a. Most of the cosmological parameters come from decomposing the temperature fluctuation map into spherical harmonics $Y_{\ell,m}(\theta,\phi)$:

$$\frac{\delta T}{\langle T\rangle}(\theta,\phi) := \frac{T(\theta,\phi)-\langle T\rangle}{\langle T\rangle} = \sum_{\ell=0}^{+\infty}\sum_{m=-\ell}^{+\ell} a_{\ell,m} Y_{\ell,m}(\theta,\phi)\,. \tag{1.9}$$

Cosmological parameters can be inferred by the *power spectrum* of the CMB (see Fig. 1.4b), defined by the coefficients

$$C_\ell := \frac{1}{2\ell+1}\sum_{m=-\ell}^{+\ell} a_{\ell,m}^2. \tag{1.10}$$

The value ℓ is linked to the angular separation between two points: a high ℓ value corresponds to a little angular separation ($\theta \approx 60°/\ell$) and, therefore, it gives information about the CMB local behavior. Analyzing the power spectrum as ℓ varies, we have information about the early stage of the Universe:

- $\ell = 0$ (monopole term) represents the average of the temperature fluctuations and it is null;
- $\ell = 1$ (dipole term) is not interesting to a cosmological level since its main contribution is given by the Doppler effect due to the motion of our Galaxy with respect to the CMB reference frame;
- $\ell \lesssim 10$ gives information about CMB at large scale and it is dominated by the Sachs-Wolfe effect [17]. Photons escaping from high density regions have a higher frequency since temperature is higher, but they are affected by the gravitational redshift as well. This effect dominates the power spectrum at large scales, acting as a white noise since it reflects the random fluctuations of the primordial Universe;
- $\ell \gtrsim 30$ shows peaks as a consequence of *acoustic oscillations* and it allows to infer the abundance of DM, baryonic mass and dark energy in the Universe by fitting these peaks to the cosmological ΛCDM framework. As matter is pulled inside potential wells, radiation pressure starts to push baryonic matter out while DM keeps on collecting inside them, causing acoustic oscillations to propagate through the medium. Potential wells get deeper as both baryonic and dark matter get pulled inside, while radiation pressure pushes out only baryonic matter: this combined action gives rise to the power spectrum peaks.

The evidence for the existence of DM comes from the agreement of the ΛCDM model fit with the experimental data as shown in Fig. 1.4b: the red line shows the fit of the model to the data. Size and position of the peaks give valuable pieces of information about the energy-matter distribution of the Universe. The density parameters $\Omega_i = \rho_i/\rho_0$, with ρ_0 the critic density for a flat Universe, are measured thanks to the Planck observatory [18, 19]:

$$\begin{aligned}\Omega_\Lambda &= 0.6844 \pm 0.0091\\ \Omega_\mathrm{m} &= 0.3156 \pm 0.0091\\ \Omega_\mathrm{b} h^2 &= 0.02225 \pm 0.00016\\ \Omega_\mathrm{DM} h^2 &= 0.1198 \pm 0.0015\end{aligned}$$

where the subscript Λ stands for dark energy, m for total matter, b for baryonic matter and DM for Dark Matter and h is the reduced Hubble constant $h \equiv H_0/\left(100\,\mathrm{km\,s^{-1}\,Mpc^{-1}}\right)$ with $H_0 = 67.27 \pm 0.66\,\mathrm{km\,s^{-1}\,Mpc^{-1}}$. This means that the present Universe is roughly composed by dark energy for 68%, DM for 27% and by ordinary matter for the left 5%.

Dark energy was introduced for the first time by Einstein in his field equation as a constant source term Λ, known as *cosmological constant*, in order to explain the accelerated expansion of the Universe and its flatness. Indeed, Edwin Hubble in 1929 showed that the galaxies are moving away from us with a speed proportional to their distance [20], proving that our Universe is expanding. The introduction of a new constant term in the Einstein field equation is equivalent to introduce a vacuum mass or energy, either positive or negative.

1.3 Alternatives to Dark Matter

Evidences described so far have a common ground as they all accept General Relativity (GR) and Newton's law as its weak field limit to be the description of gravitational interaction. These theories have been proved only on small scales as planetary orbits, but they are just supposed to hold on galactic and extra-galactic scales. As this assumption is dropped the observed anomalies may be described in terms of a new gravitational theory, without requiring the existence of DM.

1.3.1 Modified gravity theories

From MOND to TeVeS

The first strong alternative theory was proposed in 1982 by the Israeli physicist Mordehai Milgrom [21]: he proposed that Newtonian dynamics does not apply to objects with very low accelerations. In order to explain galactic rotation curves and the lack of visible mass in galaxy clusters, he proposed a *Modified Newtonian Dynamics* (MOND) by introducing a preferred acceleration scale $a_0 \sim 10^{-8}\,\mathrm{cm/s}^2$. According to the MOND theory, the modified second law of dynamics is:

$$m\tilde{\mu}\left(a/a_0\right)\vec{a} = -\vec{\nabla}\Phi, \tag{1.11}$$

where Φ is the gravitational potential and $\tilde{\mu}(x)$ includes the preferred acceleration scale keeping Newton's second law valid for high accelerations, as $\tilde{\mu}(x) \approx 1$ for $|x| \gg 1$ and $\tilde{\mu}(x) \approx x$ for $|x| \ll 1$.

Using the same scale a_0, the MOND theory can explain both the clusters' mass problem and the galactic rotation curves: using the MOND analogue of the virial theorem, the mass discrepancy for clusters softens, but does not fully resolve as they still seem to contain a factor 2-3 more matter than observed [22]. Constant galactic rotation curve is a straight consequence of Milgrom's theory [23], since for low acceleration:

$$\frac{a^2}{a_0} \approx \frac{G_N M(r)}{r^2} \Rightarrow a \approx \frac{\sqrt{G_N M(r) a_0}}{r} \Rightarrow v \approx \left(G_N M(r) a_0\right)^{1/4}. \tag{1.12}$$

A straightforward relativistic formulation of MOND theory turns out to require a superluminal propagation of a new scalar field ϕ. In order to avoid this problem, Bekenstein proposed a relativistic theory called TeVeS (Tensor-Vector-Scalar) [24]. Unlike GR, which describes gravity in terms of a metric tensor $g_{\alpha\beta}$, TeVeS theory introduces three different fields: the Bekenstein metric $\tilde{g}_{\alpha\beta}$, a scalar field ϕ and the Sanders vector field A_α. This theory is covariant as it is based on a covariant action and it reduces to MOND theory in the weak field limit, in the same way GR reduces to Newton's law.

$f(R)$ gravity

$f(R)$ gravity is a family of modified gravity theories generalizing GR: each theory is defined by a different function f of the Ricci scalar R, also known as the curvature of the space-time manifold [25]. These theories come from relaxing the hypothesis that the Hilbert-Einstein action for the gravitational field is strictly linear in the Ricci scalar, generalizing it to

$$\mathcal{S}[g] \propto \int f(R)\sqrt{-g}\, d^4x \tag{1.13}$$

where $f(R) = R$ returns Einstein's theory. A convenient selection of this function may lead to an alternative explanation of the DM evidences, but with the drawback of a scale and time dependent gravitational constant G_N.

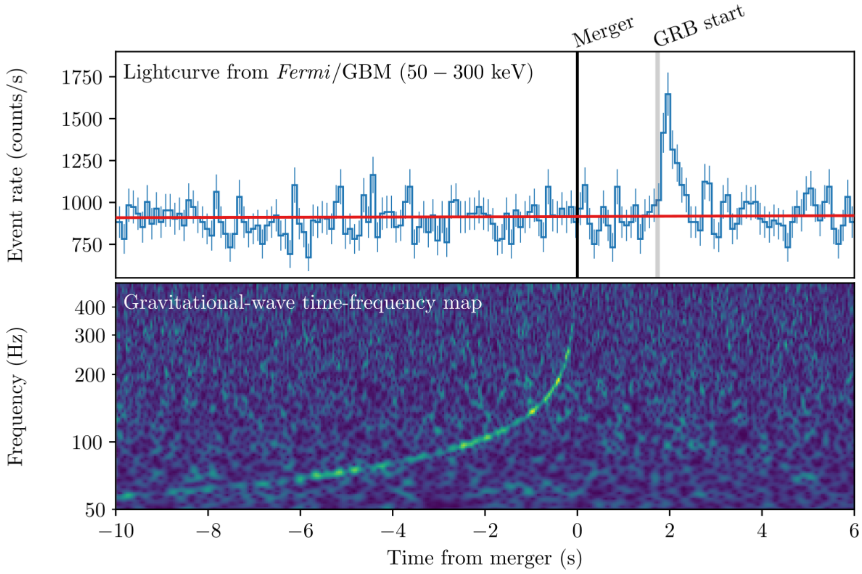

Figure 1.5: The bottom plot shows the GW170817A signal detected by the LIGO-Virgo interferometers array. The top plot shows the gamma ray burst GRB170817A detected by the Fermi/GBM telescope within an interval $\Delta t \approx 1.7\,\mathrm{s}$

Emergent gravity

One of the most recent alternative theories was proposed by the Dutch theoretical physicist Erik Verlinde: he proposes that gravity is not fundamental, but it is an entropic force, consequence of the increasing entropy linked to the information associated to mass in space, as we assume the holographic principle[1] [26]. Verlinde's theory can explain several anomalies such as galactic rotation curves or clusters' mass discrepancy, without introducing DM as for a low acceleration regime this theory returns a gravitational force varying inversely with the distance. Observation of more than 30 thousands galaxies using weak gravitational lensing shows a good agreement with emergent gravity despite requiring no free parameters to be fine-tuned [27].

1.3.2 Modified gravity after GW170817A

The LIGO-Virgo interferometers detected a gravitational wave (GW) coming from the coalescence of a binary neutron star on 17th August 2017, dubbed GW170817A [28]. This event was the first GW with an observed electromagnetic counterpart: the Fermi Gamma-ray Burst Monitor observed a short

---

[1] In quantum gravity the *holographic principle* states that the information contained in a volume can be encoded on its boundary surface.

γ-ray burst (GRB170817A) about 1.7 seconds after the LIGO-Virgo's detection [29], as shown in Fig. 1.5. The GW source was observed throughout the entire electromagnetic spectrum in the days following 17$^{\text{th}}$ August and it was possible to locate its position 40 Mpc from the Milky Way, in the NGC 4993 galaxy. This simultaneous observation provides the first ever test of Einstein's Weak Equivalence Principle (WEP) between gravitons and photons: the little time delay between GW's and photons' detection implies a little difference between the Saphiro delay for light and for gravitational waves. The *Saphiro delay* is defined as the delay in the carrier's propagation due to the non-zero gravitational potential of cumulative mass distribution along the line of sight. Therefore the fact that light and GW have the same Saphiro delay implies they are subject to the same potential.

The simultaneity of gravitational and electromagnetic signals rules out a whole class of modified theories of gravity, known as *Dark Matter emulators*, like TeVeS [30]. These theories state that ordinary matter couples to the metric $\tilde{g}_{\mu\nu}$, while GWs couple to the metric $g_{\mu\nu}$: the former corresponds to the GR metric with DM, the latter to the GR metric with only baryonic matter. Assuming GWs couple to $g_{\mu\nu}$ and light couples to $\tilde{g}_{\mu\nu}$, the Saphiro delay due only to the DM in the Milky Way along the line of sight between the Earth and NGC 4993 would be $\sim$1000 days. This conclusion immediately rules out DM emulators as the observed time delay $\Delta t \approx 1.7\,\text{s}$ is 10 orders of magnitude lower.

1.4 Dark Matter candidates

Assuming GR as the universal theory describing gravity, the evidences described so far have to be explained by introducing new matter we cannot observe. The lack of observations may be due to its low brightness or to the fact that this new matter does not interact electromagnetically: this latter hypothesis requires the introduction of new particles since no SM particle matches all DM characteristics. Indeed, a good DM candidate has to be massive, neutral and it should not interact through strong or electromagnetic interaction: neutrinos are the only SM particles matching all of those properties, but they would lead to a relativistic DM, ruled out by simulations of the formation of large scale structures in the Universe. Several Beyond Standard Model (BSM) theories offer suitable DM candidates not only to solve the missing mass problem in the observable Universe, but also as solution to other SM problems such as the naturalness of the Higgs boson's mass or the strong CP problem.

(a) (b)

Figure 1.6: (a) The galaxy cluster SDSS J1038+4849 bends the light coming from distant galaxies into arc-like shapes: the resulting image looks like a smiling face. (b) An elliptical galaxy acts as a strong gravitational lens producing four images of the G2237 +0305 quasar behind it.

1.4.1 Baryonic candidates: MACHOs

The existence of baryonic DM is a fact, as the discovery of Uranus clearly shows: since our instruments are not infinitely sensible it is impossible to observe faint sources such as exoplanets or brown dwarfs from distant galaxies. This implies that at least a fraction of the missing halo matter consists of massive faint celestial bodies known as MACHOs (*MAssive Compact Halo Objects*) which contribute to gravitational effects but cannot be observed. The principal examples of MACHOs consist of brown dwarfs with a mass $M < 0.08M_{\odot}$, cold stars, molecular hydrogen H_2 clouds and primordial black holes, formed during the high-density and inhomogeneous phase of the early Universe. By definition they cannot be observed using traditional telescopes: the only way to detect them is to observe their effect on other luminous sources.

As the light travels from a source to the observer it can be bent by the presence of a mass distribution stretching the space-time. This deflection can lead to a *gravitational lensing* effect if the source, the mass and the observer are roughly aligned: this effect may distort the observed image into ring- or arc-like shapes in case of high masses as shown in Fig. 1.6, otherwise it may cause a variation of the luminosity. The latter case is known as gravitational *microlensing* effect. A mass sitting along the line of sight of a luminous

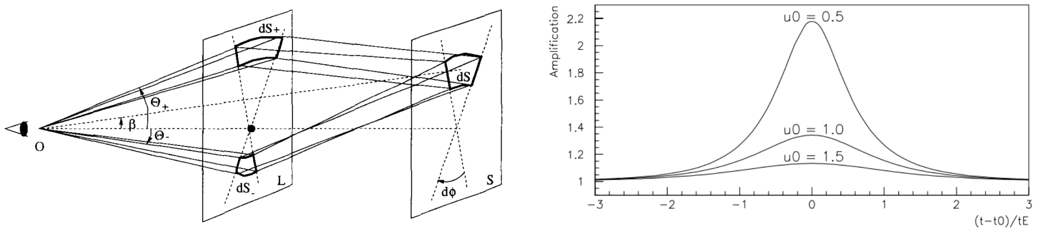

(a) **(b)**

Figure 1.7: (a) Light rays from a surface element dS in presence of a point-like lens: its corresponding surfaces in the lens plane are $dS_{\pm}$. (b) Luminosity amplification A as a function of time for a point-like lens, where $u_0 = \beta(0)/\theta_E$ and $t_E^2 = v_\perp^2/\theta_E D_O^2$.

source can act as a convergent lens, increasing the observed luminosity of the source for a variable period of time. The amplification of the flux is due to the increasing of the bright area caused by the deflection. Given an observer O, a light source S and the lensing mass l sitting between the observer and the source with a distance $D_O = \overline{Ol}$ and $D_S = \overline{Sl}$, it is possible to compute the flux amplification as the ratio of the observed solid angle and the corresponding one in absence of lenses [31]:

$$A = \frac{d\Omega}{d\Omega_0}. \tag{1.14}$$

Considering the case of a point-like lens, a source with angular position $\vec{\beta}$ has two images with angular positions

$$\theta_{\pm} = \frac{\beta}{2} \pm \theta_E \sqrt{1 + \frac{\beta^2}{4\theta_E^2}}, \tag{1.15}$$

where $\theta_E = \sqrt{\frac{4G_N M}{c^2} \frac{D_S}{D_S D_O}}$ is known as Einstein angle and it is the observed angular position of an object when a lensing mass is exactly along the line of sight between the source and the observer. As illustrated in Fig. 1.7a a source element dS subtending a solid angle $d\Omega_0 = dS/D_O^2 = \beta d\phi d\beta$ is observed subtending a solid angle $d\Omega_{\pm} = dS_{\pm}/D_O^2 = \theta_{\pm} d\phi d\theta_{\pm}$. Hence the amplification of each image in θ_+ and θ_- can be written as

$$A_{\pm} = \frac{d\Omega}{d\Omega_0} = \frac{\theta_{\pm} d\theta_{\pm}}{\beta d\beta} = \frac{1}{2} \pm \frac{\beta^2 + 2\theta_E^2}{2\beta\sqrt{\beta^2 + 4\theta_E^2}}, \tag{1.16}$$

where Eq. (1.15) was used. If it is not possible to resolve the two images the total amplification will be:

$$A = A_+ + |A_-| = \frac{\beta^2 + 2\theta_E^2}{\beta\sqrt{\beta^2 + 4\theta_E^2}}. \tag{1.17}$$

As the lens moves between the source and the observer, this effect is time dependent and assuming a constant velocity with respect to the line of sight one has

$$\beta^2(t) = \frac{b^2 + [v_\perp (t - t_0)]^2}{\theta_E D_O^2} \tag{1.18}$$

where b is the impact parameter, i.e. the minimum distance between the lens trajectory and the light source. Combining Eqs. (1.17) and (1.18), it leads to a time dependence of the luminosity of the observed source as shown in Fig. 1.7b.

The EROS experiment (Expérience pour la Recherche d'Objets Sombres in La Silla, Chile) used the microlensing techniques to estimate the fraction of baryonic DM as MACHOs in the Milky Way's halo. They observed more than 30 million stars of the Large and Small Magellanic Clouds (LMC and SMC), monitoring their luminosity over a period longer than 6 years. Using a sample of 7 millions bright stars, only one candidate event was found, whereas about 39 events were expected if the dark halo had been entirely populated by objects of mass $M \sim 0.4 M_\odot$, setting an upper limit on the baryonic composition of DM to 8% [32]. This observations ruled out MACHOs in the mass range $6 \cdot 10^{-8} < M/M_\odot < 15$ as primary occupant of the Milky Way's dark halo, confirming the non-baryonic nature of DM and, therefore, the need to explain the missing mass in term of BSM particles.

1.4.2 Non-baryonic particle Dark Matter

As DM represents an important fraction of the entire energy-mass composition of the Universe, its nature has influenced the formation and evolution of its structures. For this reason large-scale universal structures may reflect the properties of DM. The formation of large-scale structures is caused by quantum fluctuations, growing up to galaxy-sized objects during the Inflation era: as DM decouples from cosmological fluid, it interacts only via gravitational interaction gathering in potential wells. While DM keeps on accumulating forming "dark" structures, the photon-baryon fluid oscillates inside these wells as a consequence of radiation pressure, causing baryonic fluctuations. As soon as baryons and photons decouples the latter are free to stream and they make up the CMB we observe today, while the former feels the gravitational pull of DM gathering and forming the Universe structures.

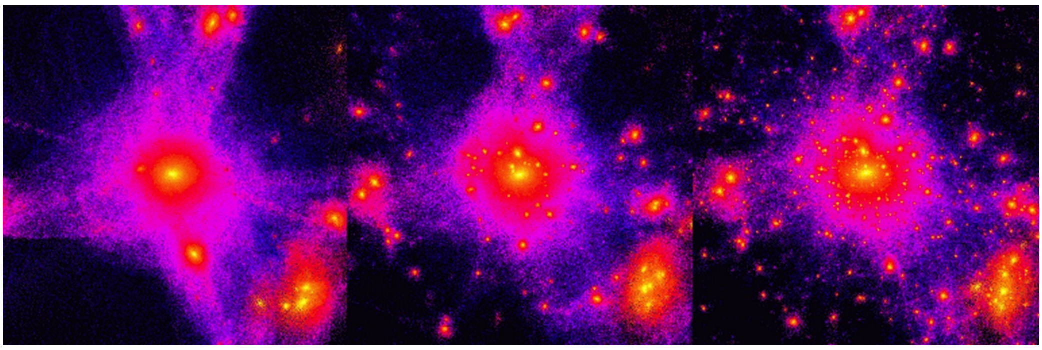

Figure 1.8: Simulations of what structure in Hot (left), Warm (middle), and Cold (right) DM universes would look like at present time (z=0). The best agreement with observations is achieved with CDM simulation. Simulation by Ben Moore, University of Zurich.

In this simplified picture the dispersion speed of DM plays a fundamental role: the faster DM particles move after decoupling from cosmological fluid, the more spread the primordial structures are. Indeed, the DM could be classified based on its dispersion speed into three main types:

- **Hot Dark Matter** (HDM) if it slows down to non-relativistic speed after the decoupling from photon-baryonic fluid. In this case the structure formation is described by a *top-down* model, where the matter collects first into pancake-like shapes and then it fragments into smaller units [33]. This model has several flaws, in fact the evolution of primordial galaxies is too slow compared to the observed Universe. HDM particles are characterized by a small mass: the most natural candidates for this kind of DM are massive relic neutrinos forming the Cosmic Neutrino Background (CνB) [34, 35]. Even a little mass for the three families could be sufficient to account for a flat Universe ($\Omega_0 = 1$), as the neutrinos' fraction of the total density is given by $\Omega_\nu h^2 = \sum_{i=1}^{3} \frac{m_i}{93\,\mathrm{eV}}$. The last results from Planck observatory set an upper limit on the sum of the neutrinos' masses to $\sum_{i=1}^{3} m_i \leqslant 0.23$ eV, ruling out this hypothesis;

- **Cold Dark Matter** (CDM) if it slows down to non-relativistic velocities before the decoupling. In this case the density fluctuations lead to a *bottom-up* model for the formation of structures: they grow hierarchically, with small objects collapsing under their self-gravity first and merging or clustering to form larger and more massive objects. Since CDM is slower, it is more likely composed by massive particles: no SM particle matches these characteristics. Nowadays, this hypothesis is considered to be the most viable as numerous numerical N-body simulations show an excellent agreement with the observed distribution of matter in the Universe, e.g. Millennium Simulation with more than 10^{10} particles in a cubic region with about $2 \cdot 10^9$ light years for side [36]. This difference is shown in Fig. 1.8: HDM requires a longer time to resemble the current Universe, while results from CDM simulations agree with present observations;

- **Warm Dark Matter** (WDM) has intermediate properties between those of HDM and CDM, leading to a formation model which is top-down for smaller structures and bottom-up for large ones. The best candidate of WDM is the *sterile neutrino*, an hypothetical particle interacting only via gravitational interaction: this is the right-handed neutrino ν_R and could explain the neutrino's mass required to account for the oscillation phenomenon [37].

Numerical simulations of the large-scale structures and studies on CMB led scientific community to consider ΛCDM model as the standard model for Cosmology, based on Einstein's GR. The main ingredients of this theory are an inflationary expansion of the Universe during its early stages, the existence of Dark Energy opposing to gravitational attraction allowing the expansion of the Universe and the presence of Cold DM: the latter is characterized by being dissipationless, i.e. it can not cool by radiating photons, and almost collisionless as it interacts only via gravitational and maybe weak interaction.

Possible BSM candidates for CDM are briefly discussed in the following.

1.4.3 Axions

These particles come from a possible solution of the so-called *strong CP problem*: strong interaction described by QCD does not seem to break CP symmetry the way electroweak interaction does, as decay of neutral kaons K^0_L and K^0_S shows [38]. In the SM there are no apparent reasons why QCD should not violate CP symmetry while weak interaction does. The SM explanation for such violation is the presence of the imaginary phase δ_{13} in the CKM matrix, mixing the quarks' weak eigenstates into mass eigenstates: this absolute phase leads to an observable phase difference between a physical state and its CP-conjugate. A similar mechanism that could break strong CP symmetry is introducing a natural term in the QCD lagrangian:

$$\mathcal{L}_\mathrm{QCD} \supset \theta \frac{g_s^2}{64\pi} \epsilon^{\mu\nu\alpha\beta} G^a_{\mu\nu} G^a_{\alpha\beta}, \tag{1.19}$$

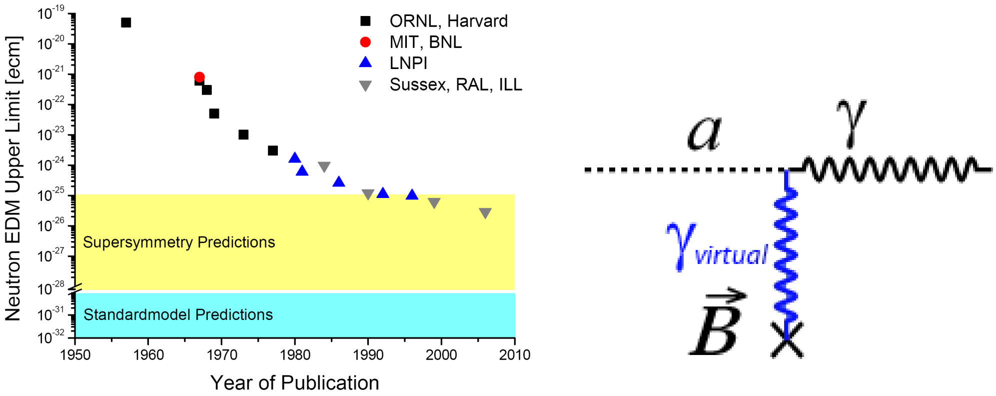

(a) **(b)**

Figure 1.9: (a) Neutron EDM experimental upper limit in the last years: yellow region represents predictions coming from supersymmetric theories, blue region represents the SM prediction of about $d_n^{\mathrm{SM}} \approx 10^{-31} e\mathrm{cm}$. (b) Primakoff effect: the axion interacts with a magnetic field (virtual photon) turning into a real photon. The experimental searches are based on this effect.

where g_s is the strong coupling. The measurement of neutron's electric dipole moment (nEDM) set the strongest constraints on strong CP symmetry violation: including the term (1.19) its theoretical value is $d_n \sim 5 \cdot 10^{-16} \theta\, e\mathrm{cm}$ [39], but recent experiments set an upper limit $d_n^{\mathrm{sup}} = 3 \cdot 10^{-26} e\mathrm{cm}$ [40], as shown in Fig. 1.9a. This constrains θ to an upper value of about 10^{-10}, leading to a naturalness problem.

In 1977 Peccei and Quinn proposed a possible solution to this problem [41]. They postulated the existence of a global $U(1)_{\mathrm{PQ}}$ chiral symmetry which is spontaneously broken: the associated Nambu-Goldstone boson is called axion and it transforms under this symmetry as $a\,(x) \to a\,(x) + \alpha f_a$ where f_a is the order parameter associated with the breaking of $U(1)_{\mathrm{PQ}}$. In this way it is possible to dynamically set θ to zero removing the CP violating term, but non-perturbative QCD effects lead to a massive Nambu-Goldstone boson with the mass given by [42]:

$$m_a = 0.6\,\mathrm{eV} \frac{10^7\,\mathrm{GeV/c^2}}{f_a} \tag{1.20}$$

constrained by numerical simulations between $5 \cdot 10^{-5}$ eV and $1.5 \cdot 10^{-3}$ eV. The small mass and the weak interaction with ordinary matter make axions a good candidate for CDM.

Of particular interest for axion DM searches is the axion coupling with two photons:

$$\mathcal{L}_{a\gamma\gamma} = -\frac{\alpha_{\mathrm{EM}} g_\gamma}{\pi f_a} a\,(x)\,\vec{\mathrm{E}} \cdot \vec{\mathrm{B}} = -g_{a\gamma\gamma} a\,(x)\,\vec{\mathrm{E}} \cdot \vec{\mathrm{B}} \tag{1.21}$$

with g_γ a model dependent constant of order 1. Experimental searches for axions exploit thi effect, called *Primakoff effect*, relying on this coupling to detect this theoretical particles: axions interacting with a strong magnetic field can turn into photons as shown in Fig. 1.9b, showing up as an excess of intensity.

The CAST experiment (CERN Axion Solar Telescope) looks for axions produced inside the Sun as result of photons turning into axions because of an inverse process than the one shown in Fig. 1.9b. It consists of a 9.26 m long decomissioned LHC magnet capable of producing a field of up to 9.5 T: it set one of the best upper limit $g_{a\gamma\gamma} < 6.6 \cdot 10^{-11}$ GeV^{-1} [43]. The current best limit on axion-photons coupling comes from XENON100 experiment with $g_{a\gamma\gamma} < 7.7 \cdot 10^{-12}$ GeV^{-1} [44].

1.4.4 Supersymmetric Dark Matter

Supersymmetric theory (SUSY) is the most popular extension of the SM as it solves the fine-tuning problem of the Higgs' boson mass: introducing a supersymmetric partner for every particle of the SM, the Higgs' self-energy loops cancel out as each fermionic contribution is removed by its supersymmetric bosonic contribution [45]. Supersymmetry is a group of global transformations linking femionic states to bosonic states by means of fermionic generators $Q|f\rangle = |b\rangle$ and $Q^\dagger|b\rangle = |f\rangle$. Since it is a space-time symmetry, it is defined by irreducible representations called supermultiplets consisting of a SM particle and its supersymmetric partner with the same quantum numbers except for the spin, differing for a half unit.

This theoretical framework requires the introduction of many new particles with masses around $1 \div 10\,\mathrm{TeV/c^2}$, as higher masses would not account for the Higgs' boson naturalness problem. In this new particles' zoo there are several good candidates as non-baryonic CDM particles: they are called WIMPs (Weakly Interacting Massive Particles, χ) and they need to be stable, massive and coupling only via gravitational and weak interactions. The general definition of WIMPs does not imply them to be supersymmetric particles. Unlike axions, these DM candidates do not come out from a specific theory but any massive BSM particle satisfying all the DM characteristics and in a mass range $10 \div 10^3$ GeV/c^2 could be a WIMP.

WIMP miracle

The great interest in WIMPs comes from the fact that they are supposed to have the right relic density for CDM, once the thermal equilibrium in the early Universe is assumed. During the early stage of the Universe, WIMPs and SM particles were in equilibrium as pairs production and annihilation $\chi\bar{\chi} \rightleftarrows \ell^+\ell^-$, $q\bar{q}$, ... were equally likely to happen because temperature was much higher than WIMP mass ($T \gg m_\chi$). The common rate for production/annihilation is given by

$$\Gamma_{\text{ann}} = \langle\sigma_{\text{ann}} v\rangle n_{\text{eq}}, \tag{1.22}$$

where brackets denote the cross section average over the WIMP speed distribution and n_{eq} is the WIMP number density in equilibrium. As the Universe expands, the temperature of the plasma drops becoming smaller than the WIMP mass ($T < m_\chi$): the chemical equilibrium ceases, as annihilation processes are more likely to happen than pair production, hence the number of WIMPs decreases with the Boltzmann factor $e^{-m_\chi/T}$. At the same time the density of WIMP n_χ decreases as the Universe is expanding and it leads to a decreasing rate Γ_{ann}. As the annihilation rate becomes smaller than the expansion rate of the Universe, the WIMP abundance "freezes out", resulting in the current relic abundance. The WIMP number density follows the Boltzmann equation

$$\frac{dn_\chi}{dt} + 3Hn_\chi = -\langle\sigma_{\text{ann}} v\rangle \left(n_\chi^2 - n_{\text{eq}}^2\right), \tag{1.23}$$

where the equilibrium density follows a Maxwellian distribution in temperature. An approximate solution considering the freeze-out time at $T = m_\chi/20$ leads to a mass independent WIMP relic abundance

$$\Omega_\chi h^2 \approx \frac{3 \cdot 10^{-27}\text{cm}^3\text{s}^{-1}}{\langle\sigma_{\text{ann}} v\rangle}. \tag{1.24}$$

Comparing this result with the Planck 2015 observations $\Omega_\chi h^2 \approx 0.12$, the annihilation thermal average cross section is $\langle\sigma_{\text{ann}} v\rangle \sim 10^{-26}\text{cm}^3\text{s}^{-1}$: this value is similar to the one obtained by considering a weak interacting massive particle. This coincidence is called *WIMP miracle* and has provided a strong motivation for the search for WIMPs: a weak interacting massive particle in thermal equilibrium in the early Universe leads to the same relic abundance required by the current ΛCDM model and observations.

SM	**MSSM**	$\mathrm{SU(3)_C}$, $\mathrm{SU(2)_L}$, $\mathrm{U(1)_Y}$	**SM**	**MSSM**	$\mathrm{SU(3)_C}$, $\mathrm{SU(2)_L}$, $\mathrm{U(1)_Y}$
$\begin{pmatrix} q_u \\ q_d \end{pmatrix}_{\mathrm{L}}$	$\begin{pmatrix} \tilde{q}_u \\ \tilde{q}_d \end{pmatrix}_{\mathrm{L}}$	$(\mathbf{3},\ \mathbf{2},\ 1/3)$	g	$\tilde{g}$	$(\mathbf{8},\ \mathbf{1},\ 0)$
$(q_u)_{\mathrm{R}}$	$(\tilde{q}_u)_{\mathrm{R}}$	$(\mathbf{3},\ \mathbf{1},\ -4/3)$	$W^{\pm}$, W^0	$\tilde{W}^{\pm}$, $\tilde{W}^0$	$(\mathbf{1},\ \mathbf{3},\ 0)$
$(q_d)_{\mathrm{R}}$	$(\tilde{q}_d)_{\mathrm{R}}$	$(\mathbf{3},\ \mathbf{1},\ 2/3)$	B	$\tilde{B}$	$(\mathbf{1},\ \mathbf{1},\ 0)$
$\begin{pmatrix} \nu \\ \ell \end{pmatrix}_{\mathrm{L}}$	$\begin{pmatrix} \tilde{\nu} \\ \tilde{\ell} \end{pmatrix}_{\mathrm{L}}$	$(\mathbf{1},\ \mathbf{2},\ -1)$	$\begin{pmatrix} H_u^+ \\ H_u^0 \end{pmatrix}$	$\begin{pmatrix} \tilde{H}_u^+ \\ \tilde{H}_u^0 \end{pmatrix}$	$(\mathbf{1},\ \mathbf{2},\ 1)$
$(\ell)_{\mathrm{R}}$	$(\tilde{\ell})_{\mathrm{R}}$	$(\mathbf{1},\ \mathbf{1},\ 2)$	$\begin{pmatrix} H_d^0 \\ H_d^- \end{pmatrix}$	$\begin{pmatrix} \tilde{H}_d^0 \\ \tilde{H}_d^- \end{pmatrix}$	$(\mathbf{1},\ \mathbf{2},\ -1)$

Table 1.1: MSSM chiral and vector supermultiplets: hypercharge and non-abelian symmetry group representations (in bold) are shown.

The Minimal Supersymmetric Standard Model

The supersymmetric extension of SM minimizing BSM Physics is known as MSSM (Minimal Supersymmetric Standard Model): the internal symmetry group is $\mathrm{SU(3)_C} \times \mathrm{SU(2)_L} \times \mathrm{U(1)_Y}$ and the number of new particles is minimal as no new gauge boson is introduced [46]. In MSSM each supermultiplet couples a SM particle with its supersymmetric partner, defined sparticle: fermionic leptons with scalar bosons *sleptons* and vector gauge bosons with fermionic *gauginos*. Higgs' sector has to be modified: MSSM requires two scalar complex Higgs' bosons doublets, each one coupled with a fermionic supersymmetric partner named *higgsino*.

In the MSSM lagrangian it is possible to find terms violating the conservation of leptonic or baryonic number, L and B. A direct consequence is the decay of the proton ($\Delta B = -1$, $\Delta L = 1$) with a lifetime up to few years, in contrast with the upper limit imposed by Super-Kamiokande collaboration $\tau\left(p \to e^+ \pi^0\right) > 1.6 \cdot 10^{34}$ y [47]. This evidence requires to manually introduce a discrete $\mathbb{Z}_2$ symmetry known as $\mathcal{R}$-parity leading the conservation of the multiplicative quantum number

$$\mathcal{R} = (-1)^{3B+L+2s} \tag{1.25}$$

and therefore particles and sparticles will have different $\mathcal{R}$-values: $\mathcal{R}(\mathrm{p}) = +1$ and $\mathcal{R}(\tilde{\mathrm{p}}) = -1$. This conservation immediately implies that every MSSM vertex needs to have an even number of sparticles: $e^+e^- \to \mu^+\tilde{\mu}^-$ is not allowed, while $e^+e^- \to \tilde{\mu}^+\tilde{\mu}^-$ is.

Neutralinos

Since $\mathcal{R}$-parity forbids vertices with an odd number of sparticles, the Lightest Supersymmetric Particle (LSP) needs to be stable. Moreover, the fact that

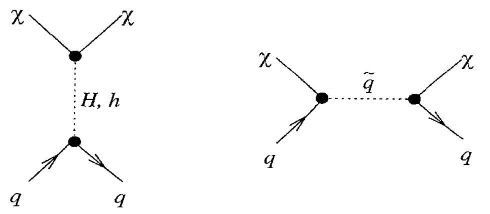

Figure 1.10: Feynman diagrams contributing to the SI neutralino-quark elastic scattering

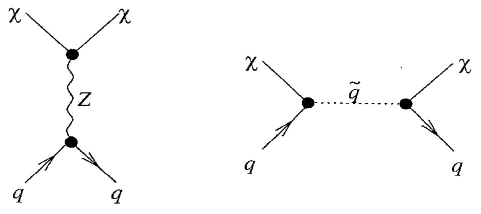

Figure 1.11: Feynman diagrams contributing to the SD neutralino-quark elastic scattering

no supersymmetric particles have been detected yet implies that the LSP has to be massive and neutral, interacting only via weak and gravitational interaction. This makes the LSP the best supersymmetric candidate for WIMP.

In the MSSM the main candidate for LSP is the lightest *neutralino*, a mix of the neutral supersymmetric fermions bino $\tilde{B}$, wino $\tilde{W}^0$ and higgsinos $\tilde{H}_u^0$ and $\tilde{H}_d^0$. This mixing is caused by the fact that the non null VEV (Vacuum Expectation Value) implies that electroweak eigenstates differ from Majorana mass eigenstates[2], therefore the observable particles should be a linear combination of them. In this way the observable mass eigenstates are the four neutralinos whose lightest is the best WIMP candidate:

$$\chi_1 = \mathbb{N}_{11}\tilde{B} + \mathbb{N}_{12}\tilde{W}^0 + \mathbb{N}_{13}\tilde{H}_d^0 + \mathbb{N}_{14}\tilde{H}_u^0. \tag{1.26}$$

By assuming this particle to be the WIMP, the cosmological abundance requires this neutralino to be “gaugino-like” ($|\mathbb{N}_{11}|^2 \sim 1$) with a more likely coupling to fermions [48].

In this scenario, neutralino’s most interesting interactions are annihilation and elastic scattering with nucleons, since indirect and direct detection techniques are based on them. In case of elastic scattering there are two types of interaction: spin-independent (SI) and spin-dependent (SD), described by a scalar and axial interaction [49]. In the first case the scatter of a neutralino with a quark is expressed as

$$\mathcal{L}_{\text{scalar}} = a_q \bar{\chi}\chi\bar{q}q, \tag{1.27}$$

with a_q the coupling. Hence the total cross section will be

$$\sigma_{\text{SI}} = \frac{4\mu_{\text{N}}}{\pi}\left[Zf_p + (A-Z)\,f_n\right]^2, \tag{1.28}$$

---

[2] Since gauginos and higgsinos are fermions with two degrees of freedom as their bosonic counterparts, the only way they can have mass is by introducing a Majorana mass term in the lagrangian.

where μ_N is the reduced mass and f_i $(i = p, n)$ is the coupling to the considered nucleons, based on its quark composition. Eq. (1.28) holds under the zero transfer momentum condition: as this condition is no longer satisfied it is necessary to introduce a nuclear form factor $F_{\mathrm{N}}(q)$. Since in most theories WIMP coupling to neutrons and protons is very similar $(f_n \approx f_p)$ it is possible to write the total cross section (1.28) as

$$\sigma_{\mathrm{SI}} = \frac{4\mu_{\mathrm{N}}}{\pi} A^2 f_n^2. \tag{1.29}$$

The SD WIMP-nucleus interaction arises from couplings of the WIMP field to the quark axial current $\bar{q}\gamma_\mu\gamma_5 q$, described by the lagrangian

$$\mathcal{L}_{\mathrm{A}} = d_q \bar{\chi}\gamma^\mu\gamma_5\chi\bar{q}\gamma_\mu\gamma_5 q, \tag{1.30}$$

with d_q the generic axial coupling. Because of the axial nature of the coupling the resulting cross section will depend on the total angular momentum of the nucleus $\sigma_{\mathrm{SD}} \propto J(J+1)$ and it can be observed only using $J \neq 0$ nuclei [50].

1.4.5 Other candidates

Even if WIMP and axions represent the most popular candidates for DM particles, there are many other hypotheses on the nature of CDM [51]. The thermal equilibrium scenario for WIMP during the freeze-out implies an upper limit on its mass of $m_\chi < 340\,\mathrm{TeV/c^2}$ [52], lowered to $m_\chi \lesssim 34\,\mathrm{TeV/c^2}$ with new data on CMB. Dropping the thermal equilibrium hypothesis it is possible to identify a new class of DM candidates known as *wimpzillas* with a high mass $m_{\mathrm{DM}} > 10^{10}\,\mathrm{GeV/c^2}$. Among the possible ways to produce such particles in the early Universe, the most studied is the gravitational production: wimpzillas are produced during the transition from the inflationary phase to a matter-radiation dominated phase. A common motivation for superheavy DM comes from the observation of cosmic rays with energy above the GZK cutoff ($\sim 5 \cdot 10^{19}\,\mathrm{eV}$): such particles may explain these extremely energetic events as due to their decay or annihilation in a top-down model [53].

In 1921 Kaluza proposed the idea that electromagnetism could be unified with gravity by including the gauge field in the metric tensor: this required to add *extra dimensions* to the 3+1 observed [54]. In this scenario the space-time is a 3+1 dimensional brane which is embedded in a 3+1+δ dimensional space-time called bulk. A general feature of extra-dimensional theories is that upon compactification of the extra dimensions all of the fields propagating in the bulk have their momentum quantized in units of $p \sim 1/R^2$, where R is the curvature of the compactified dimensions. The result is that a series of Kaluza-Klein (KK) states appears and it is seen in the ordinary space-time as a series of particles with masses $m_n = n/R$, where n labels the mode number. In these theories the Lightest KK Particle (LKP) needs to be stable as the KK number conservation is a direct consequence of the momentum conservation, therefore it represents a possible candidate for CDM with a high mass $m_{\mathrm{KK}} \sim 800\,\mathrm{GeV/c^2}$. Because of the heavy nature of these particles only tonne-scale detectors can probe this possibility.

1.5 Indirect search

In the last decades the search for particle DM has been one of the most challenging and active field of experimental Physics, with a growing number of new experiments based on different techniques. One of the most important family of DM detectors is based on *indirect detection*: these experiments look for signals coming from the annihilation of WIMPs in the form of SM particles, like high energy photons or neutrinos. In the following the three main types of indirect search experiments are briefly discussed.

1.5.1 High-energy solar neutrinos

As the Solar System moves through the dark halo of the Milky Way, WIMPs are swept up by the Sun: they occasionally loose energy scattering with nuclei in the Sun and they eventually get gravitationally bound [49]. WIMPs in the core of the Sun can annihilate, producing high energy neutrinos, as annihilation products can be heavy quarks, gauge bosons or neutrinos themselves. Compared to other DM detection techniques, indirect search using solar neutrinos involves minimal astrophysical uncertainty: the equilibrium between WIMPs' annihilation and capture due to the long Sun's lifetime allows to average out all the astrophysical inputs, like DM velocity distribution or its local density.

IceCube

IceCube is a cubic-kilometer neutrino detector installed in the ice at the geographic South Pole, between depths 1450 m and 2450 m [56]. The reconstruction of neutrinos relies on the detection of Čerenkov light emitted by secondary particles produced in neutrinos interactions with the medium. Photons are detected by optical modules named DOMs (Digital Optical Modules), each one housing a 25 cm diameter PMT and a digitizer board. They

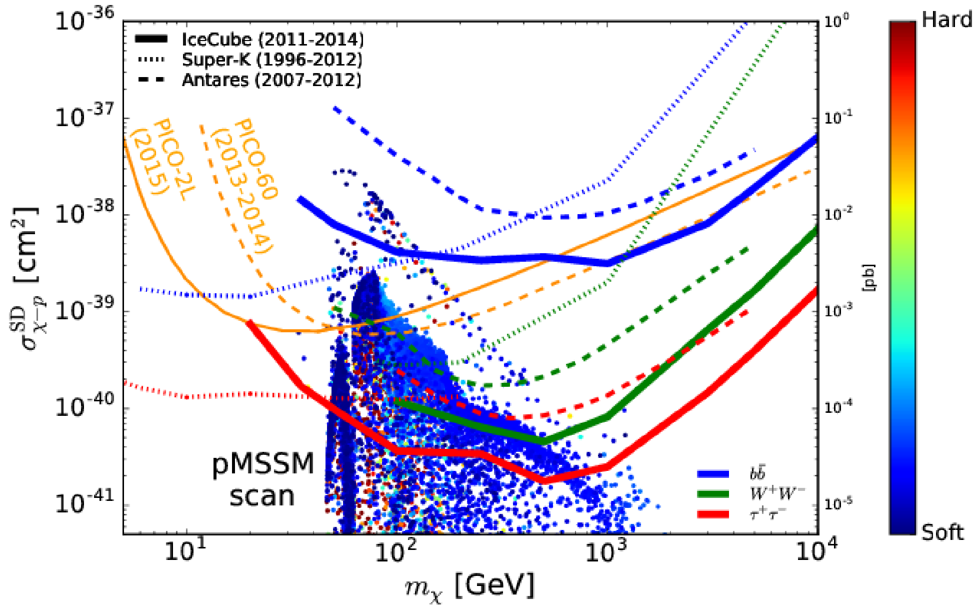

Figure 1.12: Limits on SD WIMP-proton scattering for neutrino telescopes and direct detection experiments. Line colors represent different possible decays of WIMPs. Colored points correspond to different theoretical models with different parameters [55].

are arranged in 86 strings 125 m distant one another with 60 DOMs each, 17 m distant along the string. This set up allows IceCube to be sensitive to neutrinos with energies as low as ∼ 100 GeV/c^2. In the central region strings are closer to form a sub-array dubbed *DeepCore*: the optimized geometry and instrumentation lower the energy threshold down to ∼ 10 GeV/c^2.

The energy threshold of IceCube makes this telescope sensitive to WIMP mass down to 200 GeV, while DeepCore lowers this limit to about 50 GeV: this dictates the event selection strategies [55]. The dataset is divided into two non-overlapping samples: IceCube events are neutrinos coming from the Sun with more hits outside the DeepCore fiducial volume or at least 7 hits, while DeepCore events are defined as the complementary dataset. Even if the direction of solar neutrinos is almost horizontal within the detector because of the position of the Sun at the South Pole, atmospheric muons and neutrinos represent the main background.

The presence of annihilating WIMPs in the inner Sun can be detected as an anomalous flux of solar neutrinos and this is the reason why it is fundamental to know the hypothetical flux coming from the Sun and the expected background. After 532 days of livetime, IceCube and DeepCore set the best limits on SD WIMP-proton scattering for $m_\chi \gtrsim 80\,\mathrm{GeV/c^2}$ as the comparison plot in Fig. 1.12 shows, while limits on SI scattering are worse than the one set by direct search experiment.

Super-Kamiokande

Located in the 1000 m deep Kamioka mine in Japan, Super-Kamiokande (SK) is a 41.4 m tall cylindrical water Čerenkov detector with a diameter of 39.3 m, filled with more that 50 kt of ultra pure water [57]. It consists of an inner detector of 22.5 kt fiducial volume instrumented with more than 11129 50-inch PMTs and an outer detector instrumented with 1885 8-inch PMTs used as cosmic rays veto.

For DM analysis SK collaboration used three categories of event [58]: fully-contained (FC) if the event is entirely observed in the inner detector, partially-contained (PC) if the event is observed in the inner detector but some energy is deposited in the outer one and upward-going muons (up-μ) if it is a muon coming from below. Using 3903 days of data, SK collaboration did not find any excess over expected atmospheric-neutrino background and they set the best limits for SD WIMP-nucleon scattering, eventually lowered by IceCube results as Fig. 1.12 shows.

1.5.2 Gamma rays from galactic centers

Another possible signal coming from WIMPs annihilation is very high energy γ rays, as they travel in straight lines in the local Universe and therefore it is possible to track back their source. The annihilation of DM is possible because of the contribution of fermionic loops as shown in Fig. 1.13a: a direct couple with photons is forbidden as DM does not interact electromagnetically, by definition. Since annihilating WIMPs move in the dark halo with non-relativistic velocities (the local mean speed for DM is $\langle v\rangle \sim 270\,\mathrm{km/s}$), momentum-energy conservation gives two back-to-back photons with energy $E_\gamma = m_\chi$ and intrinsic energy spread of only $\sim 10^{-3}$, due to the Doppler effect [59]. Therefore, detecting photons coming from WIMPs annihilation would lead to a direct measurement of their mass: this feature makes this technique very appealing.

As high energy photons interact with matter via e^+e^- pair production with a mean free path of about 38 g/cm^2, it is impossible for these γ rays to reach ground based telescopes: the Earth's atmosphere is 1030 g/cm^2, therefore photons interact producing electromagnetic showers before being detected. Thus, observations must be done from space or using Čerenkov telescopes detecting secondary particles forming electromagnetic showers.

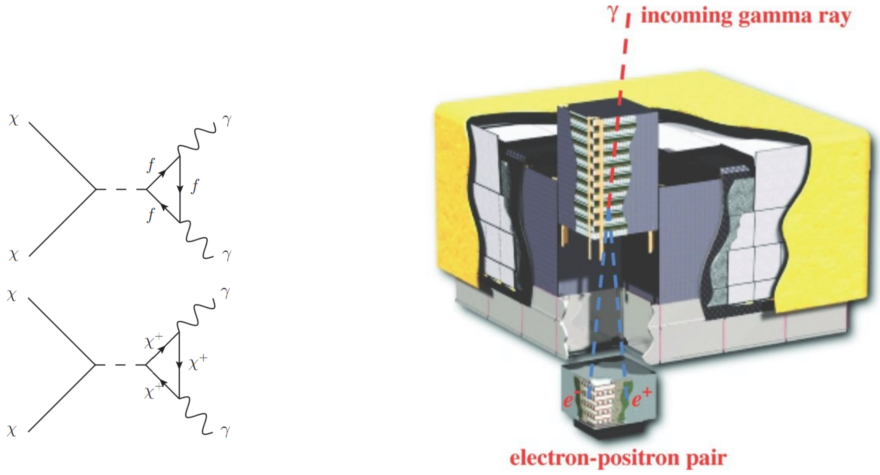

(a) **(b)**

Figure 1.13: (a) A fermionic loop is a possible contribution to WIMP annihilation into a pair of high energy γ's. (b) A γ ray entering the Fermi-LAT detector undergoes pair conversion: $e^+ - e^-$ direction and energy give information about the parent photon.

Fermi - Large Area Telescope

The Large Area Telescope (LAT) is a pair-conversion telescope used to detect γ rays in the energy range 20 MeV÷300 GeV/c^2: it consists of a 4×4 modules array, each module including a tracking section of alternating silicon microstrips and tungsten foils and a CsI calorimeter to measure the total energy [60].

In its search for DM, Fermi-LAT looks for a signature in the isotropic diffuse gamma ray background, dubbed IGRB, due to the annihilation of WIMPs in the dark halo embedding the entire Galaxy. After 50 months of Fermi-LAT data taking, it was possible to measure the IGRB spectrum in the energy range 100 MeV÷820 GeV/c^2, setting limits on the presence of WIMPs in the galactic halo for masses from few tens of GeV up to few tens of TeV [61].

1.5.3 Cosmic antimatter

The most discussed indirect search for DM involves the detection of antimatter in cosmic rays (CRs): an anomalous component could be due to WIMPs annihilation in the Galactic halo. These additional exotic components are potentially detectable as spectral distortions for the various cosmic radia-

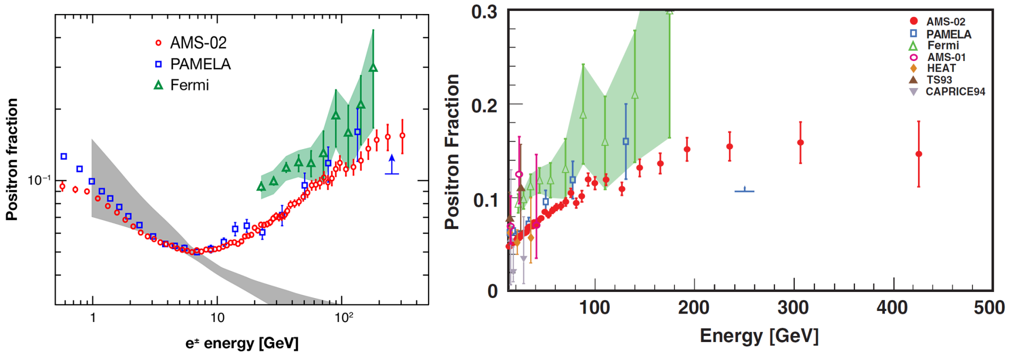

(a) **(b)**

Figure 1.14: (a) Positron fraction $\phi(e^+)/(\phi(e^-) + \phi(e^+))$ as measured by PAMELA (2009), Fermi-LAT using Earth magnetic field to identify positrons and electrons (2012) and AMS-02 (2014). (b) Positron fraction above 10 GeV/c^2, where it begins to increase to become flat above $\sim$200 GeV/c^2.

tions:

$$\chi\bar{\chi} \rightarrow q\bar{q},\, W^+W^-,\, \ldots \rightarrow \bar{p},\, \bar{d},\, e^+,\, \ldots \tag{1.31}$$

and this implies that an anomaly in the spectrum should be observed for different components of CRs spectrum. Unlike γ rays and neutrinos, however, these charged particle do not point to their source due to the presence of galactic magnetic field. The detection of primary cosmic rays must be carried outside the Earth's atmosphere, using detectors mounted on satellites or on balloons. The Payload for Antimatter Matter Exploration and Light-nuclei Astrophysics (PAMELA) was the first satellite-based experiment dedicated to the detection of CRs, with a particular focus on antimatter and light nuclei components. After its lunch on June 15, 2006, PAMELA had been almost continuously taking data until January 2016. The combination of different detectors provided a good particle identification efficiency and a precise energy measurement, necessary to study in details the spectrum of CRs up to hundreds of GeV [62].

In 2008 PAMELA collaboration observed an anomalous positron abundance in the cosmic radiation for the energy range 1.5 - 100 GeV/c^2 [63], as shown in Fig. 1.14a in comparison with the more recent data by AMS-02. The measured positron fraction is not consistent with the theoretical model of secondary production of positrons during the propagation of CRs in the Galaxy. This disagreement could be a signature of the annihilation of WIMPs in the dark halo of the Milky Way: since the antiproton flux is compatible with the expected background this would suggest a leptophilic DM. There are other possible explanations for the observed positron excess, for example the presence of near pulsars, as the latest observations by HAWC suggest [64].

AMS-02

The second phase of the Alpha Magnetic Spectrometer (AMS-02) is an antimatter search experiment mounted on the International Space Station (ISS). Like PAMELA detector, the combination of different sub-detectors improves the particle identification efficiency and the energy measurement resolution: this is fundamental to detect and identify antimatter.

AMS-02 confirmed the results from PAMELA observing a higher fraction of positrons in CRs than what expected by the standard secondary production model: the results were extended in the energy range 0.5 - 500 GeV [65]. The results in Fig. 1.14b clearly shows an increasing positron fraction in CRs up to ~200 GeV/c^2 it is clear an increment of the positron fraction. Moreover, AMS-02 measured an unexpected fraction of antiproton $\phi(\bar{p})/\phi(p)$ [66]: this anomalous flux can be hardly explained by a pulsar model. An explanation both for the anomalous positron flux and for the anomalous antiproton flux could be assuming the presence of heavy WIMPs $\left(m_\chi \gtrsim 500\,\mathrm{GeV/c^2}\right)$ in the galactic halo: this hypothesis led AMS-02 collaboration to evaluate the annihilation cross section of such WIMPs in the order of $10^{-23} \div 10^{-24}\,\mathrm{cm^3 s^{-1}}$.

1.6 Direct search

The WIMP miracle suggests DM may interact with ordinary matter like nuclei via weak interactions: this is mediated by massive vector bosons and characterized by extremely small cross sections. In this case it would be possible to discover WIMPs by detecting their scattering off nuclei: this is defined *direct detection* since the observable is due to the interaction of DM with ordinary matter. The very low cross sections require the use of large target masses and ultrapure detectors, in fact WIMP-nucleus scattering are rare events with a differential rate[3] given by

$$\frac{dR}{dE_R} = \frac{\rho_0}{m_\mathrm{N} m_\chi} \int_{v_\mathrm{min}}^{+\infty} v f\left(v\right) \frac{d\sigma_\mathrm{WN}}{dE_R}\left(v, E_R\right) dv \tag{1.32}$$

where ρ_0 is the local DM density, $\frac{d\sigma_\mathrm{WN}}{dE_R}\left(v, E_R\right)$ is the differential cross section of WIMP-nucleus elastic scattering and $f\left(v\right)$ is the WIMP speed distribution.

---

[3] Differential rate is usually expressed in terms of counts kg^{-1}day^{-1}keV^{-1}, or DRU (Differential Rate Unit).

The low event rate requires a low background and this is the reason why direct search experiments are placed in underground laboratories.

The elastic scattering WIMP-nucleus induces an energy transfer to the target which can be observed through three different signals:

- **heat**, the incident WIMPs induce vibrations in the crystal lattice of the target (i.e. phonons) and this can be measured as a temperature increase;
- **free charge** due to the ionizing power of recoiling nuclei;
- **scintillation light** produced by the excitation and de-excitation of atoms and molecules in the target as nuclei recoil.

Experiment based on direct detection of WIMPs may exploit one of these signals or even a combination of them, reaching a higher sensitivity and a lower threshold in energy leading a higher sensitivity for lower WIMP masses.

1.6.1 Cryogenic bolometers

A *bolometer* is a device for measuring the power of incident radiation: it consists of an absorptive element and a thermal reservoir, connected through a thermal link. Any deposited energy in the absorptive element increases its temperature, but the thermal link restores the equilibrium within a characteristic time: a resistive thermometer measures the temperature variation proportional to the amount of deposited energy. As the entire set up is at cryogenic temperature, it is possible to reach very high sensitivities for low energy events.

Cryogenic detectors have set the best upper limit on WIMP-nucleon elastic scattering cross section for WIMPs with low mass m_χ. In the following the main three cryogenic detectors are discussed.

CRESST

The CRESST-III experiment is the third phase of the CRESST (Cryogenic Rare Event Search with Superconducting Thermometers) project at LNGS. It is a modular experiment which can host up to 33 modules operating at a temperature of 15 mK [67]: currently, only 13 modules are operating. As schematically shown in Fig. 1.15a, each module consists of a $CaWO_4$ cylindrical crystal with a height and diameter of 4 cm: the deposited energy is detected both as an increase in temperature and as an emission of light. Simplifying the detector as an absorber with a heat capacity C, an energy

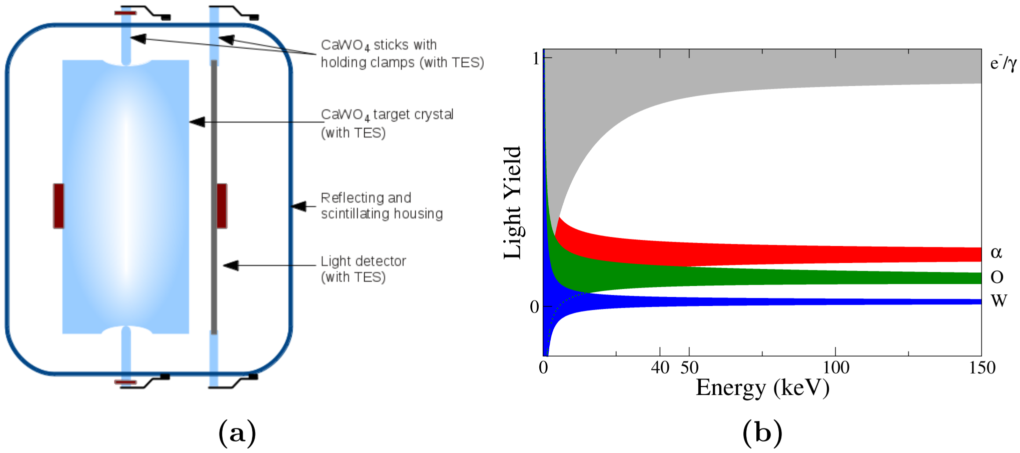

Figure 1.15: (a) Scheme of the detector design for CRESST-III modules. (b) Bands resulting from different event types in the ligh yield - energy plane. The light yield is normalized to 1 for gamma radiation with an energy of 122keV. Therefore, the light yield of betas and gammas (gray band) is about 1. For alpha particles (red band) the light yield is about 0.22 and for nuclear recoils it is even lower: about 0.1 for Oxygen (green band) and 0.02 for Tungsten (blue band).

deposition δE leads to a temperature rise $\delta T = \delta E/C$ which is measurable using superconducting phase transition thermometers such as TES (Transition Edge Sensors). Thin tungsten films are evaporated onto a surface of the $CaWO_4$ crystal and they're stabilized to superconducting phase: in this way a small temperature rise leads to a large increase in resistance, making TES extremely sensitive thermometers with a threshold corresponding to $\lesssim 100\,\text{eV}$. In order to detect the light signal each module is equipped with a $\sim 500\ \mu$m silicon on sapphire light detector.

Exploiting the double signal in heat and light, it is possible to discriminate nuclear recoil from electronic recoils: because of light quenching, scattering nuclei have a lower light yield with the same energy deposition than electrons as Fig. 1.15b shows. In 2014 the CRESST collaboration published the results from the analysis of 29.35 kg·days in the energy region $[0.6, 40]$ keV of the second phase, CRESST-II, as shown in Fig.. They were improved in 2017 by the current phase: a preliminary analysis of 2.39 kg·days in the energy region $[0.1, 40]$ keV set the best upper limits for low WIMPs masses down to less than 1 GeV/c^2 [68].

EDELWEISS

The project EDELWEISS (Expérience pour DEtecter Les WIMPs En Site Souterrain) aim at detecting light DM by exploiting the double signal produced by WIMPs interacting in ultra-cool Germanium crystals ($T \sim 18\,\mathrm{mK}$): heat and free charge. The EDELWEISS-III experiment is a modular set up located in the LSM (Laboratoire Souterrain de Modane, France). To reduce natural background it is surrounded by passive shields of polyethylene and lead and an active muon veto. The modules making up the detector are called FID (Fully Inter-Digitized): ultra-pure cylindrical Ge crystals with a height of 4 cm, a diameter of 7 cm and a mass of $820 \div 890$ g [69]. The heat-charge signal following an interaction requires a double read-out, based on NTD (Neutron Transmutation Doped) Ge sensors, sensitive enough to measure a temperature rise of 0.1 μK/keV, and a set of evaporated electrodes to measure the free charge.

In 2016 the EDELWEISS collaboration published results from 582 kg·days data focusing in the nuclear recoil energy range [2.5, 20] keV: for a WIMP mass of 5 GeV/c^2 they observed 9 events compared to an expected background of 6.1, setting a 90% confidence level (CL) upper limit of $4.3 \cdot 10^{-40}$ cm^2 for SI WIMP-nucleon elastic scattering cross section [70].

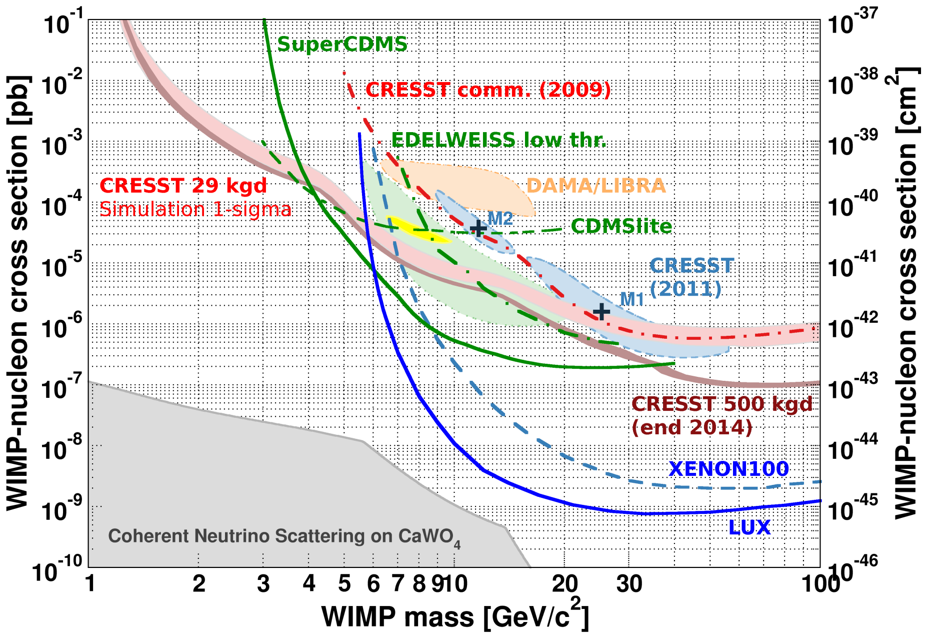

Figure 1.16: Parameter space for elastic spin-independent WIMP-nucleon scattering [68].

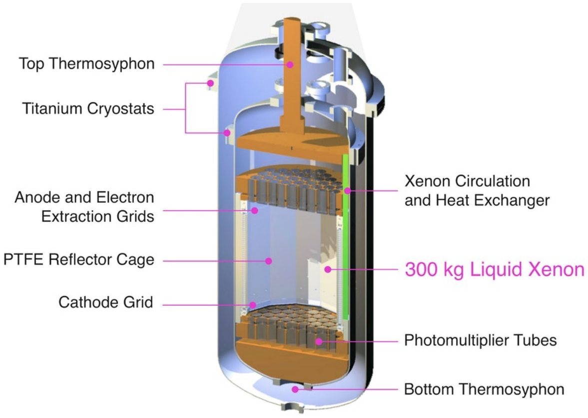

Figure 1.17: The double vessel structure of the cryostat hosts the LUX TPC.

1.6.2 Liquid noble gas detectors

The possibility of simultaneously detecting ionization and scintillation signals in liquid Xenon (LXe) or Argon (LAr), together with the possibility to scale up to larger mass at a modest cost compared to semiconductors, has contributed to make LXe and LAr popular targets for DM search and other rare physics events.

The XENON1T detector, the current generation of the XENON project, represents the latest and most sensitive example of a liquid noble gas detector: it will be discussed in detail in the next chapter.

LUX

The Large Underground eXperiment (LUX), located at the Stanford Underground Research Facility at Homestake mine, is based on a double-phase Time Projection Chamber (TPC) containing almost 250 kg of active volume of LXe and instrumented with a bottom and a top array of PMTs [71], as shown in Fig. 1.17. The TPC is hosted in a double vessel structure for thermal isolation and it is surrounded by a water tank acting as a muon veto in order to tag nuclear recoils caused by neutrons produced by CRs. Energy deposited by particle interactions in the LXe induces two measurable signal channels: prompt VUV photons from scintillation (S1), and free electrons from ionization. These electrons drifts toward the upper anode under the action of the low field inside the TPC: once they reach the GXe (gaseous Xenon) a high electric field extracts them producing a second light signal via electroluminescence (S2). The ratio of the S1 and S2 signals is used to discriminate between ERs and NRs: the detection principle of a double-phase TPC and its discrimination capabilities are described in details in the next chapter.

In 2016 LUX collaboration set the best upper limit on SI WIMP-nucleon elastic scattering cross section to $1.1 \cdot 10^{-46}\text{cm}^2$ at m_χ=50 GeV/c^2: this was achieved by combining the 2013 data (95 live days) and 2014-2016 data (332 live days) [72].

DarkSide

The current phase of the DarkSide project is DarkSide-50, a double-phase TPC containing an active mass of 50 kg of UAr, low-radioactivity underground argon [73]. In order to reduce the background coming from CRs, the TPC operates inside a 30 t organic liquid scintillator neutron veto, which is in turn installed at the center of a 1 k water Čerenkov muon veto. The main difference between Xenon and Argon is the fact that the latter presents a cosmogenic long-lived radioactive isotope, ^{39}Ar: to remove this intrinsic source of background, DarkSide uses Argon from underground natural gas reservoirs, where the abundance of this dangerous isotope is lower than the atmospheric values. The principle of detection for a double-phase LAr TPC is the same for a LXe TPC, but the former has a higher discrimination power as it can combine the information coming from the pulse shape discrimination method to the light-charge signals ratio. Indeed, electron recoils have a longer scintillation characteristic time compared to nuclear recoils.

In 2015 DarkSide-50 reported a background-free null result with an exposure of 2616 kg·days: for a WIMP mass of 100 GeV/c^2 the upper limit on WIMP-nucleon elastic scattering cross section was set to $2.0 \cdot 10^{-44}\,\text{cm}^2$ [74].

1.6.3 Annual modulation signature

A model-independent signature in DM direct search experiments is the annual modulation of the DM interaction rate: this arises because the Earth revolves around the Sun, which moves inside the galactic dark halo. As a consequence of its annual revolution, Earth should be crossed by a larger flux of DM particles, named “WIMP wind”, around 2$^{\text{nd}}$ June, when its velocity sums to Solar System’s velocity with respect to Galaxy, and by a smaller flux around 2$^{\text{nd}}$ December, when they subtract, as shown in Fig. 1.18. This motion translates into a time dependent DM speed distribution $f(v,t)$, reaching its minimum in December and its maximum in June.

DAMA/LIBRA

The DAMA (DArk MAtter) project is based on the development and use of low background scintillators: the current generation is the DAMA/LIBRA

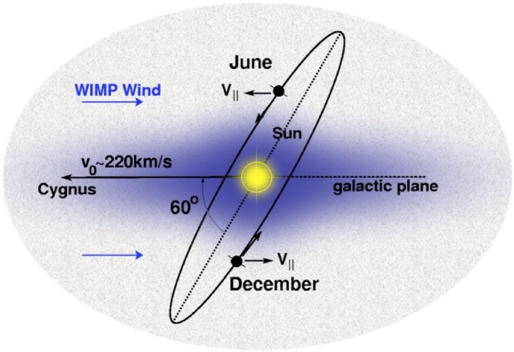

Figure 1.18: Schematic view of the Earth's motion around the Sun: its revolution leads to the annual modulation.

experiment, located in the LNGS underground laboratory and representing the upgrade of the previous DAMA/NaI detector [75]. The target consists of 25 highly radiopure NaI(Tl) blocks with 9.70 kg mass each one ($10.2 \times 10.2 \times 25.4\,\mathrm{cm}^3$) placed in a 5×5 array. The granularity of the apparatus is used to identify DM events as those events where just one of the 25 detectors fires (*single-hit* events). Because of its design, DAMA/LIBRA detector can not distinguish nuclear and electronic recoils, therefore it is only sensitive to annual modulation of WIMP signal.

With a total exposure of DAMA/LIBRA (phase 1) of $1.04\,\mathrm{t} \cdot \mathrm{y}$, DAMA collaboration announced the observation of a modulation signal in agreement with DM hypothesis. The combination of 14 annual cycles from DAMA/NaI and DAMA/LIBRA reaches a significance of 9.3σ for a total exposure $1.33\,\mathrm{t}\cdot\mathrm{y}$ [75]. Keeping free all the parameters of the single-hits events in Fig. 1.19, the fitting results give a phase $t_0 = (144 \pm 7)$ d (2^{nd} June corresponds to a phase of 152.5 days) and a period $T = (0.998 \pm 0.002)$ y. This represents one of the most discussed evidence of the existence of DM as other experiments have not observed yet the same modulation [76].

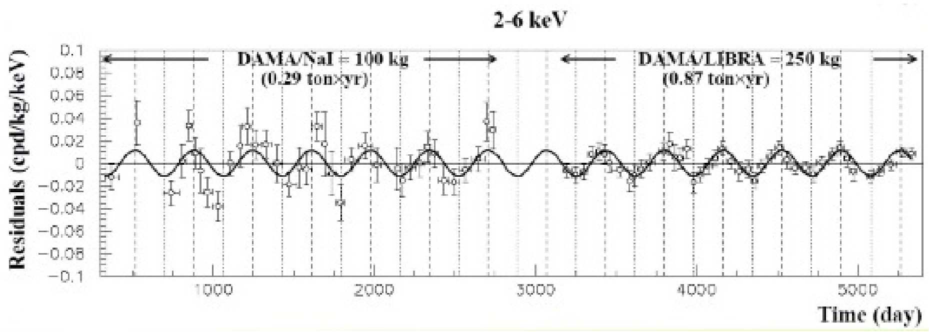

Figure 1.19: Residual rate of single-hit events measured by DAMA/NaI and DAMA/LIBRA in the energy range [2, 6] keV as a function of time. The superimposed curve is the expected annual modulation [75].

Chapter 2

The XENON project

Direct Dark Matter search experiments using liquid Xenon have set the best limits on spin independent WIMP-nucleon elastic scattering so far, thanks to their high sensitivity. Among the Xenon-based detectors, the XENON project has a leading role since it has developed the technology of the double-phase TPC based on this noble element. The advantages coming from this detector are a high energy resolution due to the detection of a double signal (charge and light) and its simple scalability. This technique is currently used by the most sensitive experiments for the direct search of DM like XENON1T [77], LUX [71] and PandaX [78]. The first phase of the project was XENON10, aiming at testing the possibility to realize a double-phase TPC with a target mass $\mathcal{O}\,(10\,\mathrm{kg})$. The positive results obtained in 2007 led to the second step of the project: a $\mathcal{O}\,(100\,\mathrm{kg})$ detector based on the same principle as the previous phase, XENON100. It set the best limits both for SI and SD interactions in 2012, improved by the LUX collaboration two years later. The present stage of the XENON project is the first tonne-scale double-phase TPC, XENON1T, hosted at the LNGS as its predecessors: with a total target mass of 2 t, it is currently the most sensitive DM search experiment. With an exposure time of only 34.2 live days, XENON1T improved the results of XENON100 of an order of magnitude, setting the exclusion limit on the SI WIMP-nucleon interaction cross section to a minimum of $7.7 \cdot 10^{-47}\,\mathrm{cm}^2$ for $m_\chi = 35\,\mathrm{GeV/c}^2$ at 90% CL. The next step of the project is XENONnT, a 6 t detector expected to take data from the end of 2019 improving the full sensitivity of XENON1T of about an order of magnitude [79].

The properties of liquid Xenon as target medium are discussed in the first part of this chapter, in order to describe the working principle of a double phase XeTPC. In the following, the stages of the XENON project are presented and the setup and results are briefly described: more details are given on the current XENON1T detector and the future XENONnT.

2.1 Particle detection using liquid Xenon

Historically, the advantages of liquid Xenon (LXe) as medium for radiation detection were first recognized by Alvarez in 1968 [80]. The unique and important feature of LXe, shared only by liquid Argon (LAr), is the production of both charge carriers and scintillation photons when energy is deposited by an incident particle. The ionization and scintillation yields are high compared to other media, for example the latter is comparable to NaI(Tl) scintillation yield, but with a faster time response. Moreover, the high atomic number (Z=54) and high density ($\sim 3\,\mathrm{g\,cm^{-3}}$) makes LXe very efficient to stop penetrating radiation, meaning that it is not only a good detector, but also a good shield.

At atmospheric pressure, the liquid phase of Xenon extends over a narrow temperature range, from about 162 to 165 K. The relatively high boiling temperature requires a modest cryogenic system, but the warm temperature makes the removal of electronegative contaminants more difficult to achieve, since at colder temperatures many impurities freeze out.

One of the peculiarity of liquid noble gases like Xenon, Argon or Krypton is the fact that their solid and liquid phases show an electronic band structure like metals, despite the very weak atomic interactions due to van der Waals forces [81]. Indeed, solid rare gases are crystals with a face-centered-cubic structure. Absorption spectroscopy provided the direct evidence of it, as the band-gap energy E_g for each solid noble gas was measured and the exciton peaks were clearly observed in the spectra. The exciton levels and the band-gap energy threshold was observed also for the spectra of LXe, LAr and LKr, proving the electronic band structure for rare gases in liquid phase.

2.1.1 Ionization yield

The energy deposited by radiation in liquid rare gases is shared among the electron-ion pairs production (N_i), atoms excitation (N_{ex}) and the production of subexcitation electrons, i.e. electrons with a kinetic energy lower than the Xenon excitation energy degrading into heat. Hence, the deposited energy E_0 is given by the balance equation by Platzman [82]

$$E_0 = N_i E_i + N_{\mathrm{ex}} E_x + N_i \varepsilon, \tag{2.1}$$

where E_i and E_x are the average expenditures of energy to ionize or excite a Xe atom, while ε is the mean kinetic energy of subexcitation electrons. For LXe the average energy lost in excitation process is comparatively small (~5%, [83]), while the energy transferred to subexcitation electrons is larger

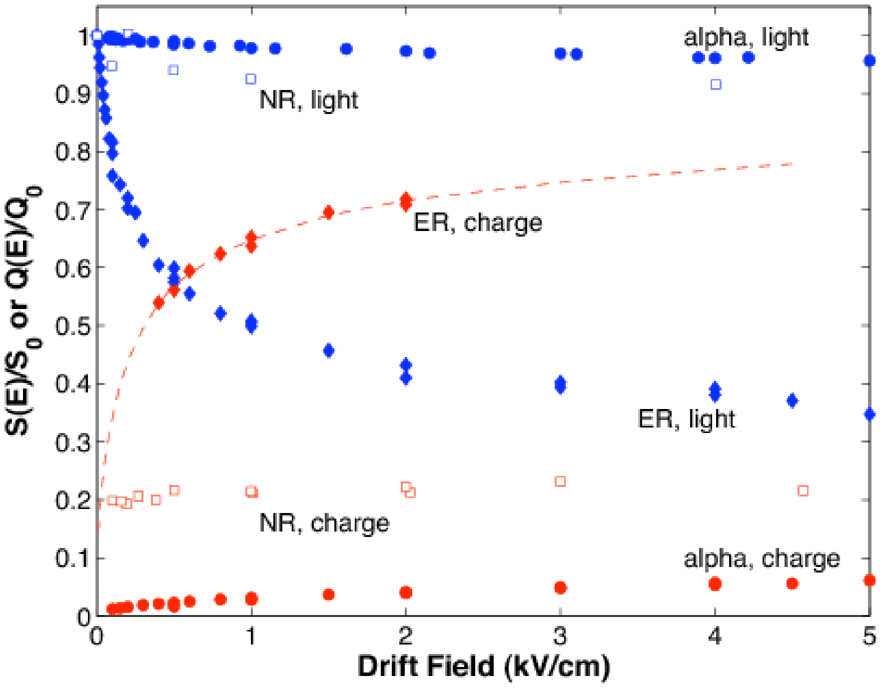

Figure 2.1: Field dependence of charge and light collection in LXe for 122 keV electron recoils (ER), 56.5 keV nuclear recoils (NR) and 5.5 MeV alphas. The charge collection (red) is the ratio between the collected charge with a field E and the collected charge with an infinite electric field, while the light collection (blue) is the ratio between the collected light with a field E and the collected light with a null electric field, i.e. when most of the electron-ion pairs recombine to produce scintillation light [84].

than 30% of the ionization potential. The W value is defined as the average energy required to produce one electron-ion pair and is given by

$$W = E_0/N_i = E_i + E_x\,(N_{\mathrm{ex}}/N_i) + \varepsilon. \tag{2.2}$$

The ionization yield, also known as charge yield (CY), is defined as the number of electron-ion pairs produced per unit absorbed energy and it is inversely proportional to the W value. A correct estimation of the deposited energy and a good charge collection, achieved minimizing the attachment to impurities and recombination, allow to infer the W value by extrapolation to infinite field. Liquid Xenon has the smallest W value among the liquid noble gases, therefore the largest ionization yield.

As we consider the fraction of collected charges, the electron-ion recombination process plays a crucial role. A fraction r of the total initial electron-ion pairs recombine forming additional excitons, hence the number of detected electrons is given by

$$N_e = (1 - r)\, N_{\text{ex}}, \tag{2.3}$$

while the number of photons due to the de-excitation of the initial and recombined excitons is

$$N_\gamma = \left(\frac{N_{\text{ex}}}{N_i} + r \right) N_i. \tag{2.4}$$

Since different particles ionizes the medium in different ways, the recombination process intensity depends on the particle's type: highly ionizing particles have tracks with a high density of free charge, leading to a higher recombination rate compared to minimum ionizing particles like cosmic muons. For example, α particles deposit most of the energy along their track in a dense electron-ion pairs core, surrounded by a sparse "penumbra" of delta rays. For α particles less than 10% of the total charge is collected at an electric field as high as 20 kV/cm, whereas the charge collection for electrons or γ rays is almost 100%. As expected, also nuclear recoils are characterized by a low charge collection because of their high atomic number leading to a dense track: nevertheless, it is higher than the collection for α particles as most of the energy is lost in secondary ionizing δ electrons, whose recombination is strongly reduced. Furthermore, nuclear recoils are highly affected by *quenching* effects [85], as most of the energy is converted into atomic motion, i.e. heat. In Fig. 2.1 the charge collection $Q\left(E\right)/Q_0$ for different values of electric fields is plotted for different type of recoils. Several emission models exist to describe the recombination process, like the Thomas-Imel model discussed in Section 4.3. However, it is fair to say that to date there is no recombination model which can fully explain the data from noble liquid detectors.

2.1.2 Transport of electrons in LXe

Because of the electronic band structure of LXe, high-energy radiation produces free electrons by exciting them to the conduction band. This structure leads to a higher drift velocity v_d for electrons in the liquid phase compared to gaseous phase, as shown in Fig. 2.2a. For low field strength E it is possible to define a linear proportionality $v_d = \mu_- E$, where μ_- is the mobility of electrons in LXe, which is about $2 \cdot 10^3\,\text{cm}^2\,\text{V}^{-1}\,\text{s}^{-1}$, close to the Silicon mobility [88]. As the electric field increases, the drift velocity saturates to a constant value. As a result of the band structure, ionization forms holes

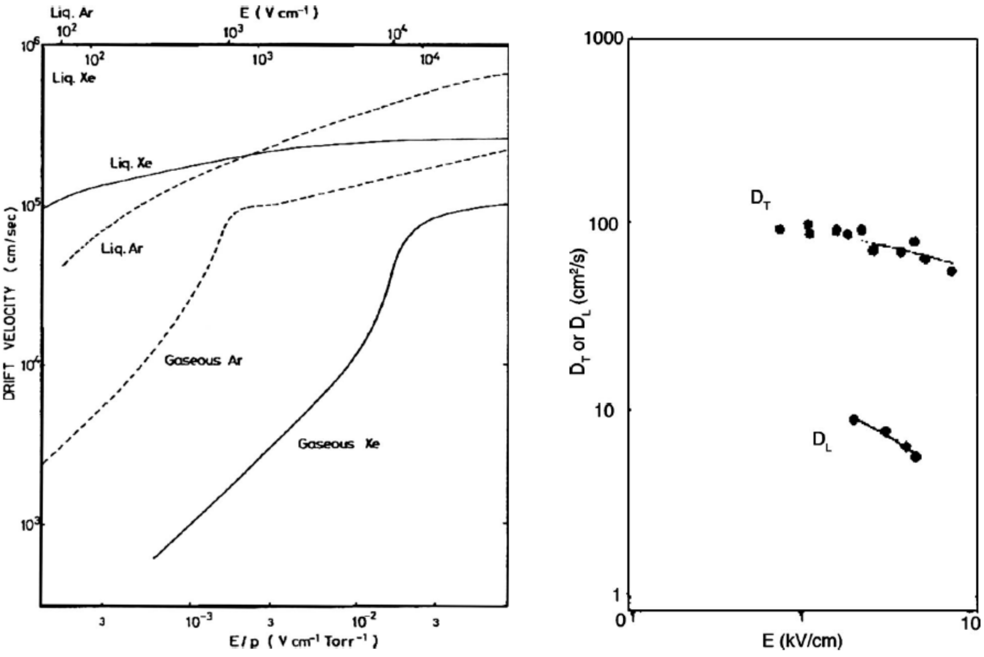

(a) **(b)**

Figure 2.2: (a) Drift velocity of electrons as a function of reduced electric field, in gaseous and liquid phases of Xenon and Argon [86]. (b) Transverse and longitudinal electron diffusion coefficients in LXe as a function of the applied electric field [87].

in the top of the valence band: their mobility is several order of magnitude lower than electronic mobility ($\mu_- / \mu_+ \simeq 10^6$) [89].

As an electron cloud drifts under the effect of an external electric field, the electrons scatter with the atoms of the medium resulting in a diffusion process. Because of the electron drift, the diffusion coefficient in the electric field direction D_L is much smaller than that in the transverse direction D_T [87], as shown in Fig. 2.2b. The former is about 10% of the transverse diffusion coefficient. After a drift time t_d the transverse spread of an electron cloud is given by

$$\sigma_{D_T} = \sqrt{D_T t_d}. \tag{2.5}$$

As electrons drift under the effect of an external electric field, they could be captured by electronegative impurities forming negative ions $e^- + S \rightarrow S^-$. This leads to an electron concentration $[e]$ decrease over the time of drift given by

$$\frac{d\left[e\left(t\right)\right]}{dt} = -k_S\left[e\left(t\right)\right]\left[S\right], \tag{2.6}$$

where $[S]$ (in mol/l) is the impurity concentration and k_S (in $\mathrm{l\,mol^{-1}\,s^{-1}}$) is the attachment rate constant. Thus, the electron concentration decays exponentially over drifting time

$$[e\,(t)] = [e\,(0)]\,e^{-k_S[S]t}, \tag{2.7}$$

where it is possible to define the *electron lifetime* as

$$\tau_e = (k_S\,[S])^{-1}\,, \tag{2.8}$$

depending on the electric field and the impurity concentration. A typical example of impurity is O_2: for stable observation of ionization signals with high charge yield, the impurities concentration needs to be lower than 1 ppb of O_2 equivalent substances [81].

Electrons drifting in a high electric field, usually higher than 10^6 V/cm, gain a sufficient kinetic energy between two consecutive collisions to ionize the medium. In this way starting from a single electron-ion pair it is possible to obtain an entire avalanche: the maximum gain, which has been measured using cylindrical chamber, is a factor of several hundred [90].

2.1.3 Scintillation yield

In addition to the ionization of the medium, liquid rare gases can emit scintillation in the region of vacuum ultraviolet (VUV) light. For LXe, the wavelength of the scintillation photons is centered at 177.6 nm. The origin of the luminescence emission is attributed to the decay of excited dimers (excimers) to the ground state. They can be produced by two different processes involving excited atoms (Xe^*):

$$\begin{aligned} &\mathrm{Xe}^* + \mathrm{Xe} + \mathrm{Xe} \rightarrow \mathrm{Xe}_2^* + \mathrm{Xe},\\ &\mathrm{Xe}_2^* \rightarrow 2\mathrm{Xe} + h\nu, \end{aligned} \tag{2.9}$$

or ionized ions (Xe^+) [91]:

$$\begin{aligned} &\mathrm{Xe}^+ + \mathrm{Xe} \rightarrow \mathrm{Xe}_2^+,\\ &\mathrm{Xe}_2^+ + e^- \rightarrow \mathrm{Xe} + \mathrm{Xe}^{**},\\ &\mathrm{Xe}^{**} \rightarrow \mathrm{Xe}^* + \text{heat},\\ &\mathrm{Xe}^* + \mathrm{Xe} + \mathrm{Xe} \rightarrow \mathrm{Xe}_2^* + \mathrm{Xe},\\ &\mathrm{Xe}_2^* \rightarrow 2\mathrm{Xe} + h\nu. \end{aligned} \tag{2.10}$$

Since excimers Xe_2^* can be formed in a singlet or in a triplet state, the scintillation signal in pure LXe is the sum of a fast and a slow components:

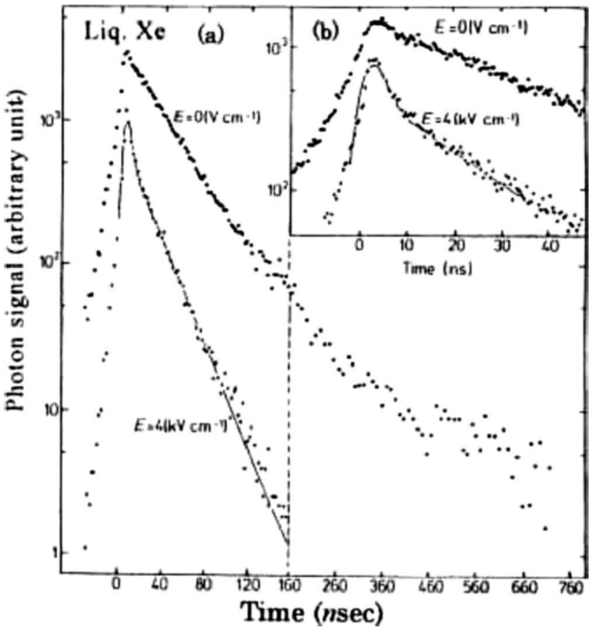

Figure 2.3: Scintillation signal for an electron in LXe with and without an electric field of 4 kV/cm, over a long time scale (a) and a short time scale (b) [91].

the former caused by the direct de-excitation of the singlet excimers, while the latter by the triplets. In absence of an external electric fields, the scintillation signal for α particles and fission fragments is characterized by a fast component $\tau_{\mathrm{f}} \simeq 4\,\mathrm{ns}$ and a slow one $\tau_{\mathrm{s}} \simeq 20\,\mathrm{ns}$ [92]. For relativistic electrons, the low deposited energy density leads to a slow electron-ion recombination, therefore the signal is dominated by a single component with a decay time of 45 ns. As an electric field is applied to the LXe, the double component structure is observed also for electrons, with $\tau_f \simeq 2\,\mathrm{ns}$ and $\tau_{\mathrm{s}} \simeq 27\,\mathrm{ns}$ [92]: this is shown in Fig. 2.3. The difference between the scintillation signal decay for different types of incident particles can be used to discriminate these particles: this technique is called pulse-shape discrimination (PSD) and it is widely used with organic scintillator [93]. The small time separation of the decay components makes difficult to use this technique with LXe-based detector, but for LAr this is an effective technique as the singlet and triplet components have very different lifetime, about 5 and 1590 ns. For this reason LAr based TPCs have the advantage to be able to operate in a single phase mode, indeed they can discriminate ER and NR events using PSD techniques.

The scintillation yield, also known as light yield (LY), is defined as the mean number of emitted photons per deposited energy unit. LXe has the highest light yield compared to all liquid rare gases, and it is similar to that of the best crystal scintillator like NaI(Tl), but with a faster characteristic time. Assuming the absence of quenching processes, the maximum LY is reached when all the electron-ion pairs recombine to produce excimers, i.e. when $r = 1$ in Eq. (2.4), possible only for a null external electric field. In this best-scenario case, the average energy required to produce a single photon is

$$W_{\text{ph}} = \frac{W}{1 + N_{\text{ex}}/N_i}, \tag{2.11}$$

as obtained by Eqs. (2.1) and (2.2). Since most of the scintillation light comes from the recombination process described in Eq. (2.10), the scintillation light yield depends on the electron-ion density along the particle's track, that is strictly related to the linear energy transfer (LET). Nevertheless, a high LET does not automatically imply a higher scintillation yield. Recoiling Xenon nuclei have a high LET because of their atomic number, but their LY is lower than for electronic recoils: the ratio of these light yields is defined relative scintillation efficiency $\mathcal{L}_{\text{eff}}$ and it is about 14% for energies up to 10 keV. The LY of nuclear recoils excitation is strongly reduced by nuclear quenching, i.e. most of the energy is deposited in the medium as heat. Another quenching mechanism is based on the biexcitonic collisions [94]. Because of the high excimers density along the recoiling nucleus track, the reaction

$$\text{Xe}^* + \text{Xe}^* \rightarrow \text{Xe} + \text{Xe}^+ + e^- \tag{2.12}$$

is more likely to happen, emitting an electron with a kinetic energy given by $E_{e^-} \simeq 2E_{\text{ex}} - E_g$, where E_g is the band-gap energy of LXe. This model holds as main quenching mechanism for energies below 10 keV.

Impurities in LXe may absorb VUV scintillation light leading to an exponential attenuation of the detected signal

$$\text{I(x)} = \text{I}_0 e^{-x/\lambda_{\text{att}}}, \tag{2.13}$$

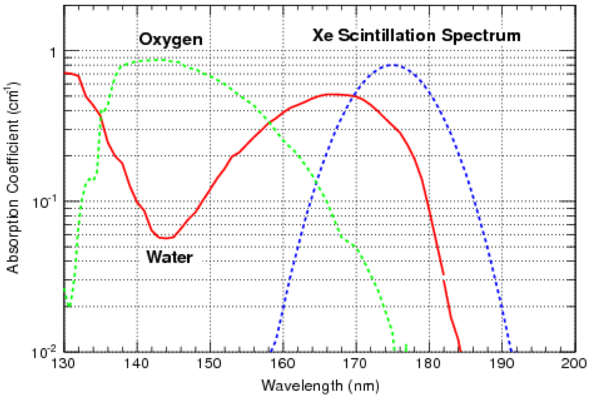

Figure 2.4: Absorption coefficient $1/\lambda_{\text{abs}}$ for VUV photons in 1 ppm water vapor and oxygen LXe and, superimposed, Xenon emission spectrum [95].

where λ_{att} is the photon attenuation length. It consists of two independent components: the absorption length λ_{abs}, describing the true loss of photons due to the presence of impurities in the LXe, and the Rayleigh scattering length λ_{sca}, representing elastic scattering of photons with atoms or molecules, without any loss. The worst impurities for VUV light of LXe are water vapor and the electronegative oxygen: Fig. 2.4 shows the absorption spectra for these impurities overlapping the scintillation light emission spectrum for LXe.

In liquid and gaseous Xenon (GXe), for high electric field below the avalanche threshold, a scintillation process called *proportional scintillation*, or electroluminescence, occurs as observed for the first time by the Saclay group [96]. Electrons produced by ionization acquire enough energy to excite atoms in collisions emitting light through a process similar to the normal scintillation [97]

$$\begin{aligned} &e^- + \text{Xe} \rightarrow e^- + \text{Xe}^*, \\ &\text{Xe}^* + 2\text{Xe} \rightarrow \text{Xe}_2^* + \text{Xe}, \\ &\text{Xe}_2^* \rightarrow 2\text{Xe} + h\nu. \end{aligned} \tag{2.14}$$

The proportional scintillation spectrum is similar to that of scintillation, therefore this signal can be efficiently detected by the photomultipliers used for scintillation light.

2.1.4 Anti-correlation of light and charge signals

In LXe-based detectors, like double-phase TPCs, both signals coming from scintillation and ionization can be observed simultaneously. Ionizing radiations deposit their energy in the medium following the Platzman balance equation Eq. (2.1), therefore the number of excited atoms and electron-ion pairs is proportional to the deposited energy and to its LET. Excluding impurities' effects, the sum of the scintillation and ionization signal divided by

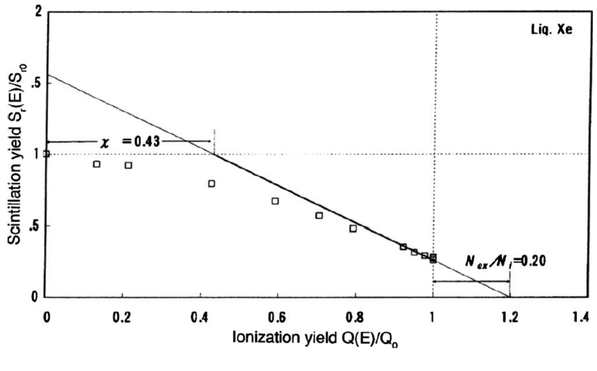

Figure 2.5: Relation between CY and LY for 1 MeV conversion electrons emitted by ^{207}Bi in LXe. The straight line indicates the perfect anticorrelation. χ is the fraction of escape electrons over electron-ion pairs produced [98].

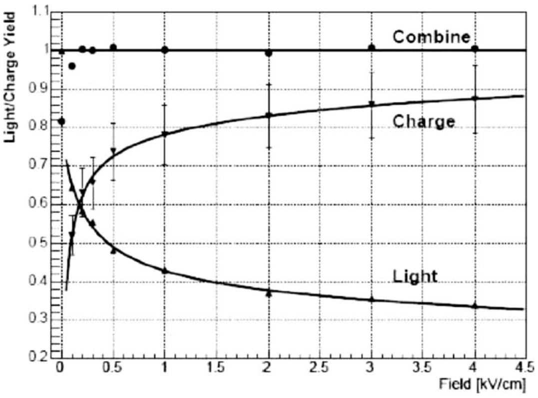

Figure 2.6: Ionization and scintillation yield as a function of the applied electric field for ^{137}Cs 662 keV γ rays [99].

$N_{\mathrm{ex}} + N_i$ gives a completely flat LET dependence: this holds if excited atoms and electron-ion pairs are exclusively converted into light or free charge signals. This leads to a perfect anticorrelation between the CY and LY. For relativistic electrons this correlation does not perfectly hold: for low LET the light yield decreases because of escape electrons, i.e. those electrons not recombining for an extent period of time in the absence of electric field. These electrons can be collected as charge signal for high electric fields: Fig. 2.5 shows that for a high charge collection $Q(E)/Q_0$ the anticorrelation, represented by the solid line, holds.

Since ionization and scintillation signals are anticorrelated, also their fluctuations are: this means that for a under-fluctuation of one signal, the other over-fluctuates. Indeed, by normalizing the detected signals to the numbers of photons or electrons emitted by LXe, their sum is constant and independent on the electric field applied, as Fig. 2.6 shows. As a result, the fluctuation of the sum signal is smaller than that of the individual signals. Therefore, a measurement of both the charge and light signals improves the energy resolution of the LXe-based detector.

2.1.5 Liquid Xenon as Dark Matter target

The double anti-correlated signal and the relatively simple cryogenics required make LXe one of the most promising medium for particle detection. It is a particularly suitable candidate for the direct detection of WIMP-nucleus scattering for several reasons, starting from the essential capability to discriminate electronic recoils and nuclear recoils. Its great stopping power due to the high density ($\rho_{\mathrm{LXe}} \simeq 2.96\,\mathrm{g\,cm^3}$) self-shields LXe from external penetrating radiations like γ rays or high energy electrons, reducing the background coming from external sources like the materials of the detector or the environment. Moreover, since WIMP-nucleus cross section is expected to scale as A^2, the large atomic number ($\langle \mathrm{A} \rangle \simeq 131$) increases the expected WIMP interaction rate, increasing the sensitivity.

Compared to other noble gases, like Argon, Xenon has only short-lived isotopes. Hence, it is a rather pure material and it does not require any further purification as it is the case of Argon, which needs to be depleted as the cosmogenic radioisotope ^{39}Ar is a beta emitter with a half-life of about 270 years [100].

Among the ten stable isotopes of Xenon, two of the most abundant in nature have non-zero spin: ^{129}Xe has spin 1/2 and ^{131}Xe has spin 3/2. This allows to study also the dependence of the WIMP-nucleus scattering cross section on the spin, thus providing more information about the Dark Matter nature.

2.2 Detection principle of a double-phase TPC

The core of the XENON project is the double-phase XeTPC detector, a time projection chamber exploiting both the light and the charge signals produced by the interaction of particles with the target LXe. The liquid target is enclosed between a bottom cathode and a grounded gate mesh to generate a uniform drift field for the electrons freed by ionization. Above the mesh, the anode is in the GXe gap: a high electric field of $\mathcal{O}(10\,\mathrm{kV/cm})$ is kept between the two in order to extract the electrons from the LXe, producing a proportional scintillation light. A top PMT array in the gaseous Xenon and a bottom array below the cathode in the liquid Xenon are used to detect the light signals, whose collection is maximized by coating the TPC internal walls using the reflective Teflon (PTFE). The photomultipliers have to be sensitive to the Xenon scintillation VUV light at $\lambda \simeq 178\,\mathrm{nm}$. The working principle of a double-phase LXeTPC is shown in Fig. 2.7

When a particle interacts with the LXe target, the deposited energy is converted both in scintillation light and in electron-ion pairs produced by ionization accordingly to the applied electric field, as described in detail in the previous section. The primary signal S1 is immediately detected by the PMT arrays, but because of internal reflection at the LXe-GXe interface ($n_{LXe} > n_{GXe}$) most of the light is observed by the bottom array.

The electrons which did not undergo recombination, are drifted by the electric field towards the anode in the GXe gap. As they reach the interface above the grounded mesh, they are extracted from the LXe into the GXe by the high electric field and they produce a proportional scintillation light signal, named S2. The number of proportional scintillation photons N_γ

contributing to the S2 signal is given by

$$N_\gamma = \alpha N_e \left(E - \beta P\right) d, \tag{2.15}$$

where P is the gas pressure, E the extraction field, d the distance traveled by N_e extracted electrons in GXe, α the amplification factor and β the threshold of reduced field for electroluminescence. The S2 signal is produced right below the PMT top array, hence about more than a half of the signal is detected by few of its PMTs which are the closest to the S2 production region. The remaining signal is observed by the bottom PMT array.

The distribution of hit PMTs for the S2 signal allows to reconstruct the position on the plane perpendicular to the drift field, i.e. the x-y position. The depth of the event with respect to the top PMT array, i.e. the z position, is given by the time difference between S1 and S2, as S1 is a prompt signal while S2 is produced one the electrons reach the GXe gap, drifting under the effect of a homogeneous electric field. Combining these reconstructions it is possible to obtain the event position inside the active volume, the fundamental ingredient to define a fiducial volume to reduce the majority of the background expected to come from detector radioactivity.

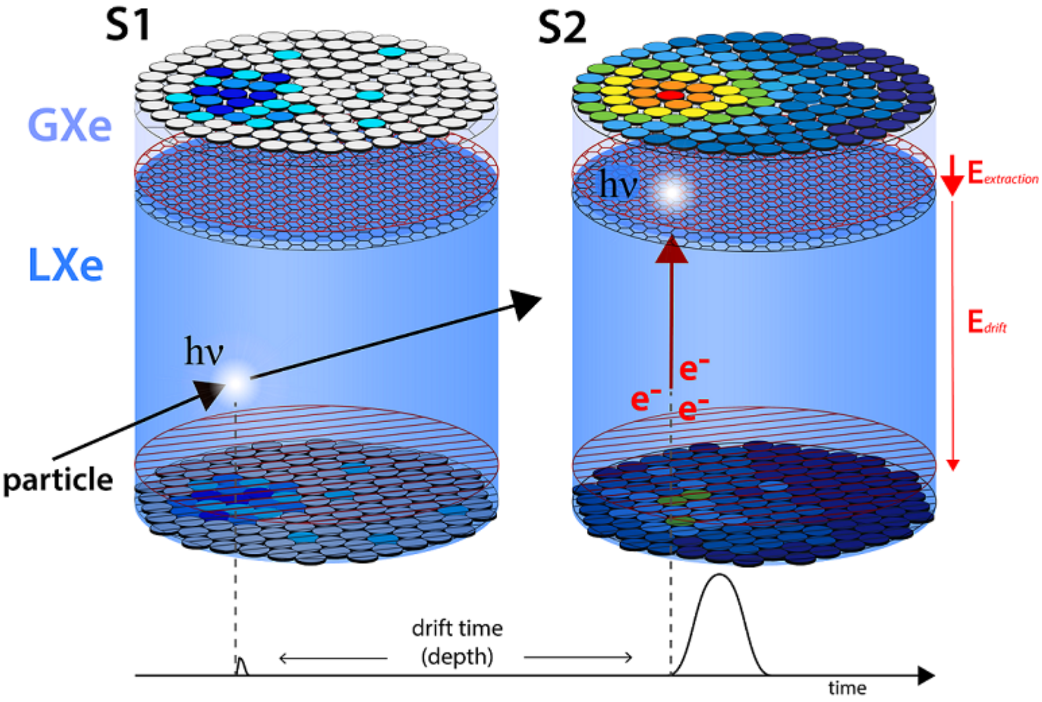

Figure 2.7: Schematic view of the working principle of a double-phase TPC based on Xenon.

The position reconstruction is important to correct the detected signals for inefficiency and absorption position-dependent effects. A light collection efficiency (LCE) map is applied to S1 signal to take into account PMT quantum and geometrical efficiencies. This correction map is obtained from ^{83m}Kr calibration data, correcting for each position in order to have an homogeneous light yield in the entire volume. Similarly, the charge signal S2 needs to be corrected both for its LCE map and for the electron lifetime. Indeed, drifting electrons may be captured by impurities or recombine with ions along their path, following an exponential decrease of the signal with the z position of the event. The electron lifetime τ_e is measured by fitting the exponential decay of the intrinsic ER calibration source S2 signal intensity as a function of the z position. The XENON1T experiment uses both α particles from ^{222}Rn and ER from ^{83m}Kr to measure the electron lifetime.

Applying these corrections to signals S1 and S2, the corrected cS1 and cS2 are obtained. Combining the cS1 and cS2, the energy resolution improves since the anticorrelation between the signals reduces the statistical fluctuations, as discussed in Section 2.1.4. The anticorrelation and the energy resolution improvement are evident in Fig. 2.8, where the ^{131m}Xe line is shown for different signals. Thus, the reconstructed combined energy is a function of both the signals and it is given by

$$E = W\left(\frac{\mathrm{cS1}}{g_1} + \frac{\mathrm{cS2_b}}{g_2} \cdot 10^{-2}\right), \tag{2.16}$$

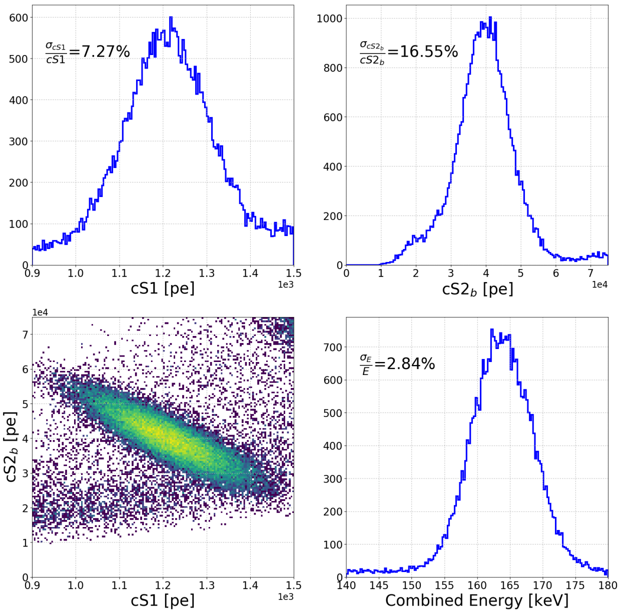

Figure 2.8: The 164 keV line from metastable ^{131m}Xe from prompt light (upper left), proportional scintillation (upper right) and its combined energy spectrum (lower right) in XENON1T detector. The resolution improves as both the signals are exploited. The anticorrelation is evident by the angle of the ellipses in the $(\mathrm{cS1}, \mathrm{cS2_b})$ space (lower left).

where $W \simeq 13.7\,\mathrm{eV}$ is the mean energy needed to produce a quantum (photon or electron), while g_1 and g_2 are the photon and electron gains, i.e. the number of observed photoelectrons per photon or electron. Instead of using the proportional signal cS2, the fraction of it collected in the bottom array $\mathrm{cS2_b}$ is preferred since it is homogeneously distributed over the entire bottom array area, whereas the proportional photons collected on the top are mainly detected by few PMTs.

2.2.1 Discriminating electronic and nuclear recoils

The ability to identify the interacting particle is fundamental for direct DM search experiments. Indeed, a WIMP is expected to interact with the medium through elastic scatter off a nucleus, producing a nuclear recoil (NR) event. On the other hand, most of the background consists of electronic recoils (ERs), like γ rays and electrons coming from radioactive isotopes, both in the detector materials and intrinsic. Therefore, being able to discriminate between ERs and NRs means reducing the main background.

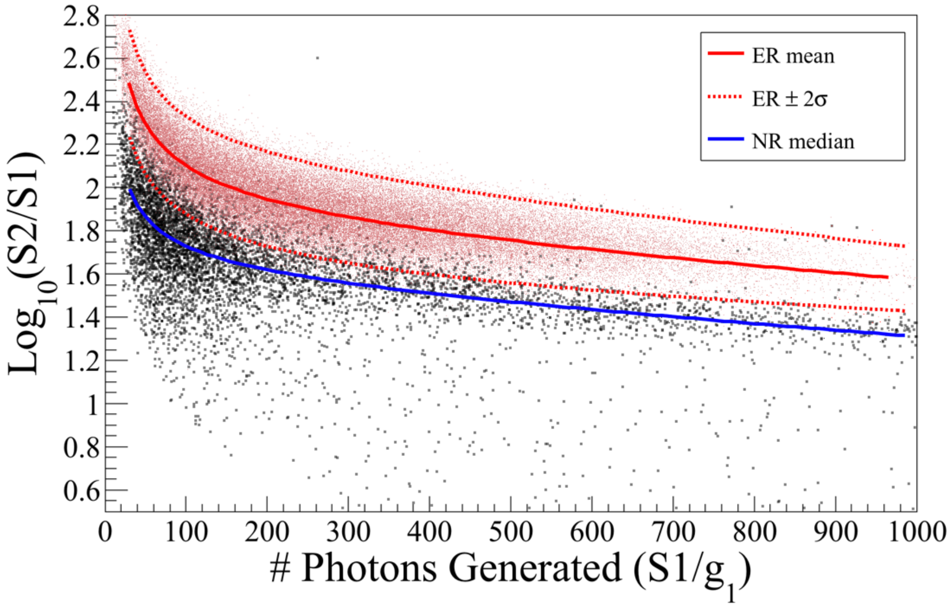

Figure 2.9: ER (red) and NR (blue) bands from CH_3T and ^{241}AmBe calibration data in XENON100 double-phase XeTPC. The mean and $\pm 2\sigma$ values of the ER band and the median of the NR band are fitted with a power law plus a first order polynomial [101].

The high LET of nuclear recoils events involves a higher recombination rate with respect to the ER events, therefore the ratio between the charge and light signals for recoiling nuclei is much lower

$$\left(\frac{S1}{S2}\right)_{\mathrm{NR}} \ll \left(\frac{S1}{S2}\right)_{\mathrm{ER}}, \tag{2.17}$$

hence the discrimination parameter $\log_{10}(\mathrm{S2_b/S1})$ can be used to distinguish between NRs and ERs. The bottom fraction of the charge signal is used as it is less affected by the position reconstruction uncertainties when the corrections are applied.

The detector response to ER and NR events is characterized through calibration runs, where γ-rays and neutrons sources are used to produce a high statistics respectively for ERs and NRs. An example of the ER and NR bands obtained with calibration runs is shown in Fig. 2.9 for XENON100 experiment in the discrimination space $(\mathrm{S1}, \log_{10}(\mathrm{S2_b/S1}))$. The ER events are from tritium calibration, while the NR events are from ^{241}AmBe calibration [101]. With the separation achieved in XENON100, a 99.5% ER discrimination corresponded to a 50% acceptance of NR events, while a 99.75% ER discrimination gave an acceptance of 40%. A good discrimination power allows to reduce the ER background impact in the WIMP search. The data analysis for XENON1T does not apply a hard cut to reject ER events, but exploits the full information of the ER and NR distributions in the $(\mathrm{S1}, \mathrm{S2})$ space through a profile likelihood treatment [102].

2.3 Past XENON experiments

The XENON project aims at the detection of WIMPs interaction with nuclei by using the technology of the double-phase XeTPC, whose working principle is described in the previous section. The advantages of this detector are the ability to detect both light and charge signals, improving the energy resolution and discriminating ER and NR events, and its simple scalability. The scalable technology have allowed the evolution of the XENON project from a 10 kg scale TPC for XENON10 experiment up to the current tonne-scale experiment, XENON1T, all of them hosted by the Laboratori Nazionali del Gran Sasso (LNGS).

In the following, the past experiments of the project and their main results are briefly discussed.

2.3.1 XENON10

The XENON10 detector was the first prototype of the XENON Dark Matter search program, containing 25 kg of pure LXe and aiming at demonstrating the achievable energy threshold and background rejection power [103]. The TPC active volume is defined by a PTFE cylinder with an inner diameter of 20 cm and a height of 15 cm, for a total amount of about 14 kg, and an electric drift field of 1 kV/cm is applied to it. The detector is protected from external background by a cubic steel-framed structure, consisting of 20 cm high-density polyethylene (HDPE) inside of 20 cm of low-radioactivity lead, as shown in Fig. 2.10b. The HDPE is used to reduce the neutron background by a factor 90, which is mainly due to radiogenic and cosmogenic production in the surrounding rock or lead.

It was installed at the LNGS and started the commissioning in April 2006, then from October 2006 to February 2007 a total of 58.4 live days of data were acquired using a fiducial volume of 5.4 kg. The blind analysis of these data excluded previously unexplored parameter space, improving upper limits on both SI and SD cross sections for WIMP scattering off nuclei. An exclusion limit at 90% CL to SI cross section of $4.5 \cdot 10^{-44}\,\mathrm{cm}^2$ was reached for a 30 GeV/c^2 WIMP mass [104], as shown in Fig 2.10a. Concerning the

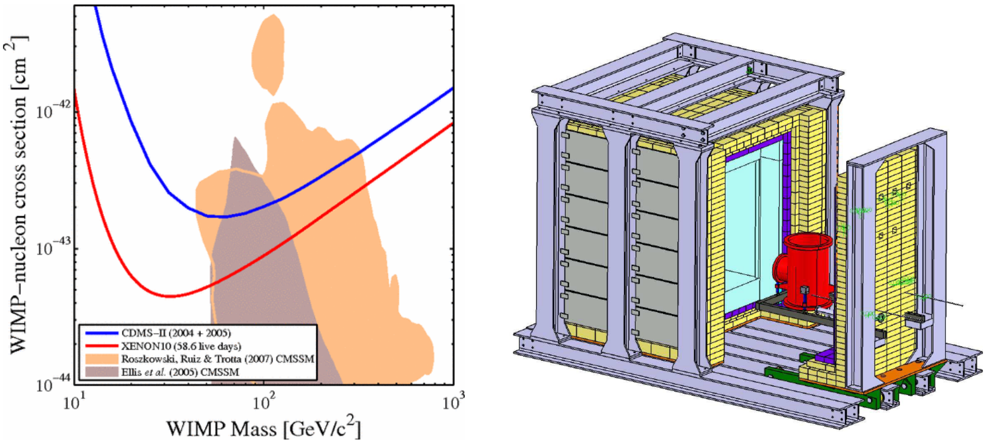

(a) **(b)**

Figure 2.10: (a) Upper limit at 90% CL on SI WIMP-nucleon interaction cross section for different WIMP masses. The red line is the result from XENON10 [104], while the blue line shows the best limit from CDMS experiment [105]. The shaded area represents the allowed parameter region for the constrained MSSM. (b) Shield structure for XENON10 detector: common and low-radioactivity lead are shown in yellow and purple respectively and HDPE is light blue [103].

SD cross section an upper limit of $5 \cdot 10^{-39}$ cm^2 was set for 30 GeV/c^2 WIMP mass [106].

2.3.2 XENON100

The XENON100 experiment started in 2008 and ended its data acquisition in the middle of 2016. The TPC is an almost cylindrical structure with a height of 30.5 cm and a diameter of 20.6 cm and the drift field is about 530 V/cm [107]. A 2D drawing of the TPC is shown in Fig. 2.11a. It contains an active LXe mass of 62 kg enclosed by 24 panels made of PTFE, chosen for its property both as insulator and good reflector for the VUV scintillation light. The active volume is read by a top and bottom PMT array, respectively made of 98 and 80 rectangular PMTs selected for their low radioactivity and quantum efficiency for the LXe scintillation light wavelength. The target is surrounded by an optically separated LXe veto, acting as an active shield of about 99 kg and it is instrumented with 64 PMTs, of the same type used for the TPC readout. An additional passive shield is used to reduce the background coming from the radioactivity of the environment, as shown in Fig. 2.11b.

After setting the best limits on SI WIMP-nucleon interaction cross section

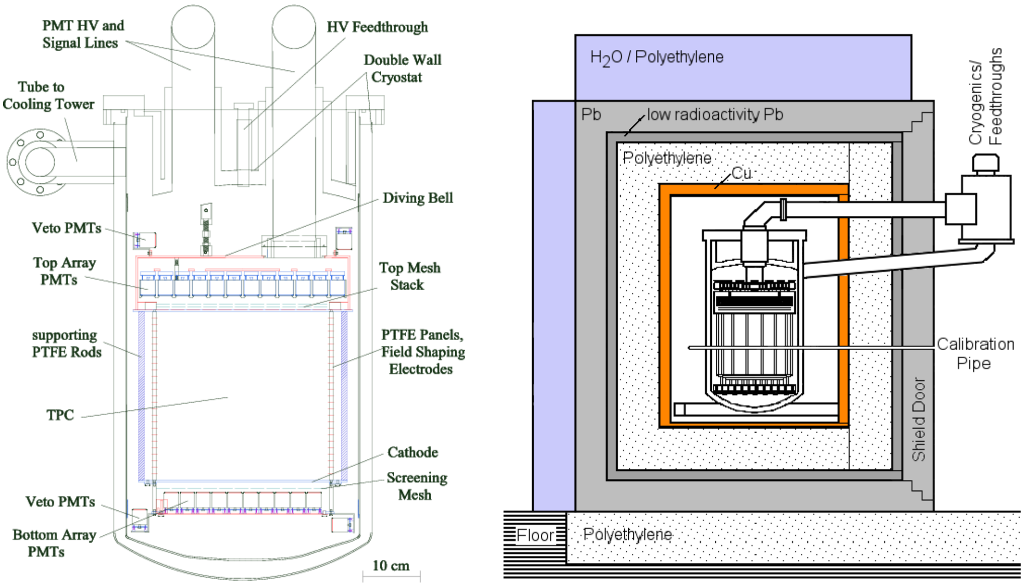

(a) **(b)**

Figure 2.11: (a) Schematic drawing of the XENON100 detector. (b) External passive shield for XENON100 detector [107].

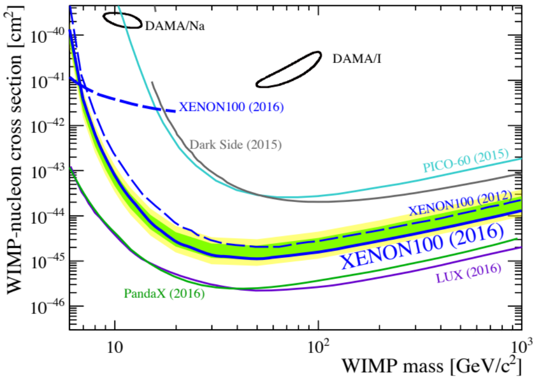

Figure 2.12: Spin-independent cross section limit (blue solid line) and 1σ (green band) and 2σ (yellow band) expected sensitivity at 90% CL from the combined analysis of three science runs of XENON100. Limits for other experiments as at the status in 2016 are plotted for comparison [109].

in 2012 using a total exposure time of 225 days with a fiducial mass of 34 kg [108], in 2016 XENON100 improved them combining three different science runs for a total exposure time of 477 live days and a fiducial mass of 48 kg [109]. A profile likelihood analysis was performed to set the upper limit on SI elastic scattering WIMP-nucleon cross section for WIMP masses above 8 GeV/c^2. It set a 90% CL minimum at $1.1 \cdot 10^{-45}\,\mathrm{cm}^2$ for a 50 GeV/c^2 WIMP mass. Using the same approach, an upper limit on the SD WIMP-neutron (-proton) elastic scattering cross section was set with a minimum of $2.0 \cdot 10^{-40}\,\mathrm{cm}^2$ ($52 \cdot 10^{-40}\,\mathrm{cm}^2$) for a 50 GeV/c^2 WIMP mass, at 90% CL.

2.4 XENON1T

The current stage of the XENON project is the XENON1T experiment, located in the Hall B of the LNGS and shown in Fig. 2.13. It was commissioned in 2016 and the first results were published in May 2017. With an active mass of about 2000 kg, it is the first tonne-scale double-phase TPC dedicated to the direct search of DM, aiming at probing spin-independent WIMP-nucleon scattering cross section down to $1.6 \cdot 10^{-47}\,\mathrm{cm}^2$ for $m_\chi = 50\,\mathrm{GeV/c}^2$ [77].

The total amount of 3.2 t of LXe is contained in a vacuum-insulated double-wall cryostat made of 5 mm thick low-radioactivity stainless steel. The inner cryostat was designed to host the XENON1T TPC, while the outer one is larger in order to host the next phase of the project, a ~ 7 t scale detector. Indeed, most of the subsystems were designed such that they can also support the larger TPC, in view of the next phase of the project, XENONnT. The TPC is a 97 cm high cylinder with a diameter of 96 cm, similar to the XENON100 detector but scaled for a factor 10 in terms of active volume, containing a LXe target of 2 t. A detailed description of the cryostat and TPC of the XENON1T experiment is given in Section 4.1.

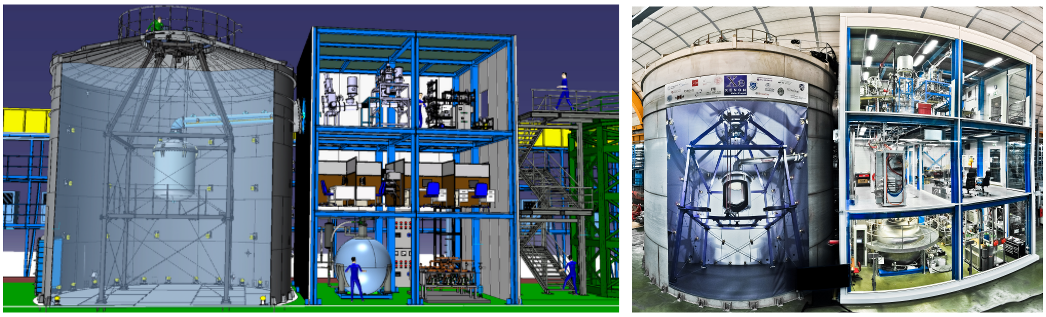

Figure 2.13: Drawing (left) and picture (right) of the XENON1T experiment with all the subsystems hosted by the service building.

The operating temperature of $T_0 = -96\,^{\circ}\mathrm{C}$ is reached following a "remote cooling" concept for the cryogenic system, which is installed outside the cryostat. In this way it is possible to reduce the material close to the TPC, to minimize the mechanical vibrations and to do maintenance while the detector is running. This system is based on two redundant pulse-tube refrigerators (PTRs) connected to a copper cold finger reaching into the Xenon volume. Passing through a vacuum-insulated cryogenic pipe, Xenon gas streams to the cryogenic system where it is liquefied by the PTRs, then collected in a funnel and flows to the cryostat. The measured total heat load of the system is 150 W and each PTR provides about 250 W [110]: the redundancy of the cryogenic system allows to operate on a PTR while the other is working. In case of a sudden Xenon pressure increase beyond a defined safety threshold, an additional backup liquid nitrogen (LN_2) cooling system maintains the pressure at a safe level. The cryogenic system is outlined in Fig. 2.14.

The Xenon must be continuously purified to keep at about 1 ppb O_2 equivalent level impurity level, as electronegative impurities are constantly outgassing from all detector components. Liquid Xenon is extracted from the bottom of the cryostat and it is evaporated in a heat exchanger system, which also cools down the return gas from the purification system. Two redundant and independent purification loops are operated in parallel. Each loop is based on a high temperature rare-gas purifier, usually called getter, removing oxide, carbide and nitride impurities. As the purified gaseous Xenon is re-condensed by heat exchanger and PTRs, the LXe flows back into the TPC, at two opposite locations below the cathode [77].

In case of emergency, the LXe can be recovered thanks to the newly developed storage system ReStoX. It consists of a vacuum-insulated stainless steel sphere with a diameter of 2.1 m, capable of containing up to 7.6 t of Xenon as a liquid, as a gas and even as a super-critical fluid, since it can withstand pressures up to 73 bar. The pressure and temperature of the

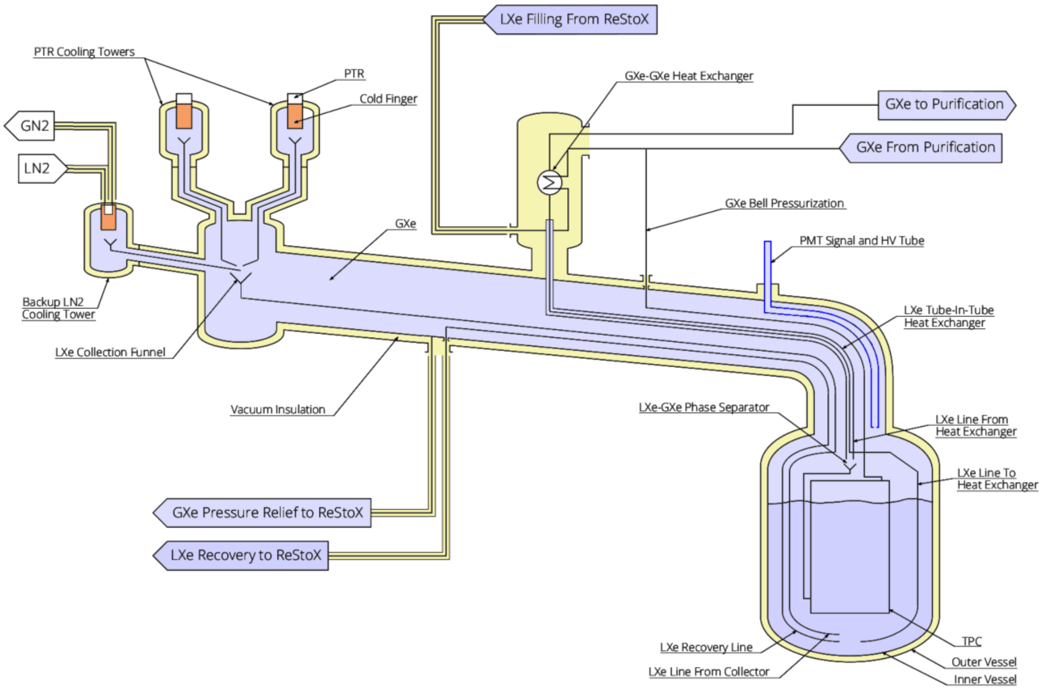

Figure 2.14: Cryogenic system of XENON1T based on a "remote cooling" concept [77]. The connection to the purification system and to ReStoX are also shown. Figure not in scale.

Xenon inside the vessel are controlled by a condenser and heater system, mounted at the center of the sphere, and the cooling is achieved by means of LN_2, provided by an external dewar of $10\,\mathrm{m}^3$. Since filling XENON1T starting with Xenon gas at 15 °C would require about 2 months using 250 W of cooling power, keeping it in its liquid phase is fundamental not to lose additional exposure time in case of emergency.

The cryostat is surrounded by a muon veto Čerenkov detector, consisting of a 10.2 m high tank with a diameter of 9.6 m, filled with deionized water and instrumented with 84 PMTs with a diameter of 20.3 cm (Hamamatsu R5912ASSY) [111]. It identifies muons to reduce the NR background due to neutrons produced by the interaction of cosmic muons with the detector materials. It can also identify showers produced by energetic muons interacting with the rock surrounding the underground laboratories. The cosmic muon flux is $(3.31 \pm 0.03) \cdot 10^{-8}\,\mathrm{cm}^{-2}\,\mathrm{s}^{-1}$ with an average energy of about 270 $\mathrm{GeV/c^2}$ in Hall B of LNGS, shielded by the 3600 m.w.e. (meters water equivalent) of rock [112]. The inner surface of the water tank is covered by a reflective foil acting as a wavelength-shifter to better overlap the Čerenkov light spectrum with the high quantum efficiency region of the PMTs, about

30% in $[300, 600]$ nm. The tagging efficiency for muons crossing the water tank is 99.5%, while it is 43% for muon-induced showers. Simulations show that the total muon-induced neutron background is reduced to $< 0.01\,\mathrm{ev/y}$ in 1 t FV, two orders of magnitude lower than the background due to radiogenic neutrons from the detector materials, therefore it can be neglected. The water tank works also as a passive shield from environmental background radiation, as it is shown by the event rate decrease during the water tank filling in Fig. 2.15.

First results from XENON1T

After a period of commissioning, XENON1T started on November 22nd, 2016 its first science run, named Science Run 0 (SR0), and it ended on January 18th, 2017, when an earthquake temporarily interrupted the detector operations. In this period the experiment collected 34.2 live days of blinded data for Dark Matter search, operating in stable conditions. During SR0 the Xenon was purified from radioactive impurities like ^{85}Kr and ^{222}Rn, leading to a low energy ER background of $(1.93 \pm 0.25) \cdot 10^{-4}\,\mathrm{events/\,(kg \cdot d \cdot keV)}$, the lowest ever achieved in a DM search detector. Calibration runs took place before and during SR0, using ^{83m}Kr for spatial corrections, ^{220}Rn to define the ER band for low energies and ^{241}AmBe for the NR band at low energy.

For the SR0 analysis a cylindrical fiducial volume of (1042 ± 12) kg of

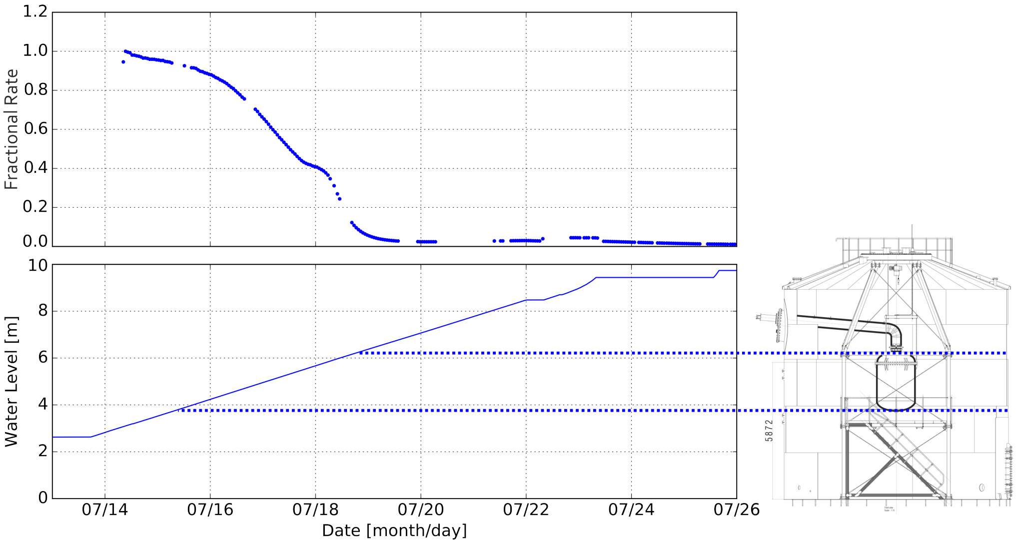

Figure 2.15: Decrease of the event rate as the water tank is filled with water. In the upper limit the events rate is normalized to the maximum activity.

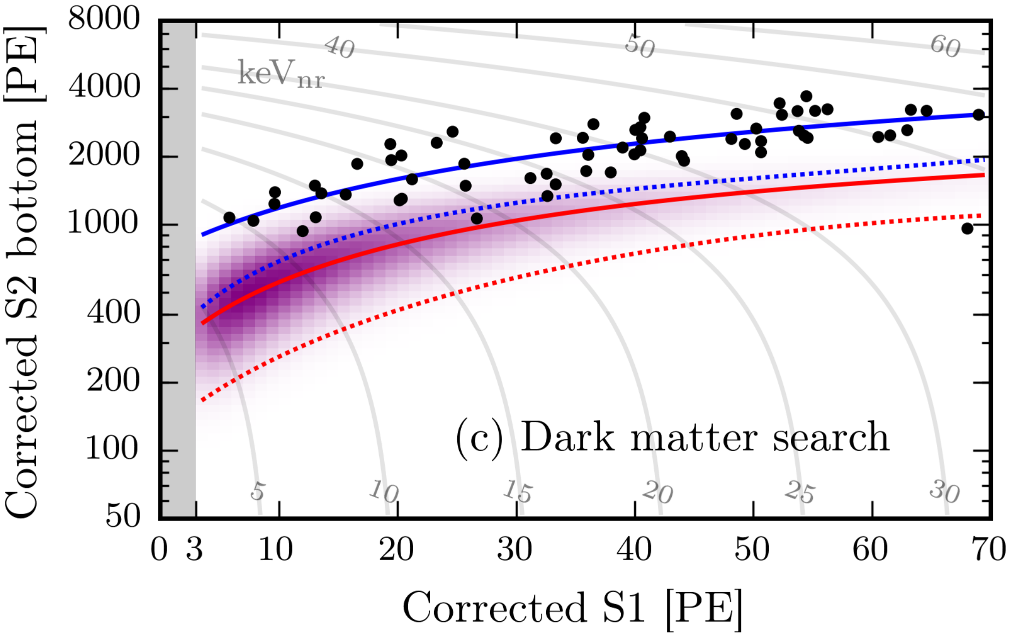

Figure 2.16: Unblinded data from SR0 of XENON1T experiment. Lines indicate the median (solid line) and -2σ (dotted) quantiles from calibration runs for ER band (blue) and NR band (red). The purple distribution indicates the signal model for a 50 GeV/c^2 WIMP [102].

LXe mass is selected, based on the reconstructed spatial distribution of ER background events. The region of interest (ROI) in the observable space is defined as $\mathrm{cS1} \in [3, 70]$ PE and $\mathrm{cS2_b} \in [50, 8000]$ PE. The main background for the WIMP search comes from the intrinsic ER background coming from β decays of ^{85}Kr and ^{214}Pb. Other background sources are radiogenic neutrons, coherent scattering of neutrinos off Xenon nuclei (CNNS), accidental coincidences of uncorrelated S1 and S2 signals, wall leakage events due to inward-reconstructed events happening on the walls and an unknown anomalous background with a uniform spectrum in the $(\mathrm{cS1}, \log \mathrm{cS2_b})$ space [102].

The data unblinding revealed 63 events in the whole ROI passing the selection criteria for a total exposure of 0.098 t·y, with only two events below the -2σ ER quantile as shown in Fig. 2.16. As no significant deviation from the expected backround were observed, an exclusion limit was set on SI WIMP-nucleon cross section at 90% CL, which improves upon the XENON100 results by one order of magnitude. The minimum at $7.7 \cdot 10^{-47}\,\mathrm{cm}^2$ for a 35 GeV/c^2 WIMP mass is currently the lowest cross section ever excluded [102]. The upper limit for a wide WIMP mass range at 90% CL is shown in Fig. 2.17, in comparison with the other great DM search experiments based

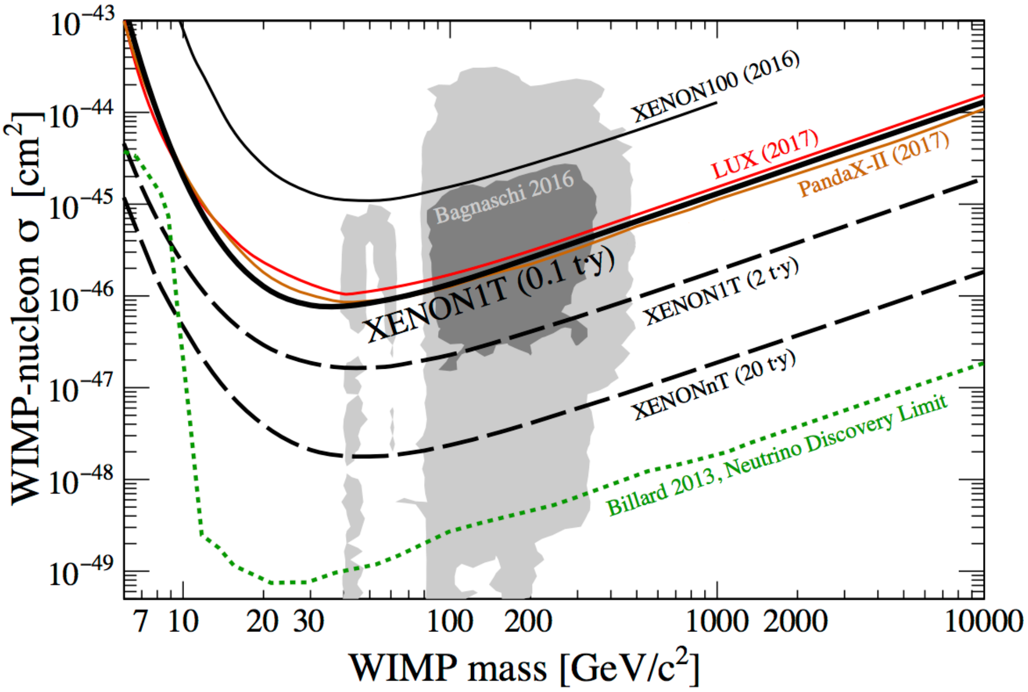

Figure 2.17: First results of XENON1T on the SI WIMP-nucleon cross section limit as a function of WIMP mass at 90% CL (solid black line) in comparison with LUX (red line) and PandaX-II (orange line). The predicted sensitivities for an exposure of 2 t · y for XENON1T and of 20 t · y for XENONnT are shown as dashed black lines [102].

on double-phase XeTPCs.

The results from Science Run 1 (SR1) are expected to be announced in Spring 2018, with a total exposure time of almost 280 live days.

2.5 XENONnT

The next phase of the XENON project is the XENONnT experiment, a near future upgrade aiming at improving the sensitivity of XENON1T of a further order of magnitude. Since most of the subsystems and the overall infrastructure of XENON1T were designed and built to host a larger TPC, leveraging on them allows a fast paced transition to the next step of the project, as the start of commissioning is expected in Spring 2019.

The largest TPC fitting in the XENON1T outer vessel using the same holding structure and leveling mechanism can contain up to 5.9 t of LXe, for a total amount of almost 8 t of Xenon in the new inner vessel leading to increase the fiducial mass of a factor 4 with respect to the current detector. This TPC has a height of about 1.6 m and a diameter of 1.34 m and its active volume is observed by a bottom array of 241 PMTs and a top array of 253 PMTs.

Among the main changes in the XENON1T subsystems, the GXe purification system will use new recirculation pumps to fasten the process and a LXe recirculation and purification systems will be used in parallel. It exploits the high density of liquid Xenon to purify faster the detection medium from electronegative impurities. Moreover, a new dedicated cryogenic distillation column will operate continuously for an online removal of intrinsic ^{222}Rn in order to reduce its background of a factor 10, namely to 1 μBq/kg.

With a very low Rn concentration in LXe, the NR background from radiogenic neutrons becomes relevant to define for the final sensitivity of XENONnT. Therefore, to reduce its contribution, a neutron veto surrounding the outer cryostat has been studied. It consists of acrylic vessels, transparent to optical wavelengths, containing Gadolinium-loaded liquid scintillator and instrumented with 120 PMTs, identical to those used for muon veto. The vessels are installed right outside the outer cryostat, with the insertion of low density closed-cell foam between the cryostat and the acrylic vessels, to avoid water in between which could capture neutrons resulting in a lower efficiency. From Monte Carlo simulations, the expected efficiency for neutron tagging is higher than 80% with an energy threshold of 200 keV: this reduces NR background from radiogenic neutrons by a factor 5, keeping the total

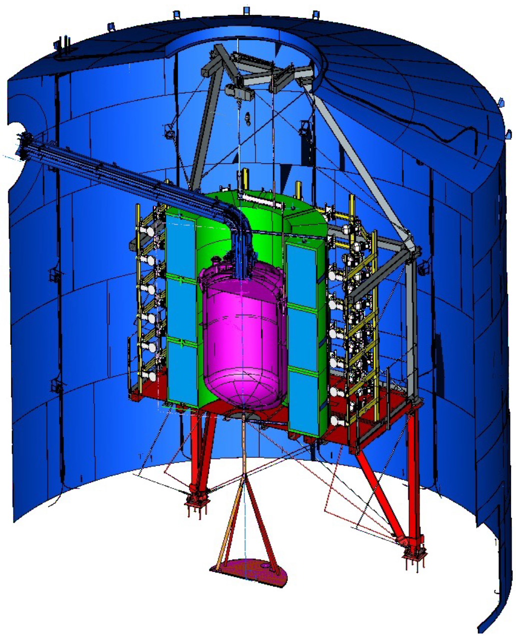

Figure 2.18: Sketch of the neutron veto surrounding the outer cryostat (purple): the acrylic vessels (green) containing the Gd-loaded liquid scintillator (light blue) and the 120 PMTs.

neutron background in the 4 t fiducial volume to about 1 event in the total exposure of $20\,\mathrm{ton} \cdot \mathrm{y}$. The sketch of the neutron veto surrounding the outer cryostat is shown in Fig. 2.18.

The XENONnT experiment will be sensitive to SI WIMP-nucleon cross section down $10^{-48}\,\mathrm{cm}^2$, as shown in Fig. 2.17: one order of magnitude above the so-called "neutrino floor" for WIMP masses above $\sim 100\,\mathrm{GeV/c}^2$, where the irreducible background from coherent neutrino-nucleus scattering becomes an important limiting factor.

Chapter 3

Neutron generator induced background

Neutron calibration is a fundamental operation to characterize the detector response to single scatter nuclear recoils, the expected signature of an interacting WIMP. For this reason the source flux has to be high enough to collect statistics to identify the NR band with a sufficient precision, but at the same time it has to be low enough to avoid pile-up effects. A neutron generator (NG) is currently used as neutron source for XENON1T experiment as its flux can be tuned in a range varying from 10 neutrons/s up to about 10^5 n/s: this fulfills the calibration requests. During NR calibration runs, the generator is vertically displaced along the cryostat inside the water tank as in Fig. 3.1. The NG sat inside the water tank for more than two months during SR1: during 2017 it was first installed from February 10th to April 13th and then from May 1st to June 8th. The NG is a stainless steel cylinder 94 cm long and with a diameter of 13.8 cm: its radioactivity, due to the radioisotopes content of the materials it is made of, can represent an additional background source during DM search runs.

In the first part of this chapter the NG is excluded to be a source for low energy ER events inside the FV: these events are the most dangerous as they may leak in the region of interest, faking a WIMP event. In the second part, the Thorium and Uranium activities for the NG are estimated in order to estimate the radiogenic neutrons flux coming from it: considering a worst case scenario the expected NR background is more than one order of magnitude lower than the expected NR background from detector materials, therefore negligible.

Figure 3.1: Deployment system for external calibration sources: red and blue belts allow movements aside and under the cryostat. The NG (green) can be vertically displaced along the cryostat.

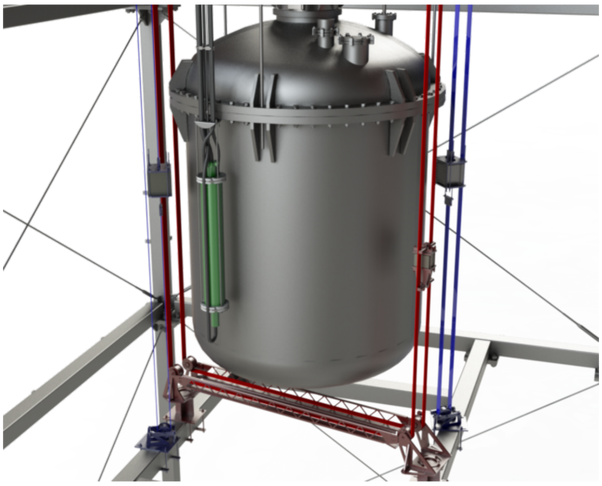

3.1 Neutron generator

An isotropic ^{241}AmBe calibration source was used both by XENON100 and by XENON1T to characterize the response to NRs: α particles emitted by ^{241}Am decays produce neutrons via the nuclear reaction $^{9}\mathrm{Be}\,(\alpha, \mathrm{n})\,^{12}\mathrm{C}^{(*)}$ in the most part. The γ-rays produced along with neutrons are shielded by a 10 cm thick lead wall surrounding the source. With a neutron yield of about 70 neutrons per $10^6\,\alpha$'s [113], the total integral flux is (160 ± 4) n/s [114]: this is low enough not to have pile-up effects.

A D-D fusion neutron generator is currently used as neutron source for NR calibration of the detector: this was characterized at the PTB (Physikalisch-Technische Bundesanstalt) and Purdue University [115]. This neutron source is more convenient since its flux can range from 10 n/s up to about 10^5 n/s or more, besides it poses minimal safety concerns when turned off. Its flux can be changed and tuned to have a high statistics with a reduced rate of pile-up events. The NG used is the 35-DD-C-W-S model, manufactured by NSD/Gradel-Fusion: it is based on the deuterium-deuterium (D-D) fusion with the emission of monoenergetic neutrons at 2.45 MeV according to the reaction

$$^{2}\mathrm{H} + {}^{2}\mathrm{H} \rightarrow {}^{3}\mathrm{He}\,(0.82\,\mathrm{MeV}) + \mathrm{n}\,(2.45\,\mathrm{MeV})\,. \tag{3.1}$$

The working principle of D-D plasma fusion is based on inertial electrostatic confinement (IEC): a high electric field is applied to the low pressure deuterium gas in order to produce the plasma by glow discharge (Paschen's law). Deuterium nuclei drift towards the cathode where a high voltage is applied ($\sim 100\,\mathrm{kV}$) to overcome the Coulomb barrier allowing D-D fusion with the emission of almost monoenergetic neutrons.

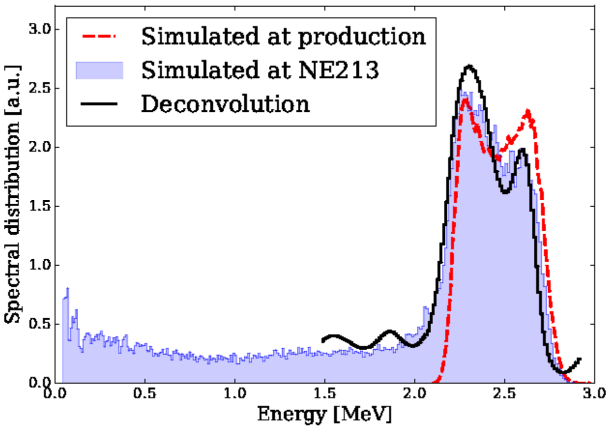

Figure 3.2: Simulated neutron spectrum in the fusion region (red dashed line) and the resulting simulated spectrum at the NE213 detector used for characterization at PTB (blue shaded histogram). The incident neutron spectrum (black solid line) is obtained by the deconvolution of the spectrum at the detector with its response function [115].

Neutron spectrum

The emitted neutron energy spectrum in the fusion region near the cathode presents two peaks: this is due to the dependence of the fusion cross section on the neutron emission angle relative to the momentum of the incident deuterium nucleus. The spectrum is characterized by two peaks at 2.22 Mev and 2.72 MeV in the laboratory frame, corresponding to the emission angles of 180° and 0°, where the cross section reaches its maxima. As neutrons propagate from the fusion region to the detector they interact with the materials loosing energy: the elastic scattering with protons in water is the most significant process, causing a long tail towards lower energies and an asymmetric peak structure. The spectrum in the fusion region and inside the NE213 detector used to characterize it at PTB is shown in Fig. 3.2.

The NG spectrum shows a smaller population at high energies: this is due to the deuterium-tritium (D-T) fusion, where the tritium T is the result of the reactions:

$$ {}^{2}\mathrm{H} + {}^{2}\mathrm{H} \rightarrow \mathrm{p} + {}^{3}\mathrm{H} \tag{3.2} $$

$$ {}^{3}\mathrm{H} + {}^{2}\mathrm{H} \rightarrow {}^{4}\mathrm{He} + \mathrm{n}\,(14.1\,\mathrm{MeV})\,. \tag{3.3} $$

As the D-T fusion has a cross section that is more than two orders of magnitude higher than D-D fusion, even a small tritium contamination can give a non-negligible amount of high energy neutrons: the total contribution to neutron yield of tritium fusion is $(3.5 \pm 0.2)\,\%$.

3.2 Electronic recoil background

One of the main drawbacks in using the NG for NR calibration is the induced ER background when it is turned off, but still sitting inside the water tank.

Indeed, in principle this could affect the DM data taking as it may represent a background source for low energies. Beside its radioactive isotopes content inducing an higher event rate for higher energies, neutrons produced by the NG when working activate Xenon nuclei. The γ-lines from activated isotopes represent an important feature in the ER spectrum since they can be used as intrinsic calibration sources.

3.2.1 Metastable Xenon isotopes activation

When neutrons enter the TPC and propagate inside the LXe, they can scatter inelastically with Xenon nuclei producing metastable isotopes, whose activities have been observed since XENON10 as γ-lines in the ER spectrum [104]. The main lines observed in the spectrum are caused by the activation of two of the most abundant Xenon isotopes: ^{129}Xe (26.44%) and ^{131}Xe (21.18%). The ^{129m}Xe isotope comes from the inelastic scattering $^{129}\mathrm{Xe}\,(n, n')\,^{129m}\mathrm{Xe}$ and it produces a γ-ray by de-excitation with an energy $\mathrm{E}_\gamma = 236.1\,\mathrm{keV}$ and half-life $\mathrm{T}_{1/2} = 8.9\,\mathrm{d}$. In the same way, the ^{131m}Xe isotope is produced by a similar inelastic scattering with a total energy $\mathrm{E}_\gamma = 163.9\,\mathrm{keV}$ and half-life $\mathrm{T}_{1/2} = 11.8\,\mathrm{d}$.

Because of their high energies, those peaks lay outside the ROI for the search of WIMPs, therefore they do not represent a background for DM search. Still, they can be used as an intrinsic calibration source with an intensity decreasing over time, but lasting for several months. Their main purpose is energy calibration to cross-check g_1 and g_{2b} values and to monitor the LY and CY stability over time, as Fig. A.1 shows.

The activation of ^{129}Xe and ^{131}Xe has been known and exploited since the first phase of the XENON project: even if the neutron flux was low, their natural abundance was high enough to have observable lines. The use of NG as NR calibration source increased the neutron flux: new activation features were observed coming from metastable isotopes not identified before because of their low activity. For example, the most abundant isotope ^{132}Xe (26.9%) can undergo neutron capture $^{132}\mathrm{Xe}\,(n, \gamma)\,^{133}\mathrm{Xe}$: the daughter product decays β^- ($\mathrm{T}_{1/2} = 5.2\,\mathrm{d}$) into an excited state of ^{133}Cs, which promptly emits a 80 keV γ-ray. Since the signals coming from the β decay and the γ pile up, they are detected as a single ER event: this translates into a β decay spectrum shifted towards higher energies of 80 keV, as Fig. 3.3 clearly shows.

3.2.2 ER background from NG materials

The materials of the NG represent a source for ER because of their radioactive isotopes content: the most dangerous contribution to the background comes from the low energy electronic recoils which could emulate a WIMP signal if laying inside the NR band. In order to study the ER background coming only from the NG sitting inside the water tank, it is necessary to find a way to isolate the NG contribution to the observed combined energy spectrum. This is achieved by considering two different DM search datasets, coincident with the period of the SR1 when the NG was installed inside the water tank (named 'NG IN') and when it was not (named 'NG OUT'). Assuming the stability over time of the detector conditions and of the other background sources, any different behavior from one dataset to the other should be attributed to the presence of the NG.

The period of time considered for this analysis goes from the beginning of SR1 on February 2nd to July 1st, 2017. Excluding from the analysis the days when the NG was mounted or unmounted (February 10th, April 13th, May 1st and June 8th), the two datasets are selected as follows:

- NG OUT from 02/02 to 09/02, from 14/04 to 30/04 and from 09/06 to 01/07 (33 days 06:13:42 exposure time);
- NG IN from 11/02 to 12/04 and from 02/05 to 07/06 (49 days 02:59:41 exposure time).

Selection cuts are applied to the datasets in order to reject multiple scattering and unphysical events, i.e. those events characterized by a S2 width inconsistent with the electron diffusion model in LXe. The selected fiducial volume is the same used for the SR0 analysis: a 83.9 cm high cylinder with a 36.94 cm radius, for a total mass of (1042 ± 12) kg [102].

The combined energy spectrum of the data with cuts applied is plotted in Fig. 3.3. While the higher energy peaks ($\geqslant 500\,\mathrm{keV}$) come from materials, the lower energy peaks are intrinsic and related to calibration sources: the ^{83m}Kr peak at 41.5 keV is a contamination of Krypton in the LXe after the end of the calibration, while the others two peaks are the metastable Xenon isotopes activated during NR calibration. In the same way the spectrum of 'NG IN' dataset shows a knee around 80 keV: this is not a feature related to the presence of the NG, but it is due to the activation of the ^{133}Xe isotope as described in the previous section. As the datasets are from different periods of the year, they are affected by different calibration operations, hence those features do not bring any information about the NG itself.

The effects due to the neutron activation need to be removed as we want to consider only the ER background induced by NG. Since we consider energies below 500 keV, as in Fig. 3.6a, the influence of neutron activation is obvious looking at the event rate evolution over time. Fig. 3.6b shows an exponential

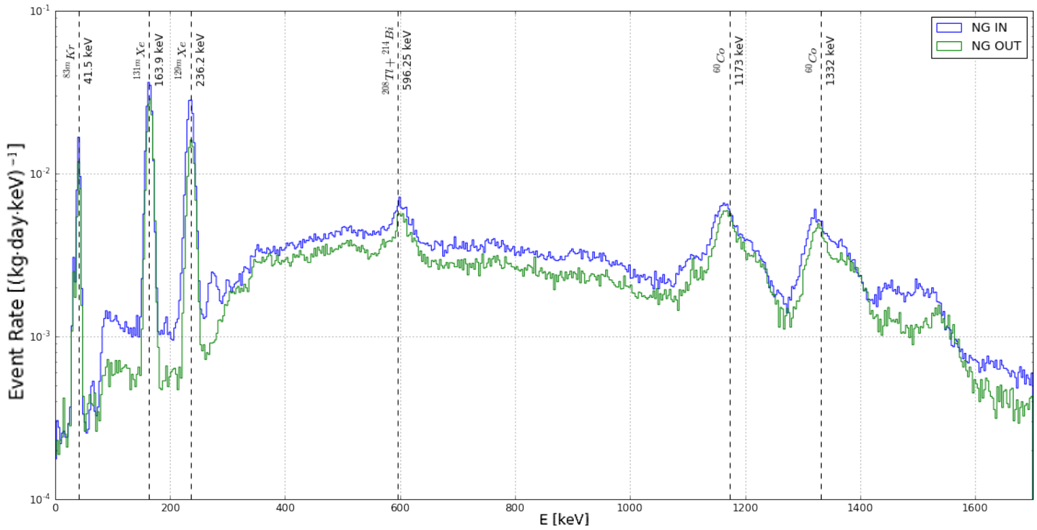

Figure 3.3: Combined energy spectrum for the electron recoil events when the NG is sitting inside the water tank (blue line) and when it is not (green line) in the energy region $[0, 1700]$ keV. The labels states the peak source. The knee around 80 keV is due to the activation of ^{133}Xe.

decrease right after NR calibrations, confirming that this energy region is influenced by neutron activation.

Selecting energies below 75 keV (Fig. 3.7a) the exponential decrease previously observed disappears, as Fig. 3.7b shows, and this means that the low energy range is unaffected by the neutron activation. A remaining feature is still present: the runs immediately following the ^{83m}Kr calibrations are characterized by a much higher rate event compared to the other runs. Indeed, the 41.5 keV Krypton line lies inside the considered energy range and, therefore, the energy range of the peak $[27, 50]$ keV is removed.

The final considered energy range is $[0, 27] \cup [50, 75]$ keV, where the event rate is stable (Fig. 3.8b) and it excludes any effect coming from calibration operations. The selected data are plotted in the $(\mathrm{cS1}, \mathrm{cS2_b})$ space in Fig. 3.8a. The differential event rate in this region, which is the number of events per day per kilogram of liquid target per unit of energy, is given by:

$$R\left[(\mathrm{kg} \cdot \mathrm{d} \cdot \mathrm{keV})^{-1}\right] = \frac{N_{\mathrm{events}}}{M_{\mathrm{FV}}\,[\mathrm{kg}] \cdot T_{\mathrm{exp}}\,[\mathrm{d}] \cdot \Delta E\,[\mathrm{keV}]} \tag{3.4}$$

where the SR0 fiducial mass is $M_{\mathrm{FV}} = (1042 \pm 12)$ kg, T_{exp} is the exposure time and ΔE is the energy interval. The final datasets have the following characteristics:

Dataset	$T_{\mathbf{exp}}$	$N_{\mathbf{events}}$	$R\left[(\mathbf{kg}\cdot\mathbf{d}\cdot\mathbf{keV})^{-1}\right]$
NG OUT	33 d 06:13:42	526	$(29.9 \pm 1.3)\cdot 10^{-5}$
NG IN	49 d 02:59:41	781	$(30.0 \pm 1.1)\cdot 10^{-5}$

where the difference between the event rate when the NG is sitting inside the water tank and when it is not is

$$\Delta R = R_{\text{IN}} - R_{\text{OUT}} = (0.1 \pm 1.7_{\text{stat}})\cdot 10^{-5}\,(\text{kg}\cdot\text{d}\cdot\text{keV})^{-1}\,.$$

As this result is consistent with a null difference, it is possible to conclude that the radioactivity of the NG materials gives a null contribution to the total ER background for low energies.

Because of the screening power of the LXe, a contribution to the background coming from the NG should be higher as we are closer to the source itself. Therefore the TPC was divided into two halves: the one closer to the NG and the farther one, as shown in Fig. 3.4. If a non-negligible contribution to the ER background is induced by the presence of this neutron source sitting inside the water tank, the event rate in the closer half of the TPC should be higher when the NG is displaced close to the cryostat. Considering only the NG IN dataset, the event rate in the closer half of the TPC is $R_{\text{close}} = (29.8 \pm 1.5_{\text{stat}})\cdot 10^{-5}\,(\text{kg}\cdot\text{d}\cdot\text{keV})^{-1}$ while in the farther half it is $R_{\text{far}} = (30.3 \pm 1.5_{\text{stat}})\cdot 10^{-5}\,(\text{kg}\cdot\text{d}\cdot\text{keV})^{-1}$. The difference between these values is

$$\Delta R = |R_{\text{close}} - R_{\text{far}}| = (0.5 \pm 2.1_{\text{stat}})\cdot 10^{-5}\,(\text{kg}\cdot\text{d}\cdot\text{keV})^{-1}$$

and it is consistent with a null difference, confirming that the NG sitting close to the cryostat is a negligible ER background source in the low energy region.

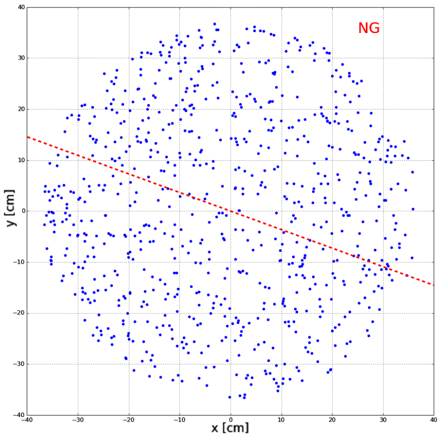

Figure 3.4: Spatial distribution of the events in the NG IN dataset inside the SR0 FV. The red line cuts the TPC in two halves: the top one labeled with 'NG' is closer to the NG, while the other is farther.

Increasing the fiducial mass, the outer volume of LXe is included in the fiducial volume and this implies a higher influence of the NG on the ER spectrum. The ER event rate in the considered region $[0, 27] \cup [50, 75]$ keV both for the 'NG IN' and 'NG OUT' dataset is shown in Fig. 3.5. The fiducial volume is defined as a cylinder with a fixed height of 83.9 cm as the SR0 FV and it can be modified by changing its radius. A non-negligible influence of the NG on the low energy background is observed for a fiducial mass above 1500 kg, corresponding to a radius of about 44.8 cm.

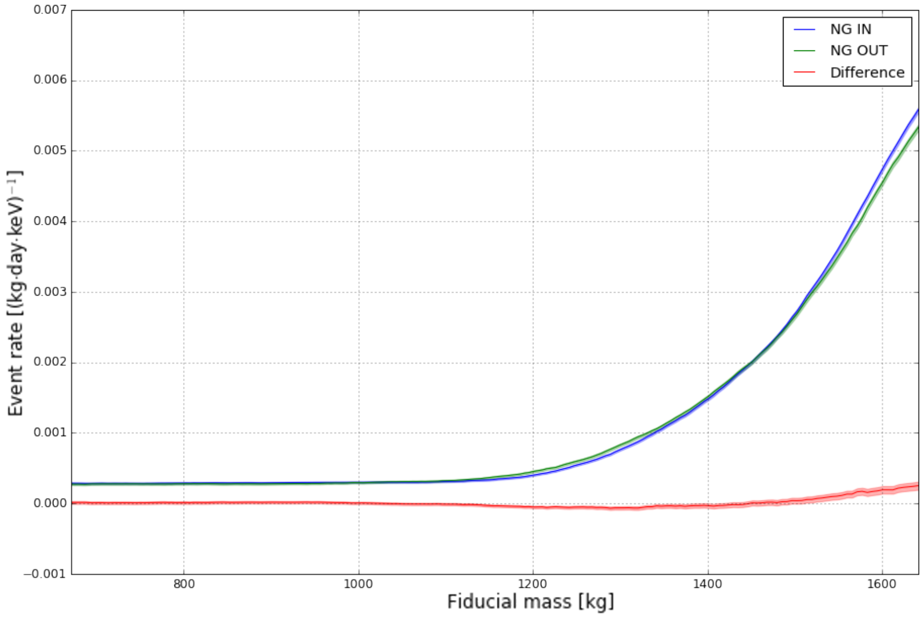

Figure 3.5: Low energy rate event as the NG is in the water tank (blue line) and when it is not (green line) as a function of the fiducial mass. The difference between them (red line) shows the influence of the NG as ER events source.

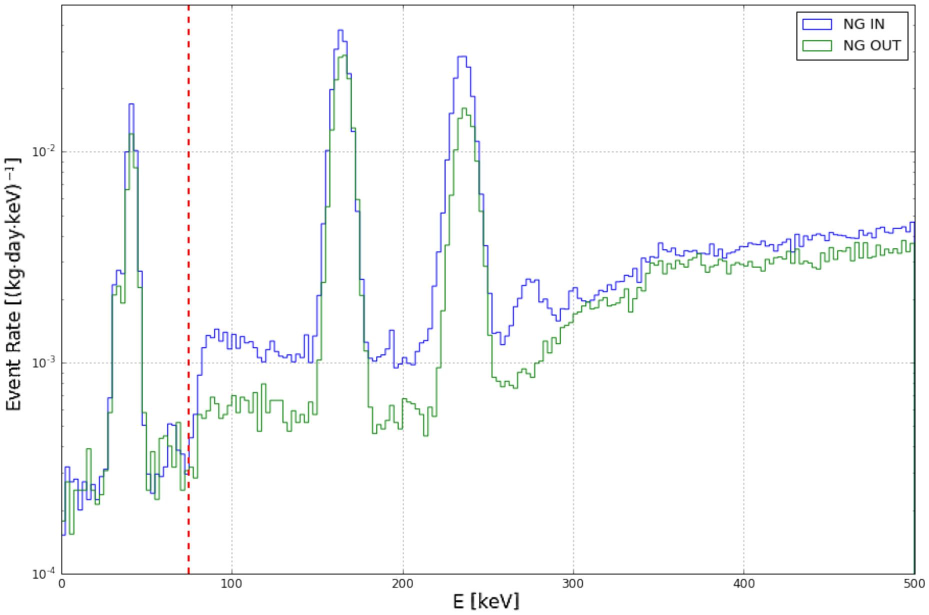

(a)

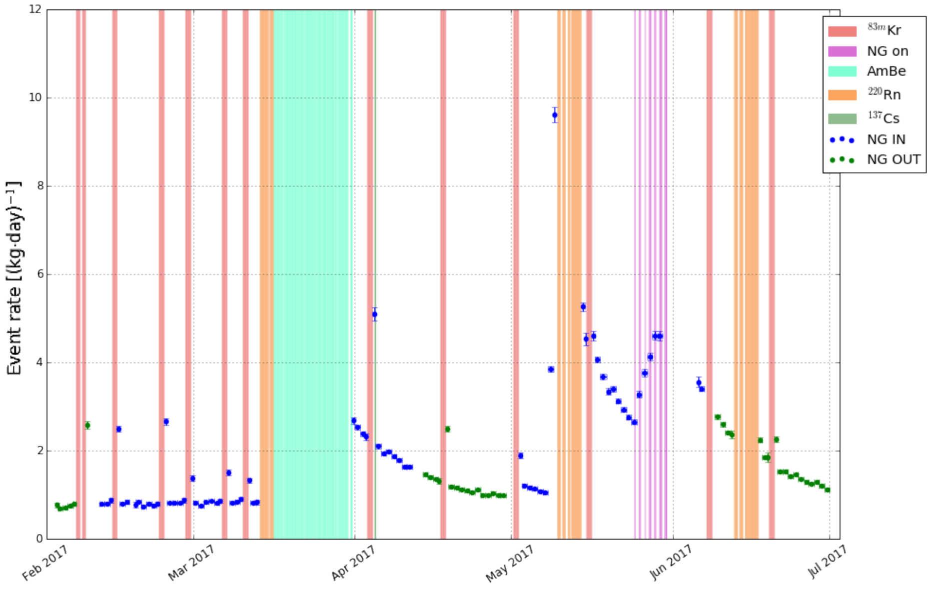

(b)

Figure 3.6: (a) Differential ER rate for energies below 500 keV. The red line is at 75 keV. (b) Total rate evolution for energies below 500 keV. The exponential decreases right after NR calibrations are a hint for neutron activation effects.

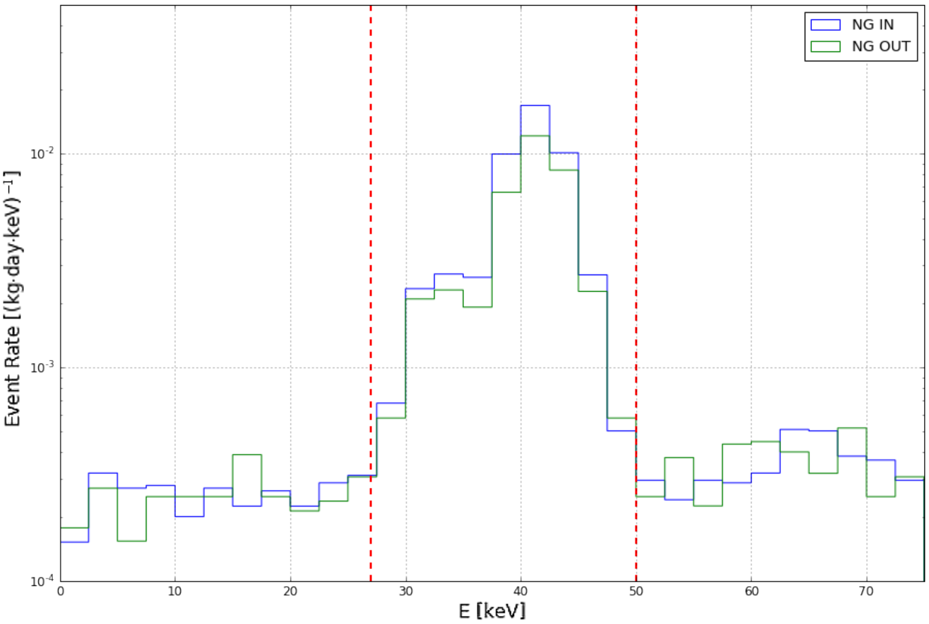

(a)

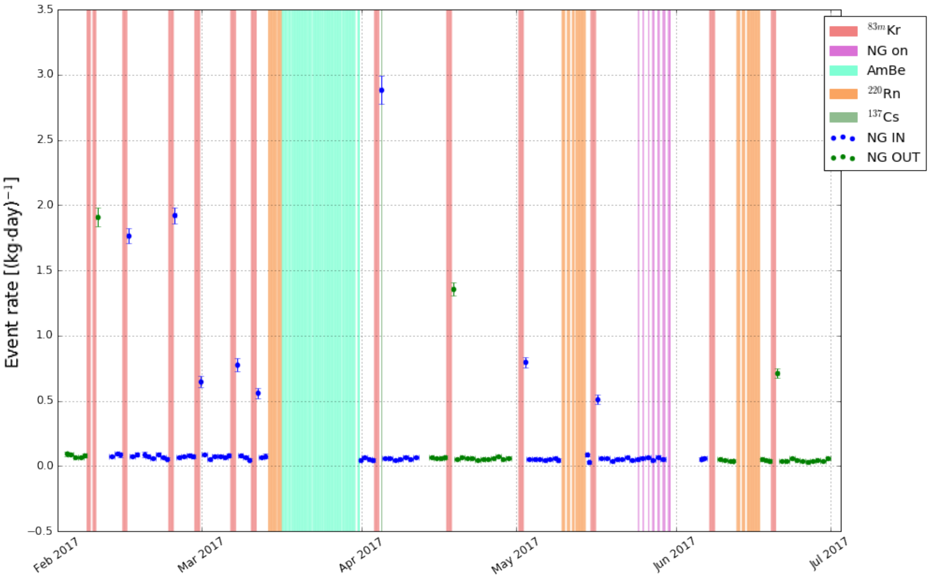

(b)

Figure 3.7: (a) Differential ER rate for energies below 75 keV. The ^{83m}Kr peak region is included in red lines. (b) Total rate evolution for energies below 75 keV. The high rates after the Krypton calibrations are a hint for its leakage.

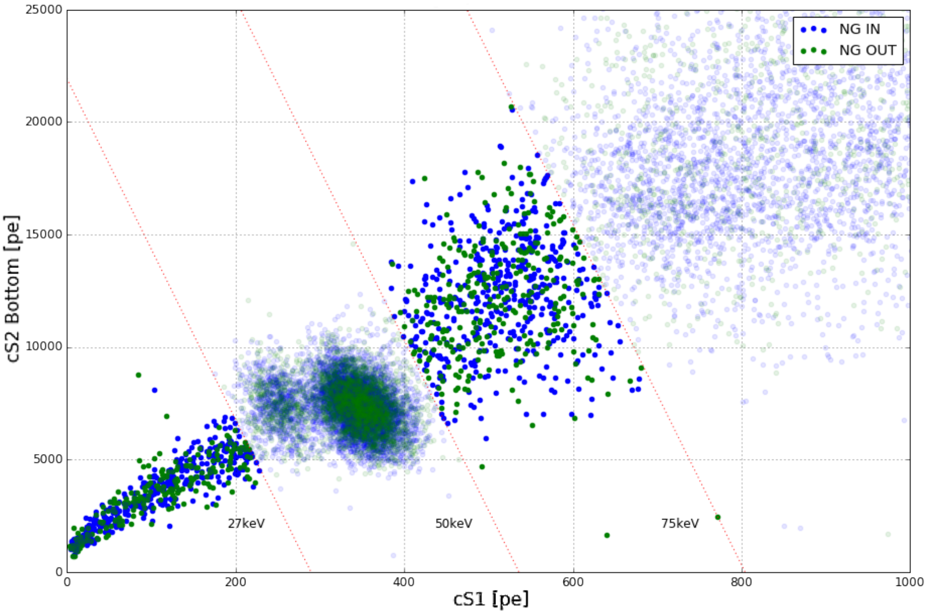

(a)

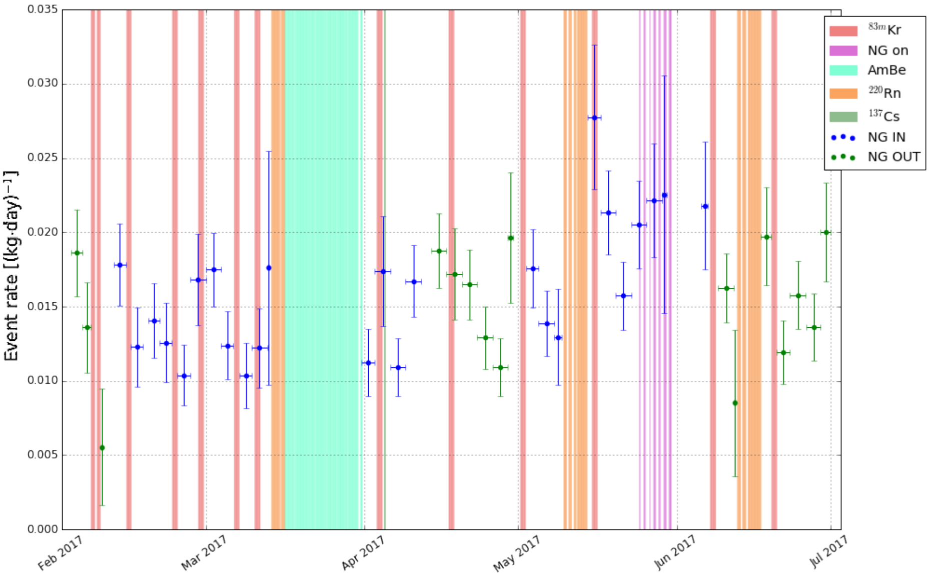

(b)

Figure 3.8: (a) Final selected data in the $(\mathrm{cS1}, \mathrm{cS2_b})$ space. (b) Total rate evolution for the final dataset: the stability over time excludes any contribution coming from calibration effects.

3.3 Neutron recoil background

The low energy ER background coming from the radioactivity of the NG materials has been excluded in the last section as it is negligible. The most dangerous background induced by neutron generator consists of radiogenic neutrons scattering once in the active volume of LXe causing a single scatter NR event, the typical signature of WIMP.

In this section such NR background is estimated: as first step it is necessary to measure the activity of ^{232}Th and ^{238}U chains as they are the main neutron sources, then the neutron flux emitted by the stainless steel making up the NG is simulated and the NR event rate is estimated. This NR background induced by the NG can be neglected as the worst case scenario is more than a order of magnitude lower than the radiogenic NR background predicted in the MC paper [79, 102].

3.3.1 Radiogenic neutrons

Radioactive chains in the detector materials can produce neutrons via spontaneous fission (SF) or secondary nuclear reactions (α, n) [116]. The main source of radiogenic neutrons are the ^{232}Th and ^{238}U chains, reported in Fig. 3.9. Also the ^{235}U chain is a potential radiogenic neutron source, but its

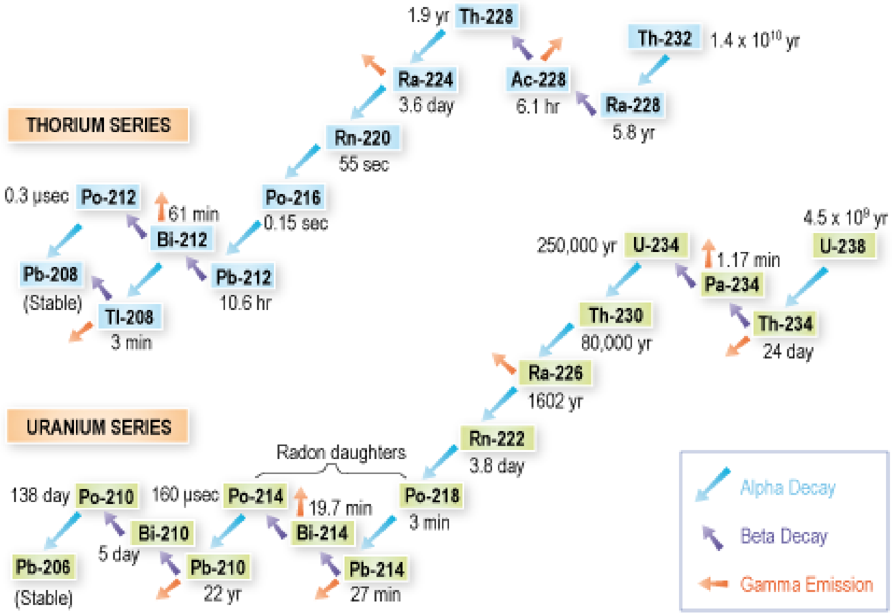

Figure 3.9: Radioactive decay chains for ^{232}Th and ^{238}U series.

natural abundance is about 1% of the ^{238}U.

Heavy nuclei that ordinarily undergo α decay may spontaneously fission into smaller nuclei with the emission of $\sim$2 neutrons in the MeV range per fission. As the rate of SF depends only on the fissioning nucleus, the neutron yield is independent of the material under consideration. The neutron yield is defined as the average number of neutrons emitted per unit of neutron energy per decay.

The main radiogenic neutrons production process is the nuclear reaction (α, n): as isotopes in the radioactive chains decay emitting an α particle, the other nuclei of the material could interact with it forming a compound nucleus which may decay by neutron emission. In this case the neutron yield strongly depends on the material in which the α emitter is: lighter nuclei are more likely to capture α particles forming compound nuclei as the high Coulomb barrier suppresses (α, n) interactions in heavy nuclei. This difference is shown by the neutron yield from PTFE and Copper in Figs. 3.10a and 3.10b: the SF contribution (dashed line) is the same for both materials, while the (α, n) is more important for the PTFE than for the copper, as the former has lighter nuclei than the latter.

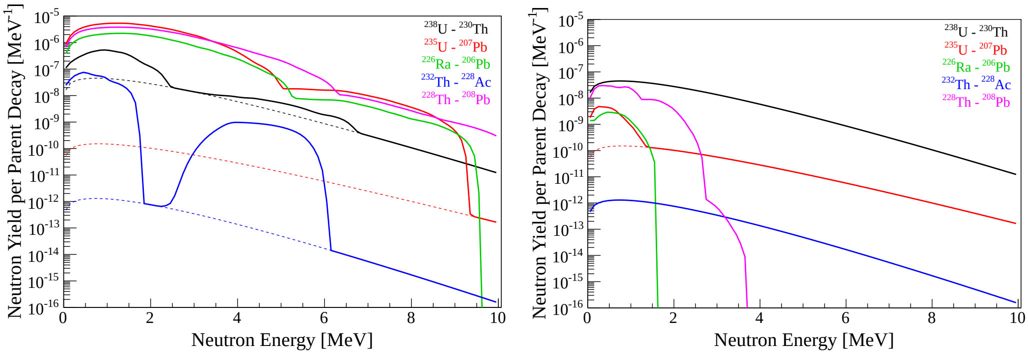

(a) **(b)**

Figure 3.10: Differential yield of radiogenic neutrons in PTFE (a) and copper (b). The solid line represents the sum of neutrons from SF and (α, n) reactions, the dashed line shows the contribution of SF only.

3.3.2 ^{232}Th and ^{238}U activity estimation

In order to estimate the NR background induced by radiogenic neutrons coming from NG, it is necessary to know the activity of ^{232}Th and ^{238}U in it. In both the series some isotopes are produced in an excited state: through de-excitation they emit monoenergetic MeV γ-rays, a clear signature of the

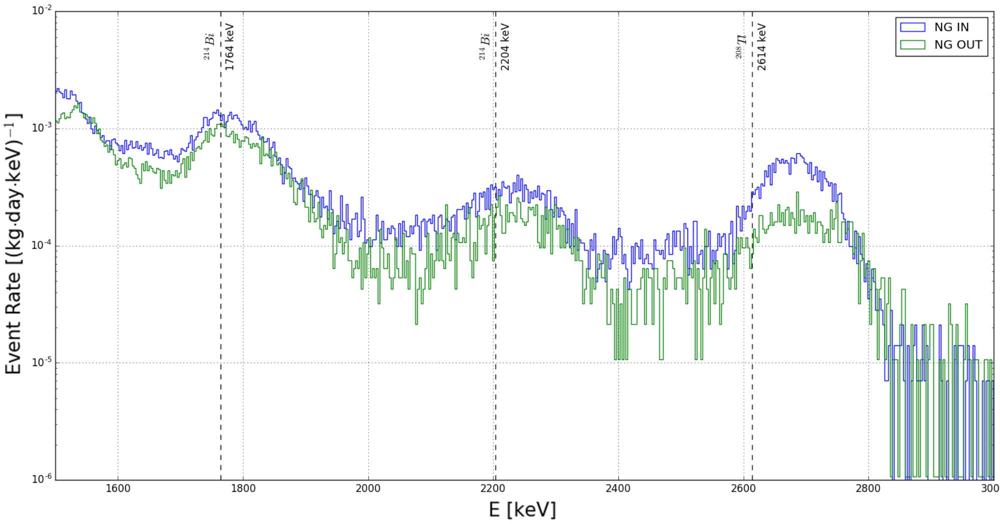

Figure 3.11: Combined energy spectrum for electron recoil events when the NG is sitting inside the water tank (blue line) and when it is not (green line) in the energy region $[1500, 3000]$ keV.

radioactive chains' activity. These monoenergetic gammas translate into high energy peaks in the CES: Fig. 3.11 shows the spectrum for energies higher than 1.5 MeV, where the three labeled peaks come from the radioactive chains of Thorium and Uranium. The two lower energy peaks at 1764 keV and 2204 keV come from the decay of ^{214}Bi into an excited state of ^{214}Po and they can be used to define the activity of ^{238}U, parent of these nuclei. In the same way, the highest energy peak at 2614 keV comes from the β-decay of ^{208}Tl into an excited state of the stable ^{208}Pb, the end point of the Thorium chain.

By matching the NG spectrum in Fig. 3.12 with MonteCarlo (MC) simulations of the radioactive chains in the NG materials, it is possible to estimate the ^{232}Th and ^{238}U activities. Inferring from these peaks the activity for the total radioactive chains requires the implicit assumption that the series are in secular equilibrium, as ^{208}Tl and ^{214}Bi belong to the last part of the chains. Since the materials making up the NG have not been screened, this assumption is the only viable way to estimate the activity of the first half of the chains. Nevertheless, disequilibrium is taken into account for the final results. The match can be done in two ways: by matching the single peaks as independent features or by matching the NG spectrum with the MC simulations in the energy range where the peaks lay. In the first case just the information coming from the peaks is considered, while in the other case all the information is: as the results are consistent for both the methods, the

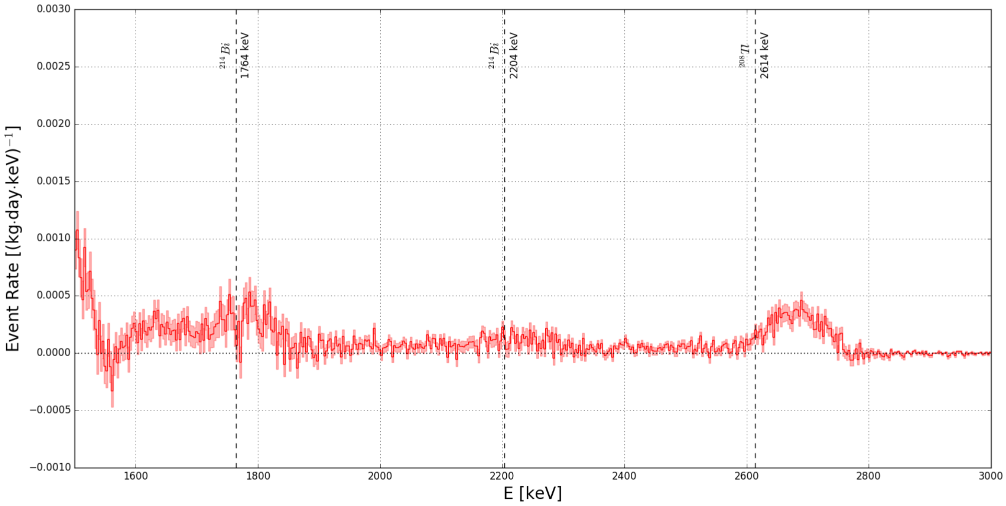

Figure 3.12: Energy spectrum contribution coming from NG given by the difference between the spectra with and without NG $\Delta\text{CES} = \text{CES}_{\text{IN}} - \text{CES}_{\text{OUT}}$. The high energy peaks shows the presence of Thorium and Uranium inside the NG.

values coming from the last one are eventually used.

MC simulation

GEANT4 is a toolkit used to simulate the production and propagation of particles through matter and their interactions [117]: the geometry description in the simulation of the XENON1T detector is implemented using this framework. The NG implementation consists of a couple of stainless steel cylinders, one inside the other: the outer and bigger cylinder is a 81.5 cm high container with an inner radius of 12.8 cm and 1.0 cm thick, while the inner one is the chamber fusion body with a height of 22.3 cm, an inner radius of 8.0 cm and a thickness of 2.0 cm. Using GEANT4 version 9.5.p01 it was possible to simulate 10^9 events both for ^{232}Th and ^{238}U radioactive chains, where an event is defined as the production of a new isotope by α or β decay following the Fig. 3.9.

Selecting only the single scatter events inside the FV, the differential background coming from the radioactive chain i is

$$R_i = \frac{N_i}{T_i \cdot M_{\text{FV}} \cdot \Delta E} \tag{3.5}$$

where N_i is the number of surviving events after the selection cuts in the energy range ΔE and M_{FV} is the fiducial mass. The effective livetime T_i

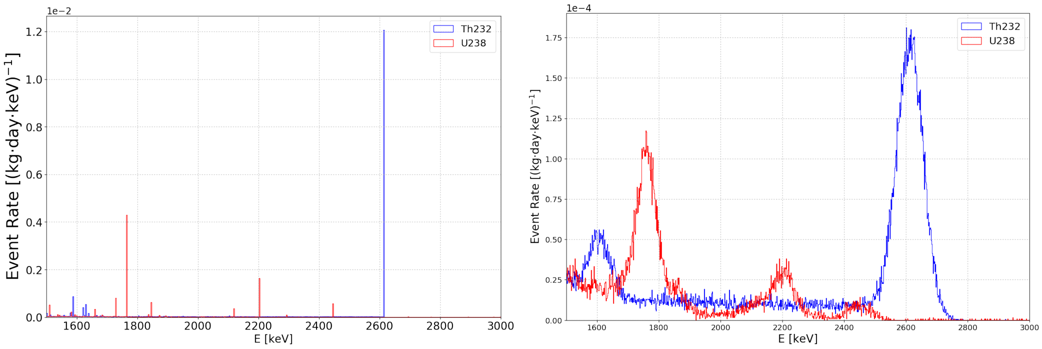

(a) **(b)**

Figure 3.13: Simulation of the differential ER event rate spectrum coming from Thorium and Uranium series in the NG, normalized to an activity of 1 Bq. In (a) the unsmeared spectrum, in (b) the smeared one with a 1.65% uncertainty on the energy reconstruction.

is the time we should wait to have a similar number of events in the real detector and it is given by:

$$T_i = \frac{N_i^{\mathrm{G}}}{N_i^{\mathrm{steps}} \cdot A_i} \tag{3.6}$$

where N_i^{G} is the total number of generated events in the MC simulation for the i chain, N_i^{steps} is the number of steps of that chain ($N_{\mathrm{U}}^{\mathrm{steps}} = 14$, $N_{\mathrm{Th}}^{\mathrm{steps}} = 10$) and A_i is the activity.

The final simulated spectra are shown in Fig. 3.13b: since the MC simulation stores the deposited energy, the energy resolution of the detector is not included. The spectra have to be smeared to take it into account: the energy resolution for high energies is approximated to $\sigma_E/E \simeq 1.65\%$. The final spectra for ^{232}Th and ^{238}U radioactive chains in the high energy range are plotted in Fig. 3.13b, where a total activity for both the series $A = 1$ Bq is considered. Matching the real data with the smeared MC simulations means finding the values of activity A_{U} and A_{Th} for which the simulation resembles the most the real NG data.

Single peaks matching

Most of the information about the activity of ^{232}Th is brought by the high energy ^{208}Tl peak at 2614 keV, while for ^{238}U it is brought by the ^{214}Bi peaks at 1764 keV and 2204 keV. Considering each peak individually it is possible to estimate the activity by fitting the peak both in the real data and in the

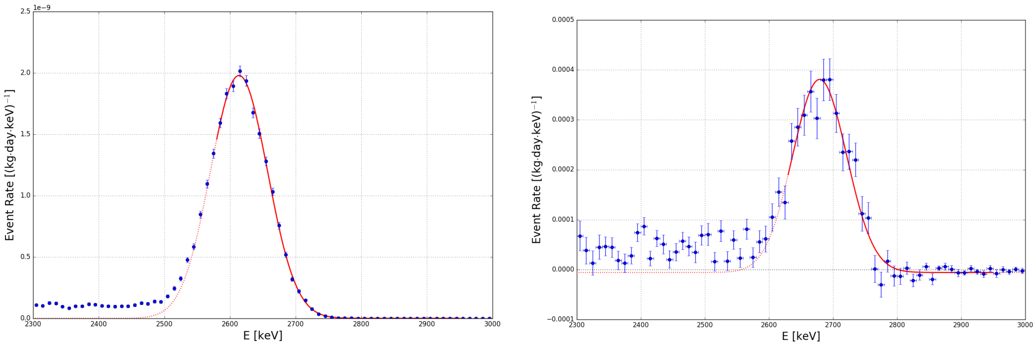

Figure 3.14: Gaussian fitting of the ^{208}Tl peak at 2614 keV in the MC data (left) and NG data (right). The solid line represents the fit range.

MC simulation spectra, where the latter is normalized to a unitary activity $A = 1$ Bq: the estimated activity is given by the ratio of the fitted amplitudes of the peaks. Indeed, it is possible to fit a peak as a Gaussian function and a constant offset

$$f\left(E\right) = C \cdot e^{-(E-\mu)^2/2\sigma_E^2} + k, \tag{3.7}$$

where the amplitude C is directly related to the activity of the source, while the constant k is a flat component representing other contribution to the event rate in that energy region. The ratio between the amplitude fitted from the real data and the fit of the normalized MC spectrum gives the value in Bq of the real activity:

$$A\,[\mathrm{Bq}] = \frac{C_{\mathrm{NG}}}{C_{\mathrm{MC}}\,(1\,\mathrm{Bq})}. \tag{3.8}$$

Comparing only the amplitudes allows to overcome the systematic shift in the reconstructed energy due to a not yet optimized performance of the data processor at high energies (while it is optimized for the WIMP search energy range)

Below the γ's energy, the Compton scattering represents a non-negligible contribution to the background, as evident in Fig. 3.14: the range to fit is therefore shifted towards higher energies. The ^{208}Tl is the first to be fitted and compared to the MC simulation as it is the highest in energy and, therefore, has no background coming from Uranium. In Fig. 3.14 the fits are shown for the MC data and the real data for the NG contribution to the spectrum (negative value are allowed as this is a difference between two spectra). Using the results of the fit shown in Fig. 3.14 and 3.8, the estimated activity for Thorium is

$$A_{\mathrm{Th}} = (2.27 \pm 0.10_{\mathrm{stat}})\ \mathrm{Bq}.$$

Once the Thorium activity is defined and its spectrum is fixed as background for the other peaks, it is possible to fit the ^{214}Bi peaks: the two peaks are independently matched to real data and the weighted average is considered for the Uranium activity. The fitting results for both the peaks are plotted in Figs. 3.15 and 3.16 and the weighted average between the two is

$$A_{\mathrm{U}} = (3.63 \pm 0.36_{\mathrm{stat}})\ \mathrm{Bq}.$$

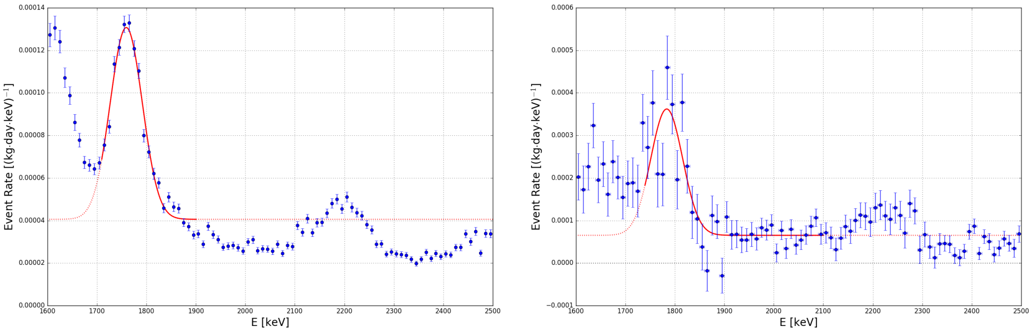

Figure 3.15: Gaussian fitting of the ^{214}Bi peak at 1764 keV in the MC data (left) and NG data (right). The inferred activity is (3.52 ± 0.42) Bq.

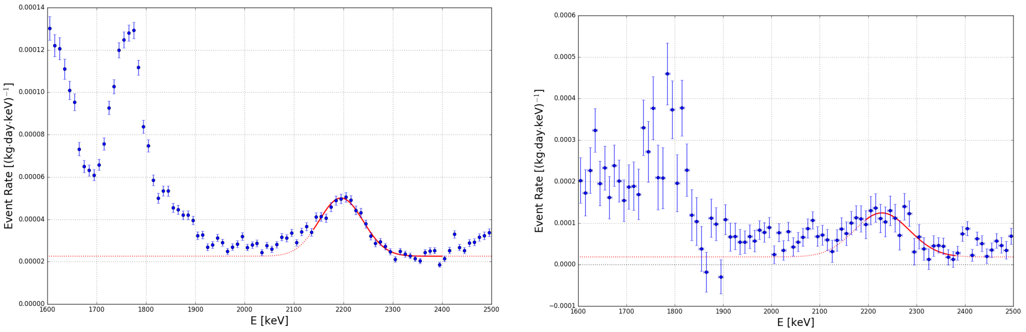

Figure 3.16: Gaussian fitting of the ^{214}Bi peak at 2204 keV in the MC data (left) and NG data (right). The inferred activity is (3.99 ± 0.74) Bq.

Combined spectra matching

Matching the single peaks reduces the entire matching just to a little energy range, wasting a lot of information coming from the rest of the spectrum. In order to exploit all the information, it is possible to match the NG real data with the MC spectra for Thorium and Uranium at the same time in the high energy range $[1.6, 2.8]$ MeV. This is chosen because the peaks lay in it and for lower energies the contribution from other isotopes, like ^{40}K or ^{60}Co, can not be neglected. Given the reference spectra $R^{\mathrm{U}}_{\mathrm{MC}}\left(E \,|\, 1\,\mathrm{Bq}\right)$ and $R^{\mathrm{Th}}_{\mathrm{MC}}\left(E \,|\, 1\,\mathrm{Bq}\right)$, matching consists to find the best scaling factors a_{Th} and a_{U} for which the total simulated spectrum

$$R_{\mathrm{MC}}\left(E\right) = a_{\mathrm{U}} \cdot R^{\mathrm{U}}_{\mathrm{MC}}\left(E \,|\, 1\,\mathrm{Bq}\right) + a_{\mathrm{Th}} \cdot R^{\mathrm{Th}}_{\mathrm{MC}}\left(E \,|\, 1\,\mathrm{Bq}\right) \tag{3.9}$$

matches the NG spectrum in the best way. The scale factors a_{Th} and a_{U} are the values of Thorium and Uranium activities in Bq units.

The first problem to face is the energy reconstruction: high energy peaks in the NG spectrum are shifted towards higher energy values and this requires to correct the MC spectrum to have the peaks matching in energy. A cubic function is used to correct the MC energy:

$$E_{\mathrm{CES}} = E_{\mathrm{MC}} + a \cdot \left(E_{\mathrm{MC}} - b\right)^3 \tag{3.10}$$

where the values a and b are fixed by comparing the MC energy peaks with the reconstructed energy. Once the MC spectrum is corrected to properly match the energy reconstruction, it is possible to match MC and real data following Eq. (3.9).

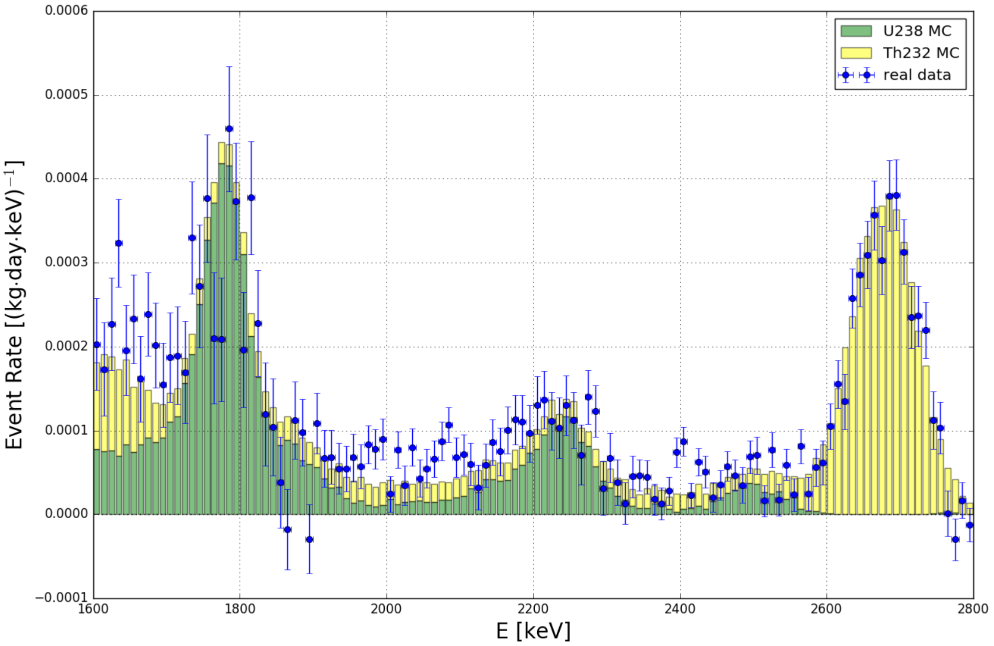

Figure 3.17: Matching the NG spectrum with the MC spectrum in the $[1600, 2800]$ keV range: in green the contribution from Uranium series, in yellow the contribution from Thorium series.

Minimizing the χ^2, the best fit parameters a_{Th} and a_{U} return the activities for ^{232}Th and ^{238}U radioactive chains. The results are shown in Fig. 3.17 and the activities are:

$$A_{\mathrm{Th}} = (2.30 \pm 0.08_{\mathrm{stat}})\ \mathrm{Bq} \qquad A_{\mathrm{U}} = (4.06 \pm 0.21_{\mathrm{stat}})\ \mathrm{Bq} \tag{3.11}$$

in good agreement with the values inferred with the single peaks.

As the fiducial volume is changed the activities should not vary since the content of these isotopes in the NG materials is independent on the volume considered for the analysis: indeed, a null dependence on the fiducial volume is observed in Fig. 3.18.

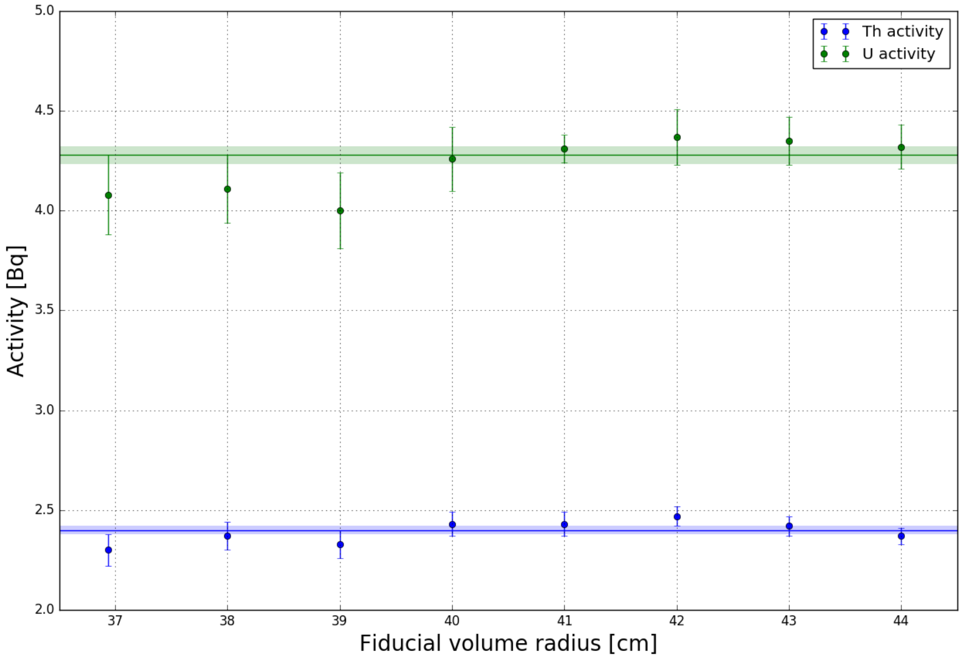

Figure 3.18: Increasing the radius of the FV the activity of Thorium and Uranium series for the NG does not change: the mean value is plotted with the 1σ band error.

3.3.3 Radiogenic neutrons from NG

Under the assumption of secular equilibrium, the activity for the ^{232}Th and ^{238}U series has been estimated. This information is fundamental to know the total neutron flux coming from the NG and its simulation with GEANT4 gives an estimation of the fraction of neutrons entering the TPC, mimicking WIMP signal. The identified radiogenic neutron sources are:

- ^{232}Th chain which is divided into two branches to take into account disequilibrium. The first part is $^{232}\text{Th} \rightarrow {}^{228}\text{Ac}$, almost negligible because of its low neutron yield, and the second part is $^{228}\text{Th} \rightarrow {}^{208}\text{Pb}$;
- ^{238}U chain in its branches $^{238}\text{U} \rightarrow {}^{230}\text{Th}$ and $^{226}\text{Ra} \rightarrow {}^{206}\text{Pb}$;
- ^{235}U chain, whose activity can be derived by the one of ^{238}U. Knowing the activity of ^{235}U and ^{238}U in a 1 g sample of $^{\text{nat}}$U, it is possible to scale the ^{238}U activity to estimate the unknown activity [118]:

$$A_{^{235}\text{U}} = \left.\frac{A_{^{235}\text{U}}}{A_{^{238}\text{U}}}\right|_{1\text{g}\,^{\text{nat}}\text{U}} A_{^{238}\text{U}} \simeq 0.0046 \cdot A_{^{238}\text{U}}. \tag{3.12}$$

MC simulation

A sample of $2 \cdot 10^7$ neutrons coming from the NG materials in the energy region $[0, 10]$ MeV has been produced using GEANT4 version 9.5.p01. Neutrons produced in the stainless steel walls follow the differential neutron yield shown in Fig. 3.19: they are simulated using a flat spectrum and then weighted based on the neutron yield in order to avoid an underpopulation for higher energies. The total neutron yield for the stainless steel is

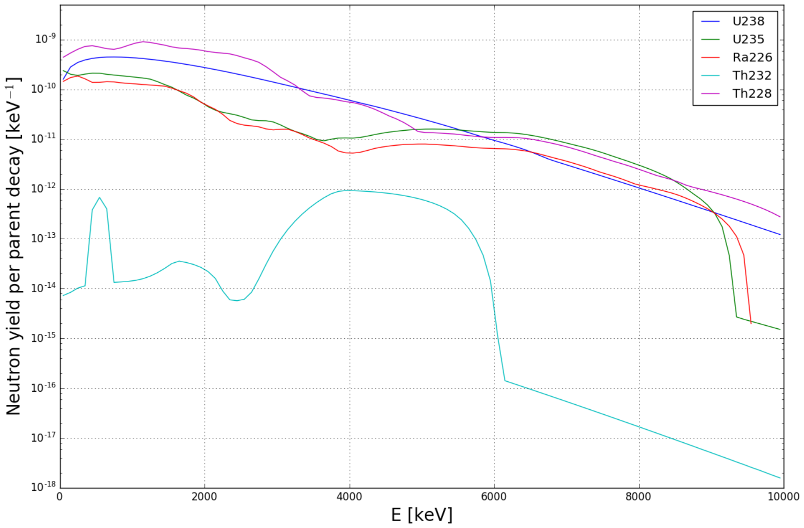

Figure 3.19: Differential yield of radiogenic neutrons in SS (stainless steel). The contribution coming from the first part of the Thorium chain is almost negligible compared to the other sources [119].

	^{238}U	^{235}U	^{226}Ra	^{232}Th	^{228}Th
Neutron yield [n/decay]	$1.1 \cdot 10^{-6}$	$4.1 \cdot 10^{-7}$	$3.1 \cdot 10^{-7}$	$1.8 \cdot 10^{-9}$	$2.0 \cdot 10^{-6}$

where the ^{232}Th immediately appears to be negligible.

NR background

The simulated neutrons propagate from the NG to the TPC: as they enter the active LXe volume they can elastically scatter with Xe nuclei faking a WIMP event in the FV. Only the single scatter NR events inside the SR0 FV are selected. The NR event rate from the source i is calculated like the ER event rate in (3.5), but weighting each event based on the initial energy of the neutron:

$$R_{\mathrm{NR},i} = \frac{\sum_\epsilon N_{i,\epsilon} \cdot \omega_\epsilon}{T_i \cdot M_{\mathrm{FV}} \cdot \Delta E} \tag{3.13}$$

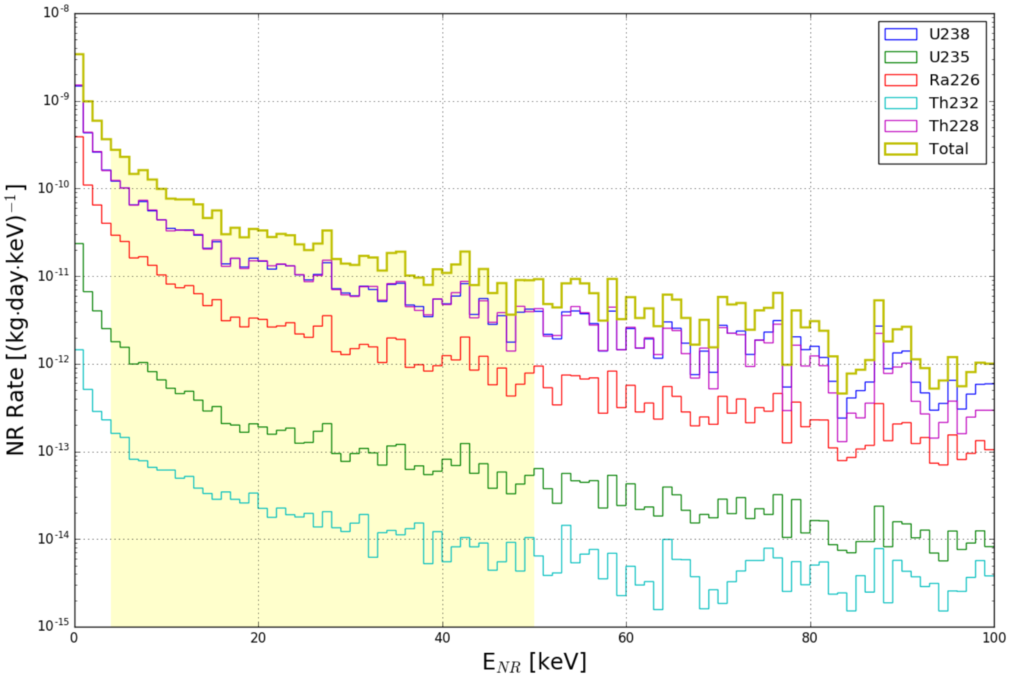

Figure 3.20: Energy spectrum of the NR background events in 1 t FV for NG induced radiogenic neutrons. The yellow shaded area is the region of interest for WIMP search.

where $N_{i,\epsilon}$ is the number of events in the energy range ΔE coming from source i and with an initial energy ϵ, therefore properly weighted with ω_ϵ, given by the ratio of the real neutron yield spectrum and the flat spectrum used to simulate neutrons.

Fixing the activity values for each source as previously measured, it is possible to estimate the energy spectrum for low energy nuclear recoils as shown in Fig. 3.20. The yellow shaded region represents the region of interest for NR events $[4, 50]$ keV: integrating the NR energy spectrum in this interval gives the total rate of NR events induced by the NG. Taking into account a systematic error of 17% on the differential neutron yield for stainless steel coming from SOURCES-4A code [119], the final expected NR event rate induced by the NG materials is

$$R_{\text{NR,NG}} = (7.7 \pm 0.4_{\text{stat}} \pm 1.3_{\text{sys}}) \cdot 10^{-4}\,\text{events/year}.$$

As the total NR background coming from the materials is 0.6 ± 0.1 events/year [79], the NG contribution is considered to be negligible. This is true also considering larger fiducial volumes as Fig. 3.21 proves: even considering almost the entire TPC the NR event rate is lower than the background coming from the material in the SR0 FV. This low rate can be explained by the fact that between the TPC and the NG there is water, while this effective neutron shied is absent for the other detector materials.

The secular equilibrium assumption comes from the fact that only the activity for the second part of both the radioactive chains of ^{232}Th and ^{238}U is estimated by the high energy peaks: there is not an equally clear signature for the chains $^{232}\text{Th} \rightarrow {}^{228}\text{Ac}$ and $^{238}\text{U} \rightarrow {}^{230}\text{Th}$, hence requiring equilibrium is the only reasonable possibility. A possible disequilibrium should be taken into account: while the neutron yield coming from the ^{232}Th chain is more than two orders of magnitude lower than the others and its contribution can be neglected, this is not the case for the ^{238}U chain. Assuming the worst case scenario for disequilibrium based on the stainless steel screening results $A\,(^{238}\text{U} \rightarrow {}^{230}\text{Th}) = 100 \cdot A\,(^{226}\text{Ra} \rightarrow {}^{206}\text{Pb})$ [120], it is still possible to neglect the contribution to NR background coming from radiogenic NG neutrons as the rate is

$$R_{\text{NR,NG}} = (3.4 \pm 0.2_{\text{stat}} \pm 0.6_{\text{sys}}) \cdot 10^{-2}\,\text{events/year}.$$

The estimation of the radiogenic NR background induced by NG is based on two assumptions: the secular equilibrium of the Th and U series in the NG and the stability over time of the detector conditions. The possible disequilibrium for the radioactive chains has already been taken into account by considering the worst case scenario. The other assumption is considered

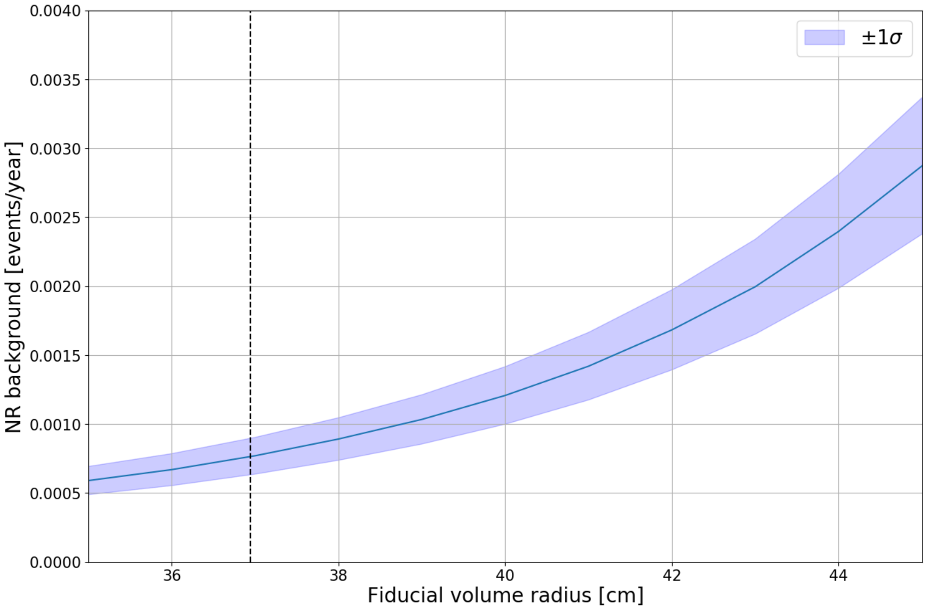

Figure 3.21: Total NR background rate from the NG as function of the FV radius. The black dashed line represents the SR0 FV radius at 36.94 cm.

to be legitimate as the detector response is stable for what concerns the light signal and it shows a little deviation from the stability for the charge signal, as discussed in Appendix A. The impact of that is negligible both for the NG induced background study, as the NG IN and NG OUT datasets are mixed in time, and for the DM search analysis. Indeed, taking into account the CY evolution over time for the ER band definition, no changes were observed.

Chapter 4

MC/data ER background comparison

For all experiments dealing with very low signal rates, such as DM or double beta decay searches, the knowledge of the background is essential. Knowing the detector background means being aware of its sources and of the contribution coming from each element of the detector. In this way it is possible to precisely simulate the detector background and to identify any deviation from what is expected: a simulation-driven approach to the study of background is to be preferred to a data-driven approach. Indeed, the latter well estimates the background, but it has no knowledge about its origin: when dealing with rare events it is necessary to know the nature of each signal in order to identify the interesting events. Moreover, data may be affected by a higher statistical fluctuation increasing the uncertainty on the knowledge of the background, a problem easily solved with simulations.

In a simulation-driven approach to the ER background it is fundamental the comparison between the MC simulations and the background data: this is necessary to identify every background source and activity. It is possible to define such values by matching the background spectrum for each possible source with the total ER background spectrum coming from real data.

In the first section of this chapter the GEANT4 implementation of the XENON1T detector is described. The second section is an overview of all the possible ER background sources which have been included in the MC simulation and in the third section the implementation of the ^{136}Xe double beta decay is described. In the end, the ongoing matching between MC simulation and background data is described and the preliminary results are shown.

4.1 GEANT4 simulation of XENON1T

The MC simulation of the XENON1T experiment is developed using the GEANT4 toolkit: the model was built according to the CAD construction drawings and its geometry tuned on the basis of the final detector [79]. In this section only the components included in the study of the ER background are discussed: some elements of the experiment are too far from the detector to contribute to the ER background, like the structure sustaining the cryostat or the water tank. Nevertheless the entire experiment is implemented in the GEANT4 model.

Cryostat

The TPC and the 3.2 t of LXe are contained in a vacuum-insulated double-wall cryostat made of 5 mm thick stainless steel, accurately chosen for its low radioactivity during a screening campaign for materials selection. The two vessels consist of a central cylindrical body closed by a dome on each side: the top domes are joint to the central part through two 45 mm thick flanges. The inner vessel (height 1.76 m, radius 56 cm), containing the entire volume of LXe and the TPC, is enclosed in an outer vessel (height 1.88 m, radius 65 cm): the vacuum between them is the best insulator to keep the Xenon in a liquid state. The cryostats are connected to the cryogenic and DAQ systems via a long double-wall vacuum insulated SS pipe starting from the central port in the top dome, while a smaller pipe is used for the HV connections. The GEANT4 implementation of the cryostats and the pipes is shown in Fig. 4.1: the images are made running geantinos simulations,

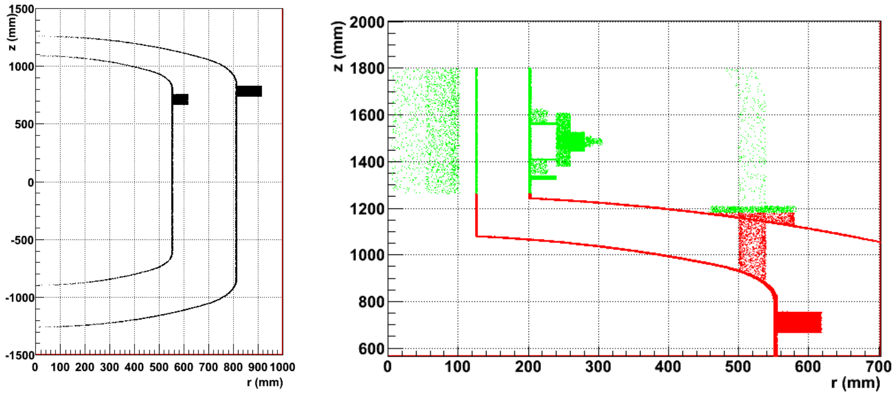

Figure 4.1: GEANT4 implementation of the inner and outer cryostats (left) and of the pipes connected to them (right).

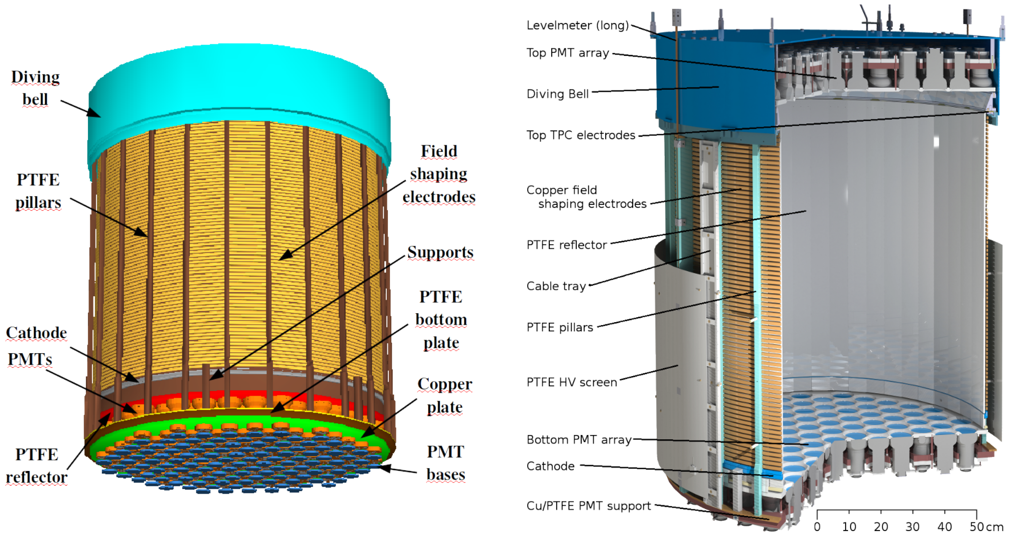

Figure 4.2: (left) External view of the GEANT4 implementation of the TPC (image extracted with the Meshlab software). (right) CAD illustration of the TPC.

pseudo-particle used to check the geometry.

TPC

The heart of the experiment is the TPC (height 97 cm, diameter 96 cm), hosting an active volume of 2 t of LXe acting as target for WIMPs and instrumented with two array of PMTs: the GEANT4 implementation and the CAD drawing are shown in Fig. 4.2. The approximately cylindrical structure is made of 24 interlocking polytetrafluoroethylene (PTFE) panels for a total radius of about 48 cm: this material optimizes the reflection of vacuum ultraviolet light maximizing the light collection. This is simplified in the GEANT4 implementation as an empty cylinder of PTFE. The electric field uniformity is obtained using *field shaping rings* connected between them through a resistor chain: a total of 74 thin oxygen-free copper (OFHC) rings are placed around the PTFE cylinder, each 10 mm high and 5 mm thick. To sustain the entire structure (PTFE inner panels + field shaping rings) 24 PTFE pillars are placed outside: they act as support for the rings. The pillars are supported both on the top and on the bottom by two PTFE rings, making the entire structure light-tight.

The electric field in the TPC, fundamental for electrons' drift, is generated through electrodes. The cathode and a screening mesh below it, used to protect the PMTs from the high field, are placed on the bottom of the

TPC: they are parallel wires made of gold-plated stainless steel mounted on a SS ring. At the LXe-GXe interface there is a stack of two hexagonal-etched gates: the grounded electrode slightly below the surface and the anode 5 mm above it, creating the proportional amplification region because of the high extraction electric field they induce. Above the anode a top screening grounded mesh is used to protect the top PMT array.

Since the LXe-GXe interface between the gate and the anode is fundamental for the S2 signal generation, the liquid level has to be kept under control: a diving bell with an adjustable overflow tube coupled to a linear motion feedthrough has been designed for this purpose. The bell is a cylindrical cap with a radius of about 52 cm and it is made of stainless steel, 5 mm thick on the top and 3 mm in the lateral part. This solution guarantees a 4π coverage since the LXe outside the bell can rise above the PMT array, acting as a passive shield and reducing the external background.

PMTs

The active volume of LXe inside the TPC is viewed by a bottom and a top array of PMTs. The bottom array consists of 121 PMTs directly immersed in LXe, right below the cathode mesh: the photomultipliers are arranged in an hexagonal structure to maximize the light collection efficiency. The top array is placed in GXe above the target volume and it is made of 127 PMTs arranged in concentric rings to improve the radial position reconstruction. For this reason the radius of the top array is about 4 cm larger than the TPC radius, thus in this way a good reconstruction can be achieved also at the edge of the TPC. The support structure for the arrays is made of two PTFE plates with a copper plate between them. The implemented geometry

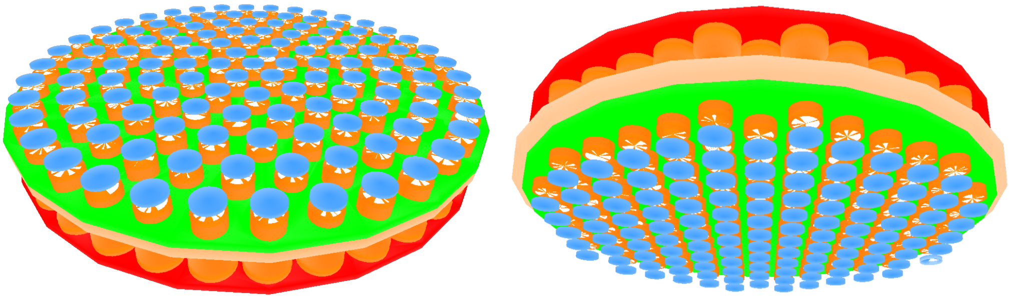

Figure 4.3: GEANT4 implementation of the top (left) and bottom (right) PMT arrays. The PMT structure is composed by two PTFE plates (green and red) and a copper plate (pink) between them. For each PMT (orange) its voltage divider circuit (blue) is shown.

for the simulation is shown in Fig. 4.3.

The photomultipliers are 3" Hamamatsu R11410-21 PMTs, specifically developed for XENON1T to have a high quantum efficiency for Xenon scintillation light ($\sim 35\%$ [121]) and a low radioactivity, measured during the screening campaign [122]. A single PMT is 12.3 cm long and its main components are a Cobalt-free Kovar body, a quartz window with a 7.6 cm radius, a ceramic stem and a photocathode: they are implemented in the GEANT4 simulation, while smaller parts (e.g. dynodes and the getter) are not included since their contribution to the total radioactivity is negligible. The voltage divider circuit for each photomultiplier is mounted on a 7 mm thick base made of Cirlex and placed 14 mm away from the PMT: it is modeled as a simple thin disk.

Physics list in GEANT4

The radioactive decays of nuclei leading to background events are simulated using `G4RadioactiveDecay` GEANT4 physics list, including α, β^+, β^- decays and electron capture. Half lives, nuclear level structures, decay branching ratios and energies of decay processes are data-driven, taken from Evaluated Nuclear Structure Data Files (ENSDF) [123], which is maintained by the National Nuclear Data Center at the Brookhaven National Laboratory (BNL). Isomers from nuclear decays are handled through the `G4PhotonEvaporation` list: prompt de-excitation gammas from E1, M1 and E2 photon transitions are included. For gamma and electron interactions the `Livermore` physics list is chosen as it is suited to describe low energy electromagnetic interactions, while for low energy neutrons (<20 MeV) the `High Precision` list is preferred because it uses the neutron data files G4NDL 3.13 with thermal cross sections, based on the ENDF/B-VI/B-VII databases [124].

The tracking of the particles is divided into steps, whose length depends on the type and energy of the particle and on the characteristics of the medium. For each step inside the LXe target, the position, time, deposited energy, particle type and the process responsible for the energy loss is stored. All this information is necessary to eventually process the MC simulation in order to have a final output simulating what is expected in the detector.

4.2 XENON1T ER background sources

The science goals for XENON1T require an extremely low NR and ER background: while the nuclear recoils are the most dangerous events since they can mimic the WIMP signals, also electronic recoils may leak into NR region simulating a WIMP recoil. For this reason it is fundamental to reduce the ER background through a selection of low radioactive materials and selection cuts during the data analysis. All the relevant ER background sources are considered in the following sections: radioactive contamination of the detector materials, radioactive isotopes intrinsic to the LXe and the irreducible solar neutrinos scattering off electrons[1].

In the following the results from the ER background prediction for the XENON1T experiment are taken into account [79], where the materials' activity come from the screening campaign measurements [120] and the final predicted ER background spectrum is shown in Fig. 4.4.

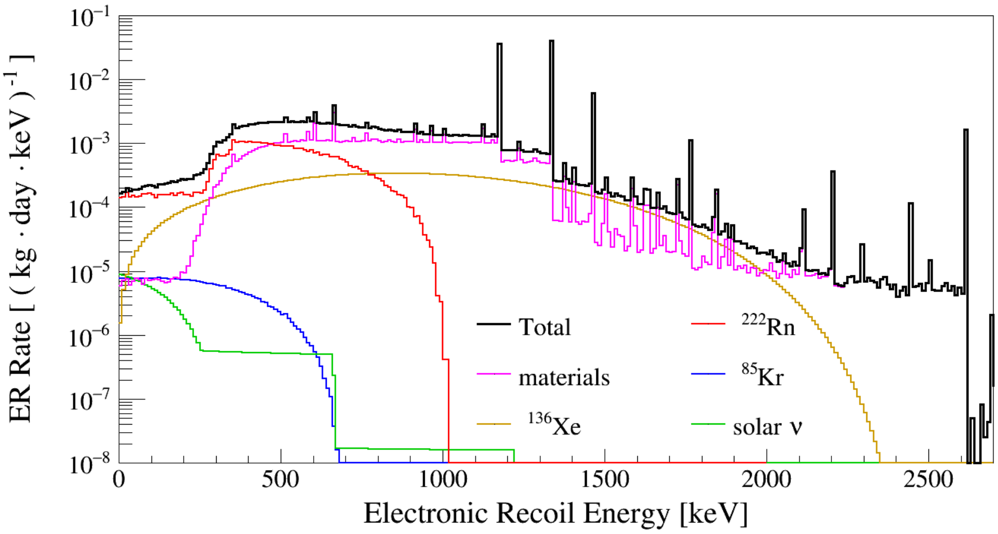

Figure 4.4: Energy spectrum of the total ER background rate in the 1 t fiducial volume.

4.2.1 Radioactivity of detector materials

A screening campaign for selecting the purest materials in terms of radioactivity has been performed before the construction of the XENON1T experiment, using MC simulations to define the acceptable levels. Two complementary techniques were exploited to measure the activity of the main radioactive isotopes in the materials: Germanium detectors and mass spectrometry. Ge-based detectors are extremely sensitive to most of the radiogenic nuclides

---

[1] The background induced by solar neutrinos can be reduced using directional detectors, removing those events coming from the Sun.

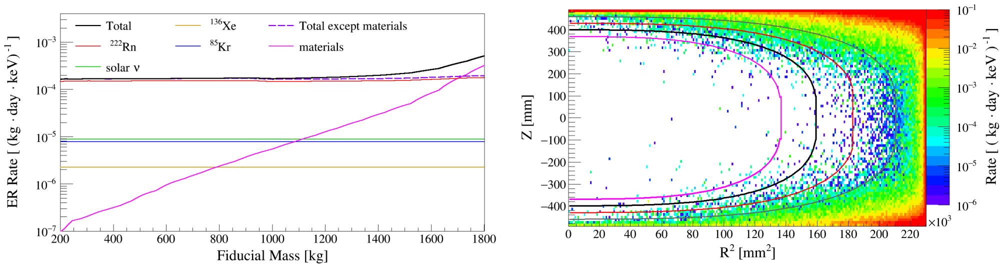

(a) **(b)**

Figure 4.5: (a) Average ER background rate in the energy range $[1, 12]$ keV as a function of the fiducial mass. (b) Spatial distribution of the ER background events from the detector materials in the $[1, 12]$ keV range. The 800 kg, 1000 kg, 1250 kg and 1530 kg fiducial volumes are indicated with the respective purple, black, read and brown lines.

relevant for the ER background: ^{40}K, ^{60}Co, ^{137}Cs, the ^{232}Th series and the second part of the Uranium series, ^{226}Ra and daughters. The first part of the ^{238}U chain has few and low energy gammas, therefore Ge detectors as Gator at LNGS [125] are unable to detect its presence: for this reason mass spectrometry techniques (e.g. ICP-MC or GDMS [120]) are used to directly count the amount of primordial nuclei of ^{238}U and ^{232}Th.

Thanks to the shielding power of LXe and the position reconstruction in three dimensions, it is possible to reduce this background through the selection of a fiducial volume, i.e. an inner detector region where the radiation coming from the material is reduced by the LXe shield. As the fiducial mass increases, the contribution to the total ER background coming from the materials is more relevant as shown in Figs. 4.5. Based on the screening results, the MC simulations predicted the spectrum in Fig. 4.6a in a 1 t fiducial volume: below 200 keV the spectrum is flat, while for higher energies the Compton scattering together with photo-absorption lines give a non-flat spectrum. The most clear lines, labeled as well in Fig. 3.3, are 1173 keV and 1333 keV from ^{60}Co, 1460 keV from ^{40}K, the high energy gammas at 1764 keV and 2204 keV from ^{214}Bi and at 2614 keV from^{208}Tl.

From the MC simulation of the experimental setup, the highest contribution to the total ER background from materials comes from the stainless steel of the cryostat (shells and flanges), mainly from its ^{60}Co contamination. The contribution coming from each element of the detector is shown in Fig. 4.6b: the PMTs contribute 23% with their bases, while 15% is due to the other SS component inside the TPC (e.g. diving bell and electrode rings).

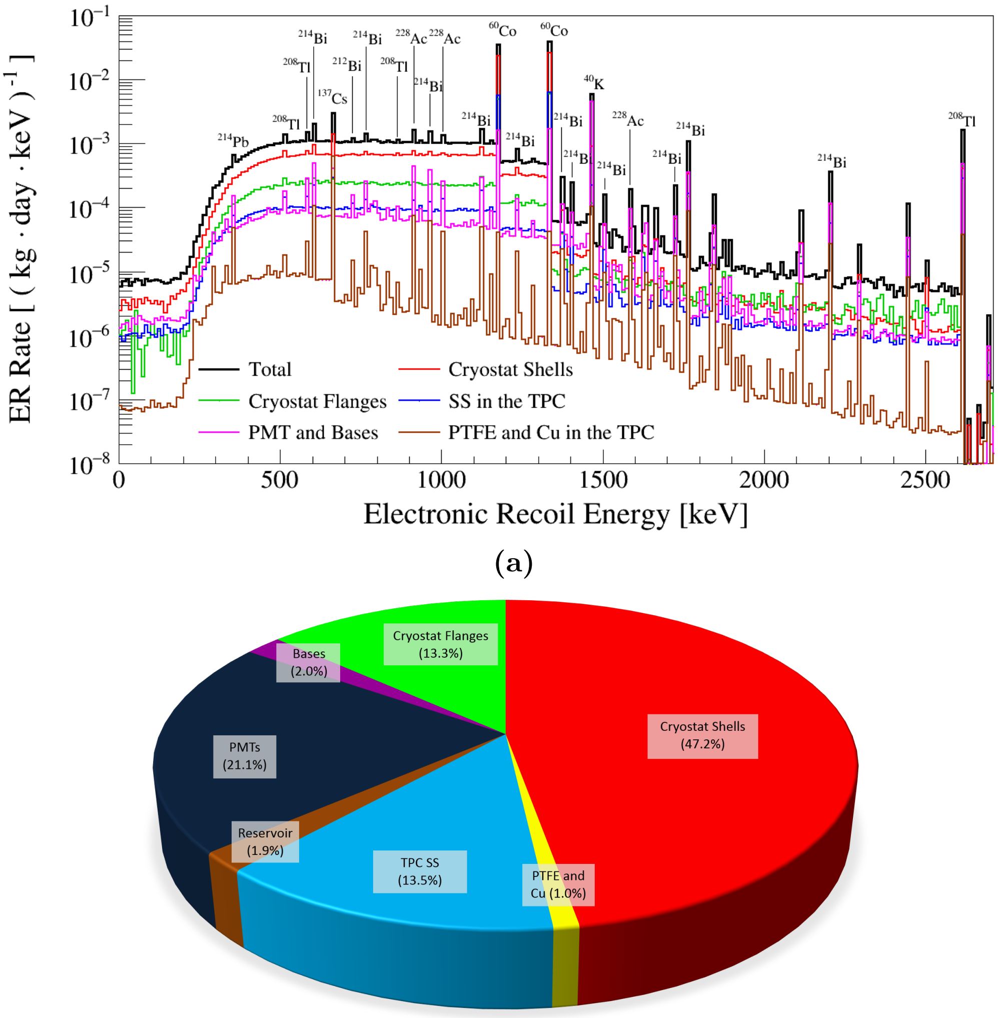

(a)

(b)

Figure 4.6: (a) Energy spectrum in 1 t FV of the total expected ER background from the detector materials. (b) Contribution to the ER background from the various components of the detector.

4.2.2 Intrinsic contaminants

The main contribution to the ER background comes from intrinsic sources, i.e. radioactive nuclides evenly distributed in the LXe. Since there is no long-lived radioactive Xenon isotope, with the exception of the double beta emitter ^{136}Xe with $T_{1/2} = (2.17 \pm 0.06) \cdot 10^{21}$ y, the intrinsic background sources are ^{85}Kr and ^{222}Rn, coming from the Uranium radioactive chain.

^{85}Kr

Xenon is extracted from the atmosphere with a typical $^{\mathrm{nat}}$Kr/Xe concentration at the ppm level. Natural krypton contains traces of the radioactive isotope ^{85}Kr: it decays β^- into ^{85}Rb with a half-life of 10.76 years and an end-point energy of 687 keV. Its natural activity in the Earth's atmosphere is estimated to be 0.09 PBq, as it is produced via neutrons in cosmic rays interacting with the Krypton-84 in the atmosphere through the nuclear reaction $^{84}\mathrm{Kr}\,(\mathrm{n},\gamma)\,^{85}\mathrm{Kr}$ [126]. However, the main sources for atmospheric ^{85}Kr are reprocessing facilities for nuclear fuel, mainly located in the northern hemisphere: such anthropogenic sources generate an atmospheric inventory that is at least 4 orders of magnitude larger than the natural. Most of the radioactive Krypton isotopes are emitted during the extraction of Plutonium for either civilian or military purposes: 3 fission processes of ^{235}U out of 1000 lead to the production of a ^{85}Kr nuclide. Almost all the ^{85}Kr remains in the fuel rods and when they are reprocessed it is emitted in the air. Indeed, estimates for its yield from reprocessing of 1 kg Pu range from 10 to 35 TBq [127]. Contributions to the radioactive Krypton in the atmosphere come also from nuclear tests and nuclear incidents, for example the Černobyl' explosion in 1986 yielded to a global activity of 35 PBq, as measured in 2000, four-

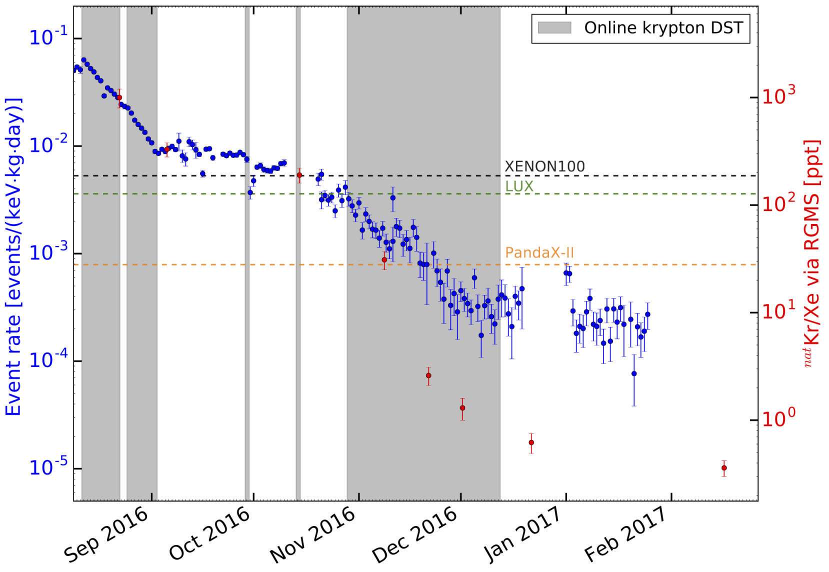

Figure 4.7: The evolution rate for events in the energy range $[0, 200]$ keV is shown in blue, while the data of Krypton concentration in LXe measured through RGMS are shown in red. The gray intervals represent the Krypton distillation periods.

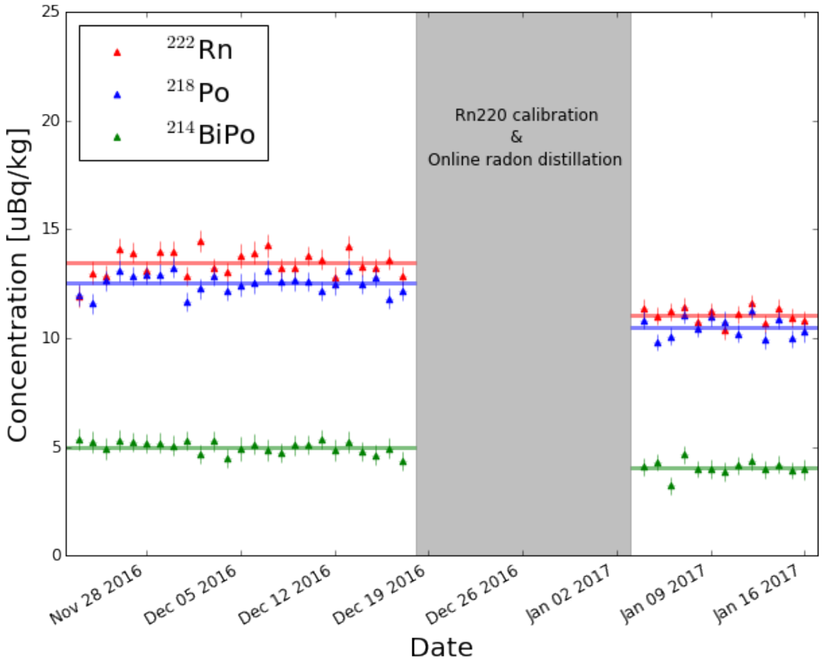

Figure 4.8: Concentration of the main radioisotopes of the ^{222}Rn chain before and after the online Radon distillation.

teen years later. As of 2009 the total amount of ^{85}Kr in the atmosphere was estimated at 5500 PBq due to anthropogenic sources, for a relative isotopic abundance in Europe of $2 \cdot 10^{-11}$ g/g [128].

This background is reduced using a dedicated cryogenic distillation column: the vapor pressure of Krypton is about 10 times higher compared to the Xenon at $-96\,°\mathrm{C}$, therefore the more volatile Krypton will gather at the top of the distillation column, while the Kr-depleted Xenon will be collected at the bottom. Given a $^{\mathrm{nat}}$Kr/Xe concentration of < 0.2 ppm in commercial high-purity Xenon gas, a Kr reduction factor of 10^5 is required to reach the design goal of < 0.2 ppt: a month after the first science run of XENON1T a concentration of ^{85}Kr/Xe $\simeq (0.36 \pm 0.06)$ ppt was reached [77]. The decrease of Krypton contamination during the distillation process is shown in Fig. 4.7, where the concentration of Krypton in LXe is measured via RGMS (Rare Gass Mass Spectroscopy). For concentrations higher than about 1 ppt the event rate for low energies is dominated by it.

^{222}Rn

The main intrinsic source of background in LXe, given the Kr85 contamination achieved after the cryogenic distillation, comes from the decay of ^{222}Rn daughters, part of the ^{238}U. The Radon can be emanated from the components of the detector and of the gas system or it can diffuse through the vacuum seals, then thanks to its long half-life (3.8 days), it can homogeneously distribute in the LXe volume. This background cannot be reduced by fiducialization of the volume, therefore the materials need to be selected for their low radon emanation and an online distillation is required to reach a contamination of the order of 10 μBq/kg. The online distillation is possible by exploiting the Krypton distillation column in inverse mode, since the Radon is less volatile than the Xenon: the ^{222}Rn contamination was reduced by $\sim$ 20% thanks to this technique, as Fig. 4.8 shows.

The most dangerous contribution comes from the β decay of ^{214}Pb to the ground state of ^{214}Bi (BR=10.9%), with an end-point energy of 1019 keV and a half-life of about 27 minutes. Decays into excited states do not represent a low energy background since the measured energy of the event is the sum of the β electron and the γ from the prompt de-excitation. However, especially if the decay happens close to the borders of the active LXe region, decays to excited levels of ^{214}Bi are also potentially dangerous: the accompanying γ ray may escape the detector without being detected. This is responsible

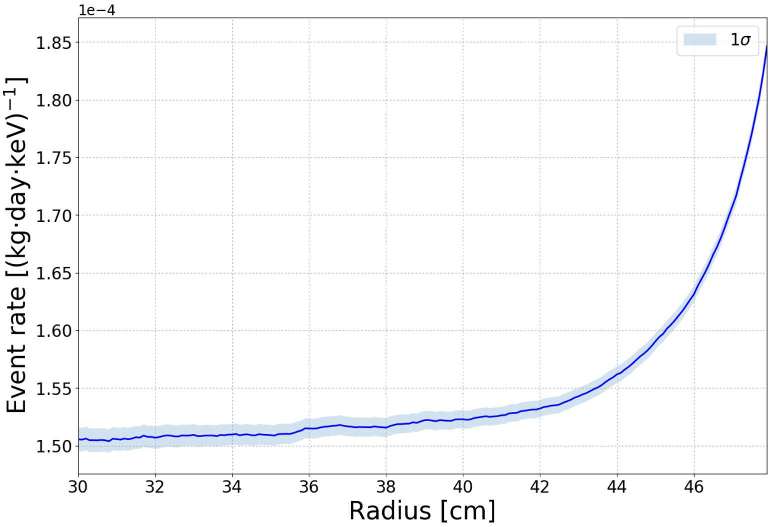

Figure 4.9: Low energy ER background event rate in the energy region [1, 12] keV coming from the most dangerous ^{222}Rn's daughter, ^{214}Pb. As the radius increases the probability for a γ to escape the TPC without being detected increases.

for the slightly higher background rate from ^{222}Rn at larger fiducial volume in Fig. 4.5a. A simulation of ^{214}Pb β decay in the whole volume of LXe is reported in Fig. 4.9: the event rate in the energy range of interest for WIMP search $[1, 12]$ keV increases as a larger radius for FV is selected, with a maximum increase of about 20%.

The other β emitter in the chain is ^{214}Bi, decaying into ^{214}Po in almost 20 minutes: it can be easily removed by looking at the time correlation with the α decay of its daughter, which occurs with a half-life of $164\,\mu$s. In addition, during the XENON100 phase it was observed that after the α decay, the recoiling ions (^{218}Po and ^{214}Pb) drift towards the cathode [129], lowering the background with respect to the assumption of a uniform distribution in LXe.

^{136}Xe

Natural Xenon contains 8.9% of ^{136}Xe: it is the only radioactive isotope of Xenon as it decays double β into ^{136}Ba with the emission of two electron anti-neutrinos $\bar{\nu}_e$ and a Q-value of about 2458 keV. The most recent measurement of its half-life $\mathrm{T}_{1/2} = (2.17 \pm 0.06) \cdot 10^{21}\,\mathrm{y}$ [130] comes from the EXO-200 experiment, a liquid phase TPC using 200 kg of enriched Xenon in the isotope 136.

The total expected background coming from this source can be estimated knowing the natural abundance $a_{^{136}\mathrm{Xe}/^{\mathrm{nat}}\mathrm{Xe}}$ and its half-life:

$$R_{^{136}\mathrm{Xe}} = \frac{n_{^{136}\mathrm{Xe}}}{\tau} = \frac{\mathrm{N_A} \cdot a_{^{136}\mathrm{Xe}/^{\mathrm{nat}}\mathrm{Xe}}}{\tau \cdot \langle \mathrm{A_{Xe}} \rangle} \tag{4.1}$$

where $\tau = \mathrm{T}_{1/2}/\ln(2)$ is the mean life and $n_{^{136}\mathrm{Xe}}$ is the number of ^{136}Xe per unit of fiducial mass, estimated knowing the atomic mass of the Xenon $\langle \mathrm{A_{Xe}} \rangle = 131.29\,\mathrm{amu}$ and the Avogadro constant $\mathrm{N_A} = 6.022 \cdot 10^{23}\,\mathrm{mol}^{-1}$. This estimation returns the event rate per unit of fiducial mass integrated for all the energies:

$$R_{^{136}\mathrm{Xe}} = (3.56 \pm 0.01) \cdot 10^{-1}\ (\mathrm{d} \cdot \mathrm{kg})^{-1}\,. \tag{4.2}$$

The double beta decay was implemented as a pair of electrons emitted in the same position following a theoretical spectrum and angular distribution: this procedure is described in Section 4.3.

4.2.3 Solar neutrinos

Electron neutrinos produced in the Sun may scatter elastically off the electrons in the active volume of LXe, producing an isotropic ER background in

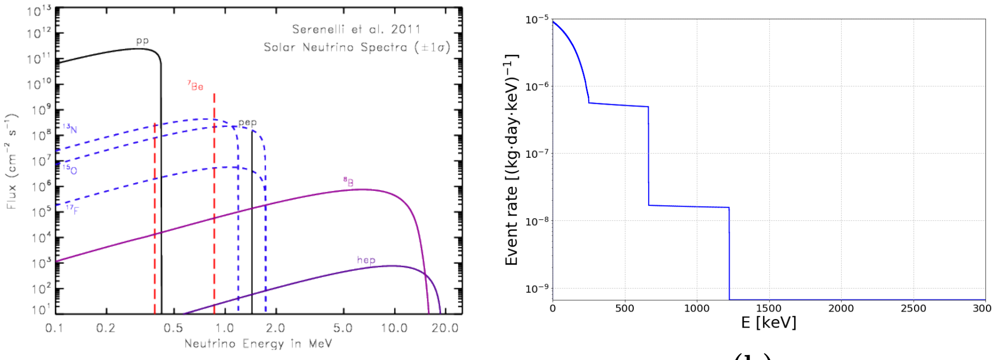

(a)

(b)

Figure 4.10: (a) Energy spectrum of solar neutrinos arriving on Earth, based on calculations in [132]. (b) Electronic recoil energy spectrum coming from solar neutrinos elastic scattering with electrons in LXe.

the low energy region. The recoil energy spectrum is shown in Fig. 4.10b: comparing it to the solar neutrinos flux of Fig. 4.10a the step-like structure can be explained by the neutrinos coming from the p-p reaction, representing the 92% of the interactions, and from the ^{7}Be contributing to 7% of the total background.

This background source cannot be reduced in experiments like XENON1T and the only way to mitigate its impact is to improve the ER discrimination power. It can be reduced using directional experiments, rejecting all the events coming from the Sun as it is the major source of neutrinos. Neutrinos are also an irreducible background source for nuclear recoils as they may scatter coherently off nuclei (Coherent Neutrino-Nucleus Scattering, CNNS): this is the main limit to direct search experiment sensitivity as they perfectly mimic the WIMP signal.

Taking into account neutrino oscillation $\nu_e \to \nu_\mu, \tau$ with an electron neutrino survival probability $\mathrm{P}\left(\nu_e \to \nu_e\right) = 0.55$ [131] and the reduced cross section for ν_μ, τ, the average background rate in the energy range $[1, 12]$ keV is

$$R_{\text{solar}} = (8.9 \pm 0.2)\ (\mathrm{kg} \cdot \mathrm{d} \cdot \mathrm{keV})^{-1}\,. \tag{4.3}$$

The total 2% uncertainty comes from the combination of the uncertainty on the p-p neutrinos flux ($\sim 1\%$), ^{7}Be neutrinos flux ($\sim 10\%$) and the uncertainty on the oscillation parameter $\sin^2\left(2\theta_{12}\right)$ of about 2%.

4.3 ^{136}Xe double beta decay simulation

For the prediction of the ER background in the XENON1T experiment, the two electrons emitted by the double beta decay ($2\nu2\beta$) of ^{136}Xe were initially modeled as a single electron following their total energy spectrum. The spectrum is given by the Primakoff-Rosen approximation [133]:

$$\frac{dN}{dK} \sim K \cdot (Q_{\beta\beta} - K)^5 \cdot \left(1 + 2K + \frac{4}{3}K^2 + \frac{1}{3}K^3 + \frac{1}{30}K^4\right) \tag{4.4}$$

where K is the electrons' total the kinetic energies and $Q_{\beta\beta} = 2458\,\mathrm{keV}$ is the Q-value of the decay, with all quantities expressed in units of electron mass. This model was compared to the total spectrum coming from simulations done with DECAY0 code [134] and the agreement is evident in Fig. 4.11. For low energies, the spectrum can be approximated with the linear expression $(3.5 \cdot \mathrm{E_R}\,[\mathrm{keV}]) \cdot 10^{-7}\ (\mathrm{kg} \cdot \mathrm{d} \cdot \mathrm{keV})^{-1}$ and in the region of interest for WIMP search this means an expected background of about $2.3 \cdot 10^{-6}\ (\mathrm{kg} \cdot \mathrm{d} \cdot \mathrm{keV})^{-1}$.

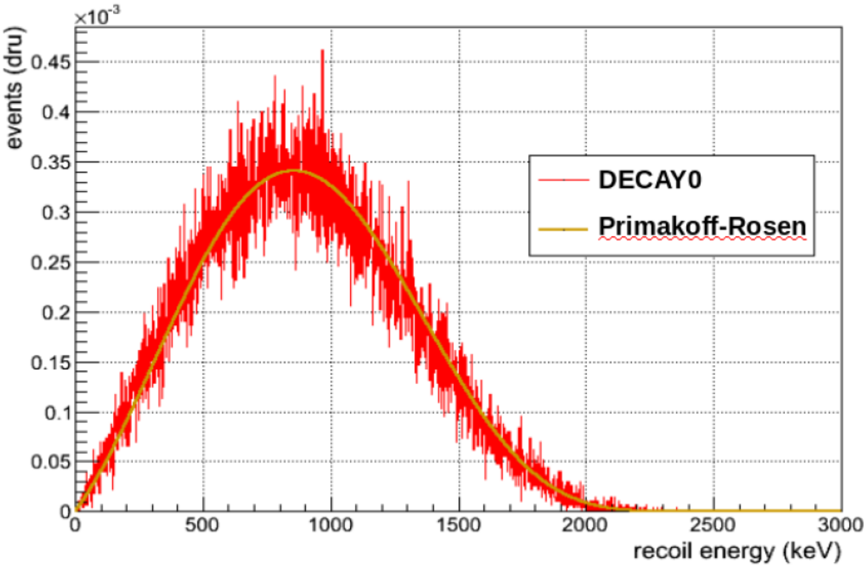

Figure 4.11: Total energy spectrum for $2\nu2\beta$ decay: the dark yellow line represents the Primakoff-Rosen approximation, while the red histogram is a DECAY0 simulation [135].

Modeling the electron pair from $2\nu2\beta$ with a single electron returns the correct energy spectrum: low energy electrons have a mean free path in LXe shorter than 0.1 mm, hence it is impossible to detect a double signal and the contribution from both the particles is summed. However, an higher energy electron has a higher probability to interact with the medium via *bremsstrahlung*, hence emitting a γ ray with a longer mean free path in LXe: for this reason this model may overestimate the fraction of multiple scattering (MS) events. Since the selection of single scatter events is one of the main requirements in matching MC and background data, the actual production of the two electrons is implemented in the simulation, starting from the theoretical calculation of J. Kotila and F. Iachello [136]. They calculated the phase space factor using the exact Dirac wave functions for the emitted electrons, considering both the finite size of the nucleus and the screening effects due to shell electrons.

The simulation is implemented in two steps: at first the directions and the energies of the electrons are generated and stored using a C++ program, then they are used as an input by GEANT4 to generate and propagate these leptons. The electrons' energy is generated following a two-dimensional probability density distribution: this gives the probability for a pair of electrons to be produced with energies $(\mathrm{E}_1, \mathrm{E}_2)$, with the energy conservation constraint $\mathrm{E}_1 + \mathrm{E}_2 \leqslant Q_{\beta\beta}$. Neutrinos are not simulated as their interaction is completely negligible and they are taken into account as a missing energy $\Delta\mathrm{E}_{\nu\nu} = Q_{\beta\beta} - \mathrm{E}_1 - \mathrm{E}_2$. The two-dimensional spectrum has been calculated for almost every double beta emitter [137] and from the phase space factor it was possible to estimate the angular correlation between the direction of the two electrons. The angular correlation factor $\alpha(\mathrm{E}_1)$ is given by the ratio of the phase space factor for electrons in p-wave ($L = 1$) and s-wave ($L = 0$) and it gives the distribution of the angle θ between the directions of the

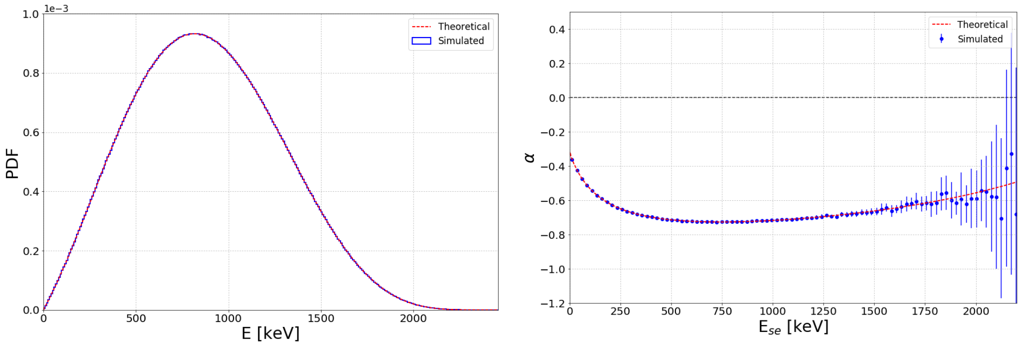

Figure 4.12: Comparison between the generated initial conditions for electrons pairs and the theoretical calculations: the total energy spectrum (left) and the angular correlation (right) are in perfect agreement. This confirms that the initial energies and directions are properly generated.

electrons as a function of the energy of one electron:

$$\frac{dN}{d\cos(\theta)} \propto 1 + \alpha(\mathrm{E}_1) \cdot \cos(\theta) \,. \tag{4.5}$$

For validation purposes a total of 10^7 initial conditions for electrons pairs was simulated using this program: in Figs. 4.12 the theoretical and simulated summed spectrum and angular correlation are shown. The almost perfect agreement confirms the correct simulation of initial conditions for the electrons emitted in the double beta decay of ^{136}Xe.

For each set of initial conditions, the GEANT4 simulation produces a two electrons with the given directions and energies: because of the intrinsic nature of this background the couples are produced homogeneously in the active volume of LXe. The output from GEANT4 simulation is stored in a ROOT file: for each step of each particle the time, deposited energy, energy loss process, position and other variables are saved. The response of the detector is not included in the GEANT4 output, therefore the MC simulation has to be processed in order to reproduce the observed signal and for this purpose a dedicated Python program is used. A single event in the GEANT4 output is divided in several steps: because of the spatial resolution in z of the detector, the deposited energies are clustered if within a z slice with a height dependent on the signal intensity, otherwise they are labeled as multiple scattering (MS) events. The deposited energy in the LXe is converted into photons for scintillation and free charge for ionization: this *emission model* is based on the Thomas-Imel box model [138], particularly suited for short tracks. Assuming that each ion-electron pair is spatially separated (geminate theory), this model describes the emission of free charge and the recombination taking into account the screening effects due to Xenon polarization as a non-null potential only inside a box. Given an initial condition of N_0 units of charge uniformly distributed in a box of dimension a, the final model yields to a collected charge fraction

$$\frac{Q}{Q_0} = \frac{1}{\xi} \ln(1+\xi) \,, \qquad \xi \equiv \frac{N_0 \alpha}{4a^2 u_- E} \tag{4.6}$$

where α is the recombination factor, E the external electric field and u_- the electrons' drift velocity. These parameters are fitted on calibration data using a bayesian approach: the theoretical model represents the prior which is updated using the information coming from calibration data, thus the posterior is the final emission model. Once the deposited energy is converted into emitted light and charge, these need to be corrected to obtain the expected final signals S1 and S2. The light signal needs to be corrected for the

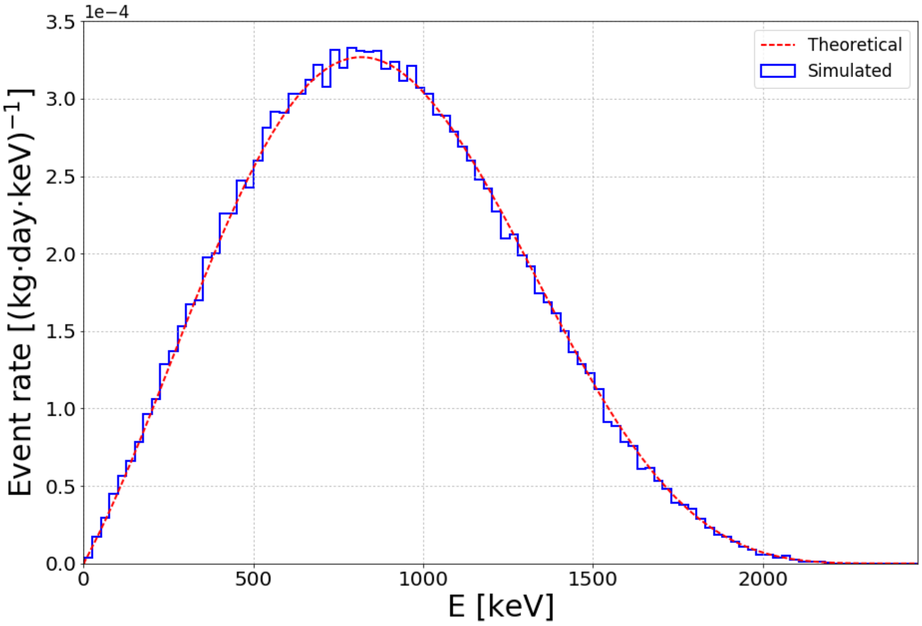

Figure 4.13: Simulated total deposited energy spectrum compared to the theoretical spectrum: after the processing step the agreement is still good. The spectra are normalized to the total expected rate for ^{136}Xe in Eq. (4.2), properly scaled for the single scatters.

light collection efficiency (LCE) map, obtained from ^{83m}Kr calibration data and in good agreement with the simulations of optical photons in the LXe active volume, knowing the characteristics of each PMT. In the same way, the charge signal needs to be corrected both for the light collection efficiency and for the electron lifetime, defined as the average time a drifting electron takes to recombine in LXe.

As the GEANT4 data are processed, the simulation is complete. In Fig. 4.13 the ER background spectrum coming from a simulation of 10^5 ^{136}Xe decays is compared to the theoretical summed spectrum: they are in a perfect agreement with each other. The simulated spectrum is the distribution of the energy deposited by the electronic pair in single scattering events. This last cross-check after the processing stage confirms that the newly implemented double beta decay works properly. Moreover, the implementation of this program is versatile as it simulates a pair of electrons starting from a two-dimensional energy spectrum and an angular correlation dependence. This means that it can be used to simulate every double beta decay emitters as well as neutrinoless double beta decays, just by changing the input spectrum.

The $2\nu2\beta$ simulation using two electrons instead of just one was implemented in order to make it more realistic, especially concerning the MS fraction of events. As the electron mean free path in LXe is lower than 0.1 mm for kinetic energy 100 keV÷1 MeV, MS events cannot be due to the presence of two electrons instead of just one as the distance between the scatters needs to be at least 3 mm to be resolved by XENON1T detector. The multiple scatter comes from the interaction of a γ bremsstrahlung emitted by one of the electrons: γ rays have a longer mean free path in LXe, therefore there is a finite possibility for them to interact 3 mm apart from their production point. Since the bremsstrahlung cross section depends on the electron energy, the γ production probability is different as we consider a single electron with energy E or two electrons with energies E_1 and E_2, where $E_1 + E_2 = E$. This difference is the reason why a simulation using two electrons instead of an energetic one is more realistic: it leads to a better simulation of the multiple scattering probability. The comparison of 10^5 double beta decays with the old and new simulations shows that multiple scattering events represents (2.81 ± 0.05) % of the total when the decay is simulated using a single electron, while this fraction becomes almost half when two electrons are considered: (1.57 ± 0.04) %. The hypothesis of bremsstrahlung as primary cause of multiple scattering is confirmed by the fact that the totality of simulated MS events, produced both with a single electron and an electron pair, involves the production of a bremsstrahlung γ ray. Fig. 4.14 shows the spectra for single and multiple scatter events and for events presenting the emission of a γ via bremsstrahlung, both for the new implementation (solid line) and the old one (dashed line). While the single scatter spectrum is almost identical for the simulations, the multiple scattering spectrum for the old implementation is higher than for the new one using electronic pairs. Similarly, the events presenting bremsstrahlung are characterized by a higher event rate when the simulation is done with single electrons than with electron pairs. Moreover, the MS and bremsstrahlung spectra have similar trend as additional hint to their correlation, but the former class of events is a subset of the latter: every MS event presents a bremmstrahlung creation process, but this does not imply that the production of a γ ray via bremsstrahlung leads to a multiple scattering event, as the photon can be absorbed within 3 mm from its origin.

4.4 MC/data matching

As XENON1T has been running for more than a year, a comparison between the MC simulations and the real background data is possible as the statistics

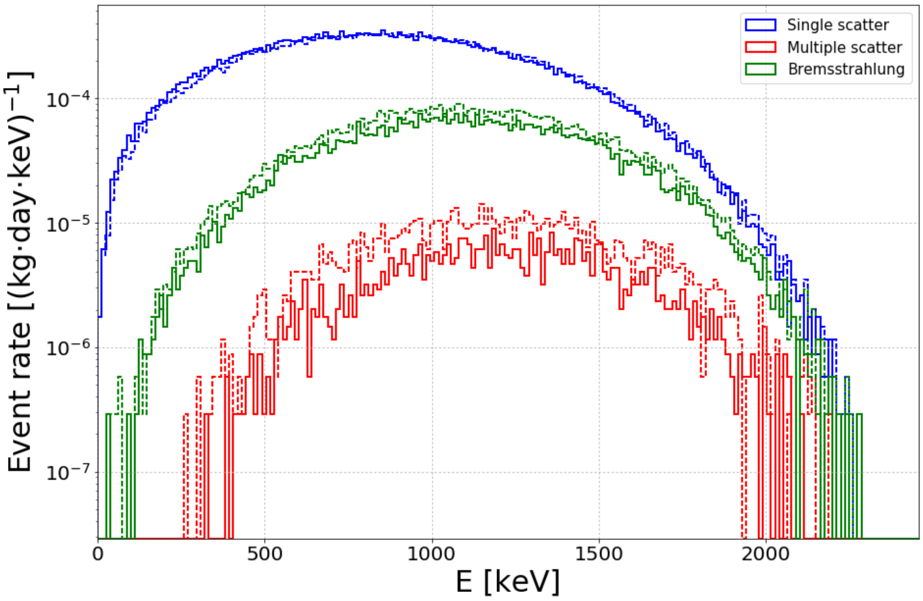

Figure 4.14: Comparison between the implementation of the $2\nu2\beta$ decay using a single electron (dashed line) and two electrons (solid lines). The difference is almost null for the spectrum of single scatter events, but it is systematically higher for the old implementation (single electron) as MS and bremsstrahlung events are taken into account. All the spectra are normalized for Eq. (4.2) and scaled for the single scatter, MS or bremsstrahlung ratio of events.

coming from the data taking is high enough. Understanding the ER background spectrum and its origin in XENON1T improves our knowledge of the detector. This is a fundamental requirement for WIMP search, but also for other rare event search like neutrinoless double beta decay or double electron capture.

A preliminary match of the MC simulation with the real background data has been recently performed: first MC simulations from each possible source have been produced, then the simulated spectrum and the background have been matched using the χ^2 minimizing framework based on MINUIT [139]. The very preliminary results are briefly presented at the end of the section.

4.4.1 MC simulations production

In order to match the entire ER background spectrum it is necessary to simulate every single contributing source: beside the already discussed intrinsic radioisotopes (^{85}Kr, ^{222}Rn, ^{136}Xe), solar neutrinos and materials' contamination, also activated isotopes and calibration sources need to be taken into account. Indeed, as the total ER background spectrum is integrated over the entire exposure time, activated Xenon lines and the residual contribution after calibration operations (e.g. ^{83m}Kr at 41 keV) are an important contribution to the entire spectrum, especially for energies lower than about 500 keV. The final MC simulated spectra are obtained after several steps:

1. primary interactions, like decaying nuclei or scattering neutrinos, are homogeneously simulated with GEANT4 version 9.5.p01 in the considered volume and material;
2. the GEANT4 output is processed as described in Section 4.3 to reproduce the detector response to the deposited particles' energy;
3. the processed simulated spectrum does not include the energy resolution of the detector and it has to be introduced by smearing;
4. before matching with the real background data the spectra are normalized to a reference value, which could be a unitary value or the expected one (e.g. for solar neutrinos 4.3), then only the single scatter events are considered.

The materials' radioactive contamination has been simulated for materials contributing the most to the total background. Following the study in [79], the main contribution to ER background coming from materials' radioactivity is due to six components:

- Cryostat shells and flanges, made of SS;
- Copper field shaping rings;
- PTFE components of the TPC, like pillars, panels or the PMTs array holder structure;
- PMTs;
- PMT bases;
- SS components of the TPC, i.e. diving bell and electrode rings.

They have been implemented in GEANT4 as described in Section 4.1. The leading long-lived radioisotope contributing to the radioactivity of these materials are:

- ^{60}Co decaying β^+ into an excited state of ^{60}Ni, which could emit γ rays with energy 1173 keV and 1332 keV;

- ^{40}K decaying via electron capture (BR=10.72%) into an excited state of ^{40}Ar, followed by the emission of a 1461 keV γ ray;

- ^{137}Cs decaying β^- into an excited state of ^{137}Ba followed up by a γ ray at 662 keV emitted for de-excitation;

- ^{238}U radioactive chain, divided into two parts to take into account disequilibrium (^{238}U → ^{230}Th and ^{226}Ra → ^{206}Pb);

- ^{232}Th radioactive chain, divided into two parts as the Uranium series: ^{232}Th → ^{228}Ac and ^{228}Th → ^{208}Pb;

- ^{235}U radioactive chain, simulated as a single chain since its activity is negligible compared to ^{238}U.

Intrinsic sources represent the dominant ER background in the fiducial volume. As they are intrinsic, the events should be generated in the total amount of Xenon inside the cryostat. Since the active volume is 2/3 of the total Xenon, less than 70% of the events generated is expected to be in the active volume: this requires a more time-consuming simulation in order to have high statistics, as only events entering the active volume are stored. In order to save CPU power and time, some sources were generated only in the active volume inside the TPC, as the contribution to the event rate coming from the events generated outside the detector is negligible. To decide whether this contribution could be neglected or not, a set of 10^4 events for each possible source was generated in the total amount of Xenon: if the fraction of stored events generated outside the TPC is lower than the arbitrary threshold 0.2%, then this source can be generated only in the active volume. Results from these simulations are shown in Fig. 4.15, where the events generated outside the TPC and stored are marked in red. In general, sources with higher energy γ's are more likely to have a non-negligible fraction of events in the active volume coming from the Xenon outside the TPC.

The simulated intrinsic background sources are:

- recoiling electron from solar neutrinos scattering off them following the spectrum in Fig. 4.10b and generated only inside the active volume the events, as they consist of recoiling electrons with a mean free path too short to enter the TPC from outside;

- ^{85}Kr;

- ^{136}Xe;

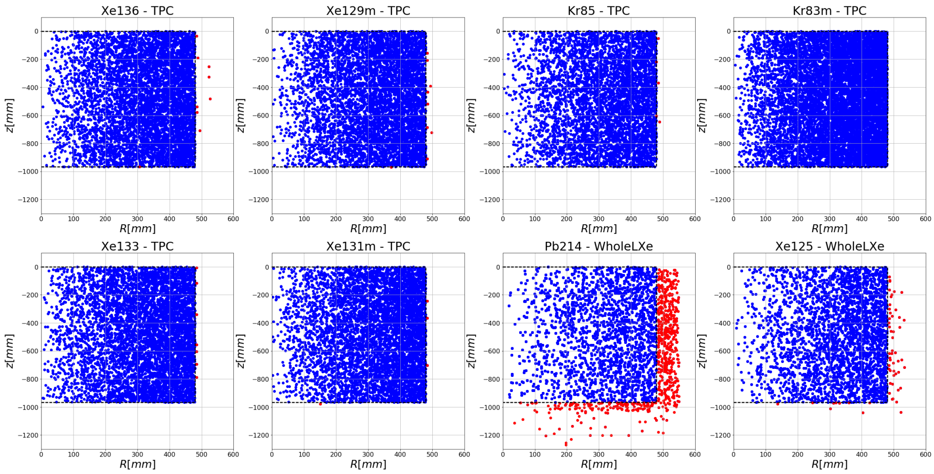

Figure 4.15: Initial position of 10^4 events generated in the total volume of LXe and entering the TPC. The blue points represent events generated inside the TPC and red points outside the TPC: if the fraction of these events is higher than 0.2% the total MC simulation is generated in the whole LXe (the simulation volume is in the title).

- ^{214}Pb instead of the entire ^{222}Rn decay chain. This is the only daughter which could lead to a background in the energy spectrum below 3 MeV, as all the others decay α or they are coupled to α emission, with an energy higher than 5 MeV;
- radioactive Xenon isotopes generated because of nuclear reactions of neutrons with Xe nuclei, ^{133}Xe and ^{125}Xe.

Other intrinsic sources are not listed because they have not been fitted to simulated data: ^{83m}Kr and neutron activated isomers ^{129m}Xe and ^{131m}Xe are modeled and fitted to real data as a Gaussian distribution. This is due to the fact that the low energy γ ($E_\gamma \lesssim 500\,\text{keV}$) are less likely to Compton scatter, therefore they can be well modeled by a smeared absorption line, i.e. a Gaussian distribution. The ^{83m}Kr contribution has to be simulated with two Gaussian distributions, with mean energies 41.6 keV and 32.2 keV. Indeed, the metastable state of the Krypton decays into the ground state in a two step process, emitting a 32.2 keV γ ray and a 9.4 keV one after a mean time interval of about 155 ns: both the events produce a light and charge signal. The S2 signals are always merged into a single one because of their width, but the two S1s may be reconstructed as a single merged signal or as two resolved signals. In the first and most common case, a single event with a total energy of 41.6 keV is reconstructed, while in the second case only the biggest S1 signal is considered, hence a 32.2 keV event is reconstructed.

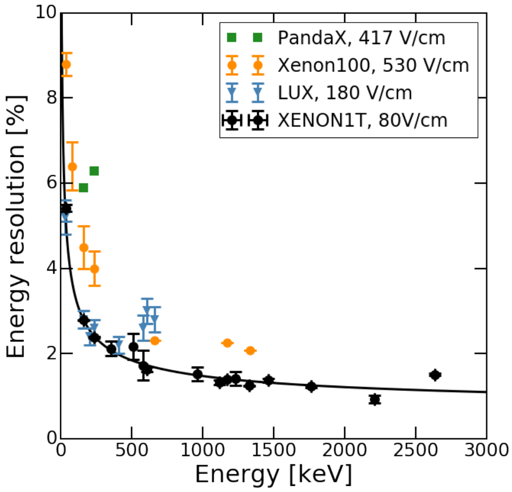

Figure 4.16: Combined energy resolution for different γ-lines in the XENON1T detector compared to other double-phase XeTPC experiments. The solid line is the best fit for the dependence in Eq. (4.7).

The processed spectra have been smeared based on the energy resolution measured from the peaks of the real background data. A comparison of the energy resolution from different double phase TPC for dark matter search is shown in Fig. 4.16. The final energy resolution can be expressed as

$$\frac{\sigma_E}{E} = \frac{a}{\sqrt{E}} + b, \tag{4.7}$$

where $a = (28.26 \pm 0.28)$ keV$^{\frac{1}{2}}$ and $b = 0.58 \pm 0.02$.

Eventually, the smeared spectra have been normalized; the background spectra from materials' activity have been normalized to a specific activity of 1 mBq/kg (or 1 mBq/item for PMTs), while for intrinsic sources the normalization was:

- 1 μBq/kg for all Xenon isotopes, ^{83m}Xe and ^{214}Pb;
- 4.12 μBq/kg for ^{136}Xe as expected from Eq. (4.2);
- $1.875 \cdot 10^{-5}$ mBq/kg for ^{85}Kr at a concentration of 0.1 ppt;
- $8.9 \cdot 10^{-6}$ mBq/kg for solar neutrino as discussed in Section 4.2.3.

4.4.2 Matching method and preliminary results

The matching of MC simulations with real background data is carried out by minimizing the χ^2 using the Python library iMinuit. The working principle is the same exploited in Section 3.3.2 for the "combined spectra matching": finding the best scaling parameters for each background contributor activity

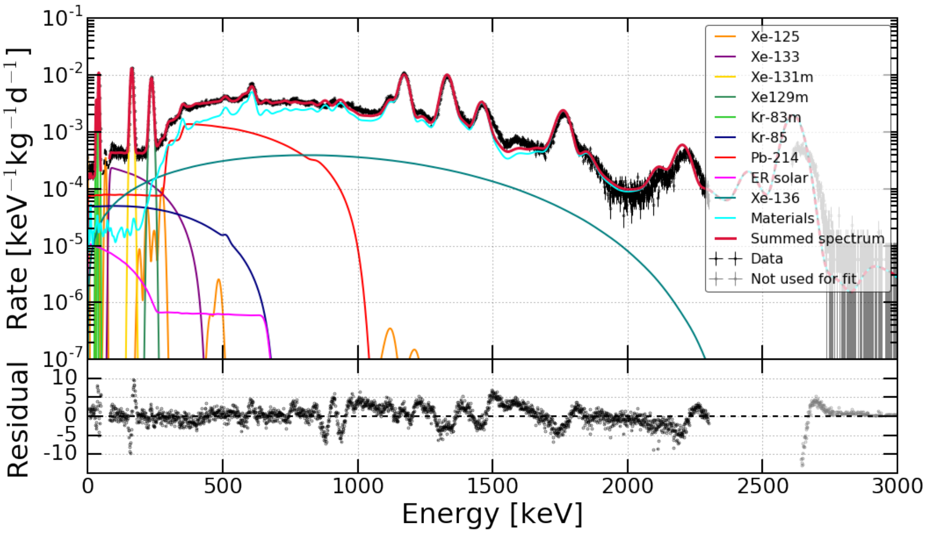

Figure 4.17: Matching of MC simulated spectra and real background data up to 2300 keV.

and minimizing its difference with the real data. The total simulated spectrum is given by the sum of each contribution coming from the material i and source j (including intrinsic sources):

$$R_{\mathrm{MC}}\left(E\right)=\sum_{i}^{\text{materials}}\sum_{j}^{\text{sources}}a_{i,j}\cdot R_{i,j}^{\mathrm{MC}}\left(E\right), \tag{4.8}$$

where the spectra $R_{i,j}^{\mathrm{MC}}\left(E\right)$ are properly normalized. The χ^2 function is

$$\chi^{2}=\sum_{\varepsilon}\frac{\left(R\left(\varepsilon\right)-R_{\mathrm{MC}}\left(\varepsilon\right)\right)^{2}}{\sigma_{R}\left(\varepsilon\right)^{2}}, \tag{4.9}$$

where $R\left(\varepsilon\right)$ is the measured spectrum in the energy bin ε with a statistical uncertainty $\sigma_R\left(\varepsilon\right)$. As every single bin of the spectrum has a number of entries $\mathrm{N}_\varepsilon \gg 1$, the χ^2 value follows the χ^2 distribution

$$f\left(z;N\right)=\frac{z^{N/2-1}}{2^{N/2}\Gamma\left(N/2\right)}e^{-z/2} \tag{4.10}$$

where the number of degrees of freedom (ndf) is given by the total number of bins minus the number of parameters to be fitted and $\Gamma\left(\mathrm{n}\right)$ is the Gamma function.

The total number of free parameters is equivalent to the total activities to be estimated by matching the MC data to the real background: considering 6

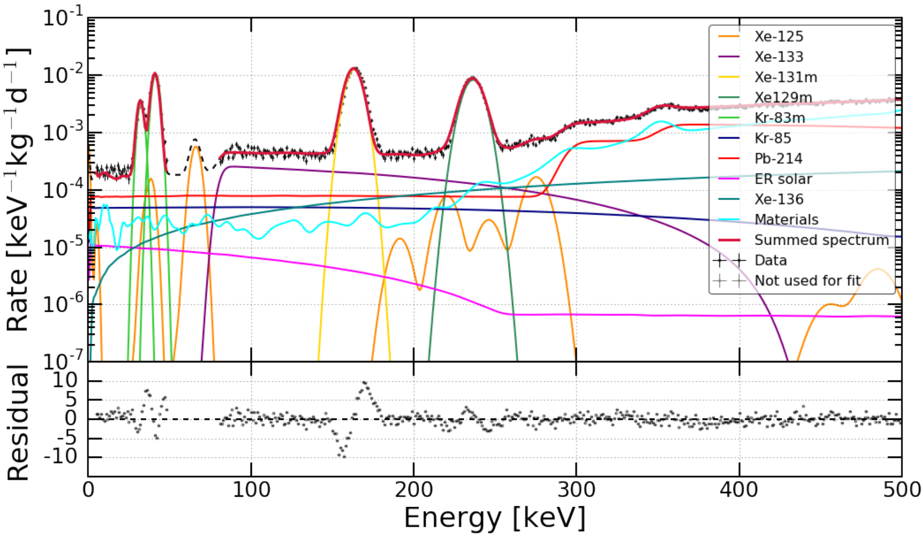

Figure 4.18: Matching of MC simulated spectra and real background data up to 500 keV.

detector components for 8 materials' radioisotopes and the 9 intrinsic sources, the total number of parameters is 57. Since minimizing a function with 57 free parameters is a challenging problem also for a powerful tool like Minuit, it is necessary to reduce this number and to constrain them. Using the contamination of the materials measured during the screening campaign and used for the MC prediction of the background [79], the ratio of the activities between materials for each isotopes can be fixed. This means that the number of free parameters for materials' radioactivity is lowered by a factor 6, since the ratio between different materials is fixed: this leads to a total number of 17 free parameters.

Additional constraints for some background sources are given by independent background studies or assumptions:

- the contamination of ^{85}Kr can vary in the two sigma region around the average measured concentration 0.45 ± 0.07 ppt, as shown in Fig. 4.7;
- the solar neutrino expected rate is fixed;
- the activity of ^{136}Xe is allowed to deviate 20% from the expected rate in Eq. (4.2);
- upper and lower limits for ^{214}Pb come from the parent ^{222}Rn activity $14.0 \pm 0.1\,\mu$Bq/kg and the BiPo[2] activity $5.6 \pm 0.1\mu$Bq/kg, coming from

---

[2] The β^- decay of ^{214}Bi and the α decay of its daughter ^{214}Po are delayed by a mean

the measurements reported in Fig. 4.8.

The real data used for matching are background data from February to October 2017. The energy ranges $[50, 80]$ keV and $[2300, 2600]$ keV are blinded and they have to be excluded from the matching: these are the energy intervals for the search of the double electron capture of ^{124}Xe and the neutrinoless double beta decay of ^{136}Xe. The high energy blinding region is close to the ^{208}Tl and ^{214}Bi lines, hence the lack of these data worsens the matching for the second part of the Thorium and, especially, Uranium radioactive chains (see Section 3.3.2). Moreover, since for higher energies the energy reconstruction worsens and the fit diverges, the matching is performed only up to 2300 keV. For the lower limit of the matching a threshold of 5 keV is considered.

The preliminary results of the matching are shown in Fig. 4.17: the fit yields to $\chi^2/ndf \approx 4$ and especially at higher energies the spectrum is not well matched anymore. The matching for lower energies is shown in Fig. 4.18. Nevertheless, a good agreement between the simulations and the real data is shown and it is one of the best matching for this kind of experiment [140, 141]. The residuals, in units of standard deviations, show sharp wiggles in coincidence with some peaks: this could be explained by a poor matching of their mean energy and to a shift of the simulated and reconstructed peaks. Moreover, for low energies the materials' simulations present wiggles which are supposed to be due to their statistics which is not high enough.

The major improvements for the matching and the next steps towards a final understanding of the ER background spectrum are: increasing the statistics of materials' simulations, simulating ^{129m}Xe and ^{131m}Xe to take into account the Compton contribution and exploiting the spatial and temporal information by simultaneously matching the spectrum in different volumes and studying the evolution over time of the activated lines. Moreover, an additional improvement is using Markov chains Monte Carlo (MCMC) bayesian approach instead of the least squares method, in order to let the parameters free using the screening information to set the priors.

---

time interval of $163.6\,\mu$s, therefore they can be identified with almost 100% efficiency thanks to this delayed coincidence technique.

Conclusions

After the first science run with an exposure time of 34.2 live days, XENON1T confirmed its leadership among the Dark Matter direct search experiments thanks to its tonne-scale LXe target and the lowest background ever recorded in this type of experiments. It sets the most stringent exclusion limit on the SI WIMP-nucleon elastic scattering cross section of $7.7 \cdot 10^{-47}\,\mathrm{cm}^2$, for a WIMP mass of $m_\chi = 35\,\mathrm{GeV/c^2}$, at 90% confidence level. The new results from the second science run, related to a total exposure time of more than 250 live days, will be shown by Spring 2018.

In parallel with the data analysis for the running experiment, the XENON collaboration is working on the realization of the next phase of the project, XENONnT. A fast-paced upgrade is possible as most of the subsystems of XENON1T, as the cryogenic and purification systems, were designed to work properly also with a larger TPC. The target mass will be about 6 t of LXe and it will have an expected sensitivity for SI WIMP-nucleon interaction cross sections down to $1.6 \cdot 10^{-48}\,\mathrm{cm}^2$ for a WIMP mass of $50\,\mathrm{GeV/c^2}$, an order of magnitude lower than the projection from the full exposure ($2\,\mathrm{t} \cdot \mathrm{y}$) of the current experiment.

Because of its low background, XENON1T is extremely sensitive to any possible background source both of ER and NR events, where the latter are more dangerous as they mimic the signal expected for a WIMP scattering off a Xe nucleus. During the latest science run, a D-D fusion neutron generator was employed as source for NR calibration and it was located inside the water tank close to the cryostat during few months, both for tests and for NR calibration operations. The radioactive contaminants in the NG materials may represent a background source, both for low energy ER and NR events. That possibility was excluded by studying the contribution of the NG to the total spectrum: it was possible by considering the difference between the spectrum when the NG was placed inside the water tank and when it was not. The difference is given by the ER spectrum induced by the NG and for low energies its differential event rate in the 1 t fiducial volume is

$$(0.1 \pm 1.7_{\mathrm{stat}}) \cdot 10^{-5}\,(\mathrm{kg} \cdot \mathrm{d} \cdot \mathrm{keV})^{-1}\,.$$

Therefore, the ER background induced by the NG can be neglected in the 1 t FV and it is negligible for larger fiducial volumes with a radius up to about 44.8 cm.

The radiogenic neutrons emitted due to the contamination of ^{238}U and ^{232}Th in the materials of the NG can be dangerous background for the WIMP search. In order to estimate the rate of radiogenic neutron events coming from the NG, the activities for Uranium and Thorium were estimated by matching the MC simulations with the high energy lines of γ rays from ^{208}Tl and ^{214}Bi of the NG spectrum. Then, it was possible to estimate the NR event rate from NG simulating the neutron emission accordingly to the measured activities ($A_{\mathrm{Th}} = (2.30 \pm 0.08_{\mathrm{stat}})$ Bq and $A_{\mathrm{U}} = (4.06 \pm 0.21_{\mathrm{stat}})$ Bq). Considering secular equilibrium for the radioactive series, the final event rate in the 1 t fiducial volume is

$$(7.7 \pm 0.4_{\mathrm{stat}} \pm 1.3_{\mathrm{sys}}) \cdot 10^{-4}\,\mathrm{events/year},$$

more than two orders of magnitude lower than the predicted NR event rate for radiogenic neutrons coming from the other materials near the detector. The NR background induced by the NG can be neglected in the entire active volume and this is true also by taking into account a possible disequilibrium in the worst-case scenario.

As almost 280 live days of data have been collected, it is possible to match the real data with the MC simulations in order to better understand the background of XENON1T. A new simulation for the double beta decay intrinsic emitter ^{136}Xe was developed, generating a pair of electrons instead of a single energetic electron: this improved the multiple scattering simulation. After a massive production of MC simulations, the preliminary results for the comparison between MC and real data were obtained: this is the first step towards the complete knowledge of the background sources of the XENON1T detector.

Appendix A

Charge Yield evolution

Monitoring the stability over time of the signals of the XENON1T detector, an evolution over time of the proportional signal S2 has been observed throughout the entire Science Run 1, from February 2017 up to January 2018. This is observed as a increase of the charge yield (CY), i.e. the number of proportional photons detected per unit of deposited energy, over the entire exposure. As the origin and energy of a peak is well known, like the 41.6 keV line from ^{83m}Kr, it is possible to calculate the CY for that specific energy as

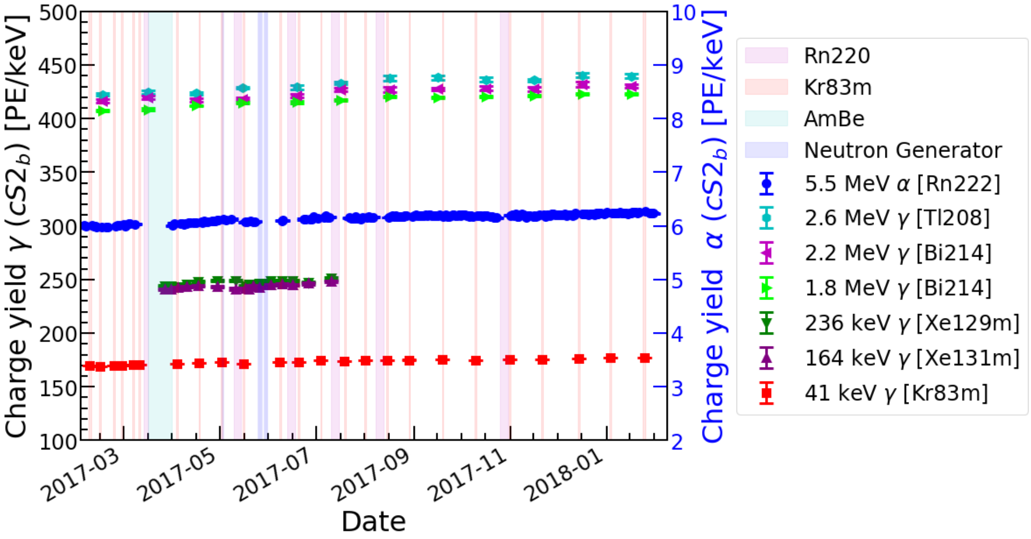

Figure A.1: Charge yield evolution over the entire SR1 exposure time for several sources.

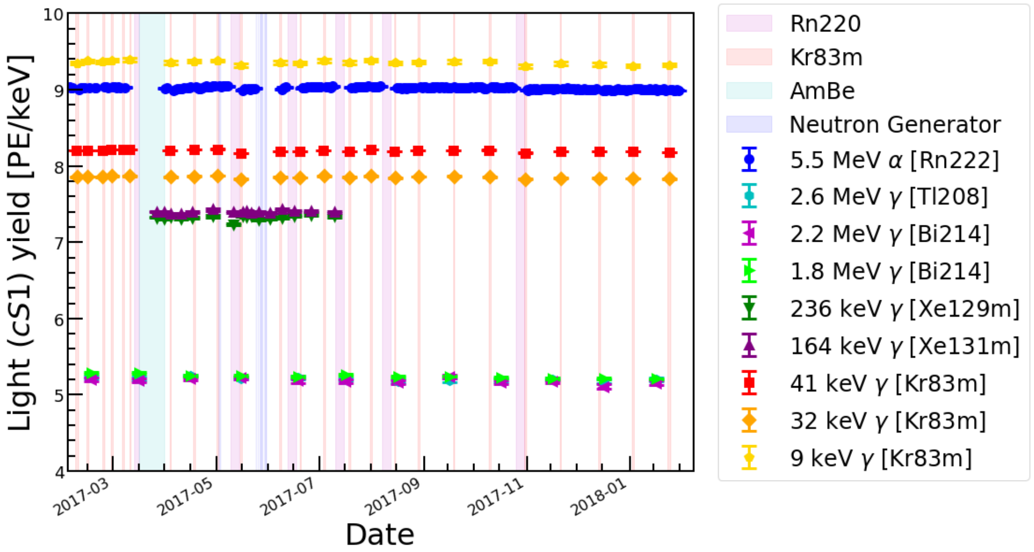

Figure A.2: Light yield evolution over the entire SR1 exposure time for several sources.

the ratio of the S2 signal over the energy:

$$\mathrm{CY}\left(E\right) = \frac{\mathrm{cS2_{bot}}\left(E\right)}{E}, \tag{A.1}$$

where the proportional signal is corrected for the light collection efficiency and for the electron lifetime and only the fraction collected by the bottom array is used.

In Fig. A.1 the charge yield evolution is plotted for several sources spanning a wide range of energy and S2:

- low energy γ rays from ^{83m}Kr;
- activation lines from ^{129m}Xe and ^{131m}Xe, fitted only for few months after NG calibration runs (NG and AmBe) as their activity decayed exponentially with a half-life of the order of 10 days;
- high energy γ rays coming from ^{208}Tl and ^{214}Bi, subject of study in the following;
- the 5.5 MeV α particles from the decay of ^{222}Rn.

The origin of this evolution has not been yet fully understood, but several hypotheses are under investigation. The deviation from the mean is within

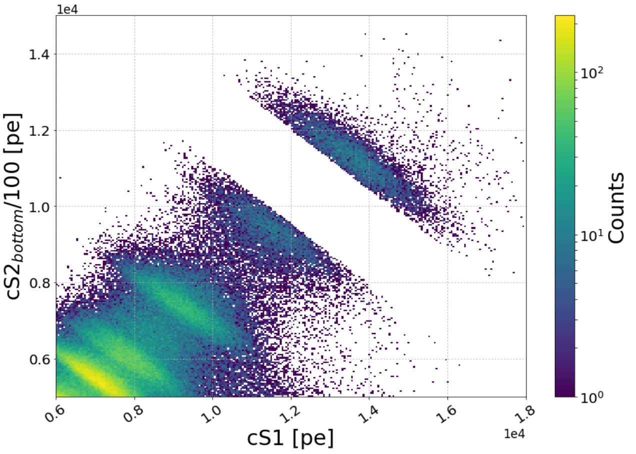

Figure A.3: Distribution in the $(\mathrm{cS1}, \mathrm{cS2_b})$ space of SR1 single scatter events in the 1 t FV. The missing population is blinded because of the $0\nu2\beta$ search.

±2% for all sources used to monitor the CY. The impact of this small deviations on the definition of the ER band was found to be negligible, thus the effect on the WIMP search analysis is null.

Next to the evolution of the CY, the light yield (LY) is stable at the $\sim 0.2\%$ level over time for all the mentioned sources: in addition to them, the signal S1 can be studied also for the very low energy considering the reconstructed single X rays from ^{83m}Kr decay (9.4 keV and 32.2 keV). The LY is given by the ratio of the corrected prompt S1 signal over the deposited energy:

$$\mathrm{LY}\,(E) = \frac{\mathrm{cS1}\,(E)}{E}. \tag{A.2}$$

The stability over time of the light yield is shown in Fig. A.2.

A.1 CY from high energy gammas

The ^{208}Tl and ^{214}Bi lines coming from the materials' radioactivity give useful information about the detector response to high energy gammas. Using them, the stability of CY and LY over time can be monitored month by month as their rate of events is $\mathcal{O}\left(10\,\mathrm{day}^{-1}\cdot\mathrm{ton}^{-1}\right)$, not as high as for ^{222}Rn, which allows a daily monitoring. The data used for this analysis are single scatter events inside a 1 t fiducial volume, selected from the SR1 Dark Matter search data. The deposited energy by each γ ray is well known and the corrected S1 and S2 are defined by fitting the Gaussian ellipsoids given by the normal distribution of both the S1 and S2 signals around their mean values. The ellipsoids are tilted since the signals are anti-correlated as described in Chapter 2. This property can be seen in Fig. A.3: the missing population is due to the blinding for the search for $0\nu2\beta$ decay of ^{136}Xe. Each gamma line is

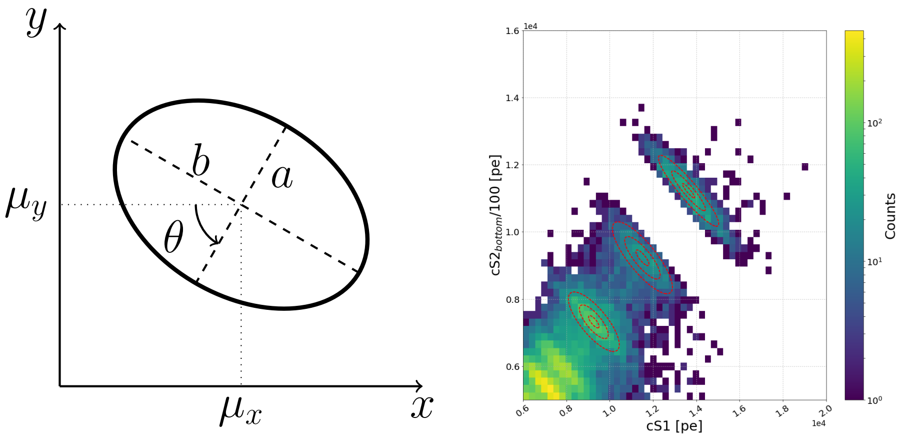

(a) **(b)**

Figure A.4: (a) Geometrical meaning of the parameters in (Eq. A.3). (b) Bivariate gaussian fit of the May dataset: the contour lines represents 95%, 68% and 30% of the maximum value.

fitted with a bivariate normal distribution

$$\begin{aligned}\mathcal{N}(x,y) = A\cdot\exp\Bigg\{ &-\left[\frac{(x-\mu_x)\cos\theta+(y-\mu_y)\sin\theta}{a}\right]^2 + \\ &-\left[\frac{(y-\mu_y)\cos\theta-(x-\mu_x)\sin\theta}{b}\right]^2\Bigg\} + k,\end{aligned} \tag{A.3}$$

where A is a normalization factor, k a background constant factor, μ_i is the mean value, θ is the ellipsoid rotation angle and a and b are the major and minor axes, from which σ_x and σ_y are calculated.

An example of fitting is shown in Fig. A.4b: the blinded region may reduce the information for the fit of both the 2614 keV ^{208}Tl and the 2204 keV ^{214}Bi lines, but yet robust results are achieved. Fitting month by month each line it is possible to obtain the evolution of LY and CY for the three high energy γ sources. The 1σ deviation from the mean value is shown in Tab. A.1.

$\mathbf{E}_\gamma$	1σ **LY deviation**	1σ **CY deviation**
1764 keV	0.50%	1.22%
2204 keV	0.62%	1.23%
2614 keV	0.40%	1.46%

Table A.1: Relative deviation of 1σ from the mean values of LY and CY for the high energy gamma sources.

Bibliography

[1] F. Zwicky. Die Rotverschiebung von extragalaktischen Nebeln. *Helvetica Physica Acta*, 6:110–127, 1933.

[2] H. Poincaré. The Milky Way and the Theory of Gases. *Popular Astronomy*, 14:475–488, October 1906.

[3] W.T. Kelvin. *Baltimore lectures on molecular dynamics and the wave theory of light*. C.J. Clay and Sons, 1904.

[4] R. Kippenhahn. *Bound to the sun: the story of planets, moons, and comets*. New York: W.H. Freeman, 1990.

[5] F. Zwicky. On the Masses of Nebulae and of Clusters of Nebulae. *Astrophys. J.*, 86:217, October 1937.

[6] R.H. Sanders. *The Dark Matter Problem: A Historical Perspective*. Cambridge University Press, 2010.

[7] M. S. Roberts. A High-Resolution 21-CM Hydrogen-Line Survey of the Andromeda Nebula. *Astrophys. J.*, 144:639, May 1966.

[8] M. S. Roberts and R. N. Whitehurst. The rotation curve and geometry of M31 at large galactocentric distances. *Astrophys. J.*, 201:327–346, October 1975.

[9] V. C. Rubin and W. K. Ford, Jr. Rotation of the Andromeda Nebula from a Spectroscopic Survey of Emission Regions. *Astrophys. J.*, 159:379, February 1970.

[10] J. P. Ostriker and P. J. E. Peebles. A Numerical Study of the Stability of Flattened Galaxies: or, can Cold Galaxies Survive? *Astrophys. J.*, 186:467–480, December 1973.

[11] W. J. Quirk. Numerical Experiments in Spiral Structure. II. *Astrophys. J.*, 167:7, July 1971.

[12] J. F. Navarro, C. S. Frenk, and S. D. M. White. The Structure of Cold Dark Matter Halos. *Astrophys. J.*, 462:563, May 1996.

[13] D. Clowe, M. Bradač, A. H. Gonzalez, M. Markevitch, S. W. Randall, C. Jones, and D. Zaritsky. A Direct Empirical Proof of the Existence of Dark Matter. *Astrophys. J., Lett.*, 648:L109–L113, September 2006.

[14] C. Mastropietro and A. Burkert. Simulating the Bullet Cluster. *Mon. Not. R. Astron. Soc.*, 389:967–988, September 2008.

[15] A. A. Penzias and R. W. Wilson. A Measurement of Excess Antenna Temperature at 4080 Mc/s. *Astrophys. J.*, 142:419–421, July 1965.

[16] D. J. Fixsen. The Temperature of the Cosmic Microwave Background. *Astrophys. J.*, 707:916–920, December 2009.

[17] R. K. Sachs and A. M. Wolfe. Perturbations of a Cosmological Model and Angular Variations of the Microwave Background. *Astrophys. J.*, 147:73, January 1967.

[18] Planck Collaboration, N. Aghanim, M. Arnaud, M. Ashdown, J. Aumont, C. Baccigalupi, A. J. Banday, R. B. Barreiro, J. G. Bartlett, N. Bartolo, and et al. Planck 2015 results. XI. CMB power spectra, likelihoods, and robustness of parameters. *Astron. Astrophys.*, 594:A11, September 2016.

[19] Planck Collaboration, P. A. R. Ade, N. Aghanim, M. Arnaud, M. Ashdown, J. Aumont, C. Baccigalupi, A. J. Banday, R. B. Barreiro, J. G. Bartlett, and et al. Planck 2015 results. XIII. Cosmological parameters. *Astron. Astrophys.*, 594:A13, September 2016.

[20] E. Hubble. A Relation between Distance and Radial Velocity among Extra-Galactic Nebulae. *Proceedings of the National Academy of Science*, 15:168–173, March 1929.

[21] M. Milgrom. A modification of the Newtonian dynamics as a possible alternative to the hidden mass hypothesis. *Astrophys. J.*, 270:365–370, July 1983.

[22] M. Milgrom. A Modification of the Newtonian Dynamics - Implications for Galaxy Systems. *Astrophys. J.*, 270:384, July 1983.

[23] M. Milgrom. A modification of the Newtonian dynamics - Implications for galaxies. *Astrophys. J.*, 270:371–389, July 1983.

[24] J. D. Bekenstein. Relativistic gravitation theory for the modified Newtonian dynamics paradigm. *Phys. Rev. D*, 70(8):083509, October 2004.

[25] S. Capozziello and M. de Laurentis. Extended Theories of Gravity. *Phys. Rep.*, 509:167–321, December 2011.

[26] E. Verlinde. On the origin of gravity and the laws of Newton. *Journal of High Energy Physics*, 4:29, April 2011.

[27] M. M. Brouwer, Visser, et al. First test of Verlinde's theory of emergent gravity using weak gravitational lensing measurements. *Mon. Not. R. Astron. Soc.*, 466:2547–2559, April 2017.

[28] B. P. Abbott et al. GW170817: Observation of Gravitational Waves from a Binary Neutron Star Inspiral. *Phys. Rev. Lett.*, 119(16):161101, 2017.

[29] B. P. Abbott, R. Abbott, T. D. Abbott, F. Acernese, K. Ackley, C. Adams, T. Adams, P. Addesso, R. X. Adhikari, V. B. Adya, and et al. Multi-messenger Observations of a Binary Neutron Star Merger. *Astrophys. J., Lett.*, 848:L12, October 2017.

[30] S. Boran, S. Desai, E. O. Kahya, and R. P. Woodard. GW170817 Falsifies Dark Matter Emulators. *Phys. Rev. D*, 97(4):041501, 2018.

[31] Esteban Roulet Silvia Mollerach. *Gravitational lensing and microlensing*. World Scientific, 2002.

[32] EROS-2 Collaboration. Limits on the Macho content of the Galactic Halo from the EROS-2 Survey of the Magellanic Clouds. *Astron. Astrophys.*, 469:387–404, July 2007.

[33] I. B. Zeldovich. The theory of the large scale structure of the universe. In M. S. Longair and J. Einasto, editors, *Large Scale Structures in the Universe*, volume 79 of *IAU Symposium*, pages 409–420, 1978.

[34] R. Cowsik and J. McClelland. Gravity of Neutrinos of Nonzero Mass in Astrophysics. *Astrophys. J.*, 180:7–10, February 1973.

[35] A. S. Szalay and G. Marx. Neutrino rest mass from cosmology. *Astron. Astrophys.*, 49:437–441, June 1976.

[36] V. Springel, S. D. M. White, et al. Simulations of the formation, evolution and clustering of galaxies and quasars. *Nature*, 435:629–636, June 2005.

[37] S. Dodelson and L. M. Widrow. Sterile neutrinos as dark matter. *Phys. Rev. Lett.*, 72:17–20, January 1994.

[38] F. Muller, R. W. Birge, W. B. Fowler, R. H. Good, W. Hirsch, R. P. Matsen, L. Oswald, W. M. Powell, H. S. White, and O. Piccioni. Regeneration and Mass Difference of Neutral K Mesons. *Phys. Rev. Lett.*, 4:418–421, April 1960.

[39] R. J. Crewther, P. di Vecchia, G. Veneziano, and E. Witten. Chiral estimate of the electric dipole moment of the neutron in quantum chromodynamics. *Phys. Lett. B*, 88:123–127, December 1979.

[40] J. M. Pendlebury et al. Revised experimental upper limit on the electric dipole moment of the neutron. *Phys. Rev. D*, 92(9):092003, November 2015.

[41] R. D. Peccei and H. R. Quinn. CP conservation in the presence of pseudoparticles. *Phys. Rev. Lett.*, 38:1440–1443, June 1977.

[42] W. A. Bardeen and S.-H. H. Tye. Current algebra applied to properties of the light Higgs boson. *Phys. Lett. B*, 74:229–232, April 1978.

[43] V. Anastassopoulos, S. Aune, et al. New CAST limit on the axion-photon interaction. *Nature Physics*, 13:584–590, June 2017.

[44] The XENON100 Collaboration. First Axion Results from the XENON100 Experiment. *Phys. Rev. D*, 90(6):062009, 2014. [Erratum: Phys. Rev.D95,no.2,029904(2017)].

[45] I. Aitchison. *Supersymmetry in Particle Physics: An Elementary Introduction.* Cambridge University Press, 2007.

[46] G. Jungman, M. Kamionkowski, and K. Griest. Supersymmetric dark matter. *Phys. Rep.*, 267:195–373, March 1996.

[47] Super-Kamiokande Collaboration. Search for proton decay via $p \to e^+\pi^0$ and $p \to \mu^+\pi^0$ in 0.31 megaton · years exposure of the super-kamiokande water cherenkov detector. *Phys. Rev. D*, 95:012004, Jan 2017.

[48] J. Ellis, T. Falk, and K. A. Olive. Neutralino-stau coannihilation and the cosmological upper limit on the mass of the lightest supersymmetric particle. *Phys. Lett. B*, 444:367–372, December 1998.

[49] Gianfranco Bertone. *Particle dark matter: observations, models and searches.* Cambridge Univ. Press, Cambridge, 2010.

[50] G. Jungman, M. Kamionkowski, and K. Griest. Supersymmetric dark matter. *Phys. Rep.*, 267:195–373, March 1996.

[51] G. Bertone, D. Hooper, and J. Silk. Particle dark matter: evidence, candidates and constraints. *Phys. Rep.*, 405:279–390, January 2005.

[52] K. Griest and M. Kamionkowski. Unitarity limits on the mass and radius of dark-matter particles. *Phys. Rev. Lett.*, 64:615–618, February 1990.

[53] P. Blasi, R. Dick, and E. W. Kolb. Ultra-high energy cosmic rays from annihilation of superheavy dark matter. *Astropart. Phys.*, 18:57–66, August 2002.

[54] Theodor Kaluza. Zum unitätsproblem in der physik. *Sitzungsber. Preuss. Akad. Wiss. Berlin (Math. Phys.)*, page 966, 1921.

[55] M. G. Aartsen and M. et al. Ackermann. Search for annihilating dark matter in the Sun with 3 years of IceCube data. *European Physical Journal C*, 77:146, March 2017.

[56] M. G. Aartsen and M. et al. Ackermann. The IceCube Neutrino Observatory: instrumentation and online systems. *Journal of Instrumentation*, 12:P03012, March 2017.

[57] Super-Kamiokande Collaboration. The Super-Kamiokande detector. *Nucl. Instrum. Methods Phys. Res., Sect. A*, 501:418–462, April 2003.

[58] Super-Kamiokande Collaboration. Search for neutrinos from annihilation of captured low-mass dark matter particles in the Sun by Super-Kamiokande. *Phys. Rev. Lett.*, 114(14):141301, 2015.

[59] L. Bergström and H. Snellman. Observable monochromatic photons from cosmic photino annihilation. *Phys. Rev. D*, 37:3737–3741, June 1988.

[60] W. B. et al. Atwood. The Large Area Telescope on the Fermi Gamma-Ray Space Telescope Mission. *Astrophys. J.*, 697:1071–1102, June 2009.

[61] The Fermi LAT Collaboration. Limits on dark matter annihilation signals from the Fermi LAT 4-year measurement of the isotropic gamma-ray background. *J. Cosm. Astropart. Phys.*, 9:008, September 2015.

[62] W. Menn et al. The pamela space experiment. *Advances in Space Research*, 51(2):209 – 218, 2013. The Origins of Cosmic Rays: Resolving Hess's Century-Old Puzzle.

[63] O. et al. Adriani. An anomalous positron abundance in cosmic rays with energies 1.5-100GeV. *Nature*, 458:607–609, April 2009.

[64] D. Hooper, I. Cholis, T. Linden, and K. Fang. HAWC observations strongly favor pulsar interpretations of the cosmic-ray positron excess. *Phys. Rev. D*, 96(10):103013, November 2017.

[65] L. et al. Accardo. High statistics measurement of the positron fraction in primary cosmic rays of 0.5˘500 gev with the alpha magnetic spectrometer on the international space station. *Phys. Rev. Lett.*, 113:121102, Sep 2014.

[66] Cristina Consolandi. Precision Measurement of the Proton Flux in Primary Cosmic Rays from 1 GV to 1.8 TV with the Alpha Magnetic Spectrometer on the International Space Station. In *25th European Cosmic Ray Symposium (ECRS 2016) Turin, Italy, September 04-09, 2016*, 2016.

[67] R. Strauss et al. A detector module with highly efficient surface-alpha event rejection operated in CRESST-II Phase 2. *Eur. Phys. J. C*, 75:352, August 2015.

[68] F. Petricca et al. First results on low-mass dark matter from the CRESST-III experiment. In *15th International Conference on Topics in Astroparticle and Underground Physics (TAUP 2017) Sudbury, Ontario, Canada, July 24-28, 2017*, 2017.

[69] E. Armengaud et al. Performance of the EDELWEISS-III experiment for direct dark matter searches. *Journal of Instrumentation*, 12(08):P08010, 2017.

[70] E. Armengaud et al. Constraints on low-mass WIMPs from the EDELWEISS-III dark matter search. *J. Cosm. Astropart. Phys.*, 1605(05):019, 2016.

[71] D. S. Akerib et al. The Large Underground Xenon (LUX) Experiment. *Nucl. Instrum. Meth.*, A704:111–126, 2013.

[72] D. S. Akerib et al. Results from a search for dark matter in the complete LUX exposure. *Phys. Rev. Lett.*, 118(2):021303, 2017.

[73] P. Agnes et al. Direct Search for Dark Matter with DarkSide. *J. Phys. Conf. Ser.*, 650(1):012006, 2015.

[74] P. Agnes et al. Results from the first use of low radioactivity argon in a dark matter search. *Phys. Rev. D*, 93(8):081101, 2016. [Addendum: Phys. Rev.D95,no.6,069901(2017)].

[75] R. Bernabei et al. DAMA/LIBRA results and perspectives. *Bled Workshops Phys.*, 17(2):1–7, 2016. [EPJ Web Conf.13,60500(2017)].

[76] E. Aprile et al. Search for Event Rate Modulation in XENON100 Electronic Recoil Data. *Phys. Rev. Lett.*, 115(9):091302, 2015.

[77] E. Aprile et al. The XENON1T Dark Matter Experiment. *Eur. Phys. J. C*, 77(12):881, 2017.

[78] XiGuang Cao et al. PandaX: A Liquid Xenon Dark Matter Experiment at CJPL. *Sci. China Phys. Mech. Astron.*, 57:1476–1494, 2014.

[79] E. Aprile et al. Physics reach of the XENON1T dark matter experiment. *J. Cosm. Astropart. Phys.*, 1604(04):027, 2016.

[80] Luis W. Alvarez. Physics notes. Lawrence Radiation Laboratory, 672 (unpublished), 1968.

[81] E. Aprile and T. Doke. Liquid Xenon Detectors for Particle Physics and Astrophysics. *Rev. Mod. Phys.*, 82:2053–2097, 2010.

[82] R.L. Platzman. Total ionization in gases by high-energy particles: An appraisal of our understanding. *Int. J. Appl. Rad. Iso.*, 10(2):116 – 127, 1961.

[83] E. Aprile, A. Bolotnikov, D. Chen, and R. Mukherjee. W. *Phys. Rev. A*, 48:1313–1318, Aug 1993.

[84] E. Aprile, C. E. Dahl, L. DeViveiros, R. Gaitskell, K. L. Giboni, J. Kwong, P. Majewski, Kaixuan Ni, T. Shutt, and M. Yamashita. Simultaneous measurement of ionization and scintillation from nuclear recoils in liquid xenon as target for a dark matter experiment. *Phys. Rev. Lett.*, 97:081302, 2006.

[85] J Lindhard, M Scharff, and HE Schiott. K. danske vidensk selskab., mat. *Fys Medd*, 31:1, 1963.

[86] L. S. Miller, S. Howe, and W. E. Spear. Charge Transport in Solid and Liquid Ar, Kr, and Xe. *Phys. Rev.*, 166:871–878, 1968.

[87] T Doke. Fundamental properties of liquid argon, krypton and xenon as radiation detector media. *Portugal. Phys.*, 12(1-2):9–48, 1981.

[88] Eido Shibamura, Akira Hitachi, Tadayoshi Doke, Tan Takahashi, Shinzou Kubota, and Mitsuhiro Miyajima. Drift velocities of electrons, saturation characteristics of ionization and W-values for conversion electrons in liquid argon, liquid argon-gas mixtures and liquid xenon. *Nucl. Instrum. Meth.*, 131:249–258, 1975.

[89] O. Hilt and W. F. Schmidt. Positive hole mobility in liquid xenon. *J. Chem. Phys.*, 183:147–153, May 1994.

[90] Stephen E. Derenzo, Terry S. Mast, Haim Zaklad, and Richard A. Muller. Electron avalanche in liquid xenon. *Phys. Rev. A*, 9:2582–2591, Jun 1974.

[91] S. Kubota, M. Hishida, and J. Raun. Evidence for a triplet state of the self-trapped exciton states in liquid argon, krypton and xenon. *J. Phys. C*, 11:2645–2651, June 1978.

[92] Shinzou Kubota, Masahiko Hishida, Masayo Suzuki, and Jian-zhi Ruan(Gen. Dynamical behavior of free electrons in the recombination process in liquid argon, krypton, and xenon. *Phys. Rev. B*, 20(8):3486, 1979.

[93] G.F. Knoll. *Radiation Detection and Measurement.* Wiley, 2000.

[94] A. Hitachi. Properties of liquid xenon scintillation for dark matter searches. *Astropart. Phys.*, 24:247–256, 2005.

[95] A. Baldini et al. Absorption of scintillation light in a 100 l liquid xenon gamma ray detector and expected detector performance. *Nucl. Instrum. Meth. A*, 545:753–764, 2005.

[96] A. Lansiart, A. Seigneur, J.-L. Moretti, and J.-P. Morucci. Development research on a highly luminous condensed xenon scintillator. *Nucl. Instrum. Meth.*, 135:47–52, May 1976.

[97] Elena Aprile, Aleksey E. Bolotnikov, Alexander I. Bolozdynya, and Tadayoshi Doke. *Elementary Processes Affecting Generation of Signals*, pages 33–105. Wiley-VCH Verlag GmbH & Co. KGaA, 2006.

[98] T. Doke et al. Absolute scintillation yields in liquid argon and xenon for various particles. *Jpn. J. Appl. Phys.*, 41(3R):1538, 2002.

[99] E. Aprile, K. L. Giboni, P. Majewski, K. Ni, and M. Yamashita. Observation of Anti-correlation between Scintillation and Ionization for MeV Gamma-Rays in Liquid Xenon. *Phys. Rev. B*, 76:014115, 2007.

[100] H.O. Back, A. Alton, F. Calaprice, C. Galbiati, A. Goretti, C. Kendziora, B. Loer, D. Montanari, P. Mosteiro, and S. Pordes. Depleted argon from underground sources. *Physics Procedia*, 37:1105 – 1112, 2012. Proceedings of the 2nd International Conference on Technology and Instrumentation in Particle Physics (TIPP 2011).

[101] E. Aprile et al. Signal Yields of keV Electronic Recoils and Their Discrimination from Nuclear Recoils in Liquid Xenon. 2017.

[102] E. Aprile et al. First Dark Matter Search Results from the XENON1T Experiment. *Phys. Rev. Lett.*, 119(18):181301, 2017.

[103] E. Aprile et al. Design and performance of the XENON10 dark matter experiment. *Astroparticle Physics*, 34:679–698, April 2011.

[104] J. Angle et al. First Results from the XENON10 Dark Matter Experiment at the Gran Sasso National Laboratory. *Phys. Rev. Lett.*, 100:021303, 2008.

[105] D. S. Akerib et al. Limits on Spin-Independent Interactions of Weakly Interacting Massive Particles with Nucleons from the Two-Tower Run of the Cryogenic Dark Matter Search. *Phys. Rev. Lett.*, 96:011302, Jan 2006.

[106] J. Angle et al. Limits on Spin-Dependent WIMP-Nucleon Cross Sections from the XENON10 Experiment. *Phys. Rev. Lett.*, 101:091301, Aug 2008.

[107] E. Aprile et al. The XENON100 dark matter experiment. *Astropart. Phys.*, 35:573–590, April 2012.

[108] E. Aprile et al. Dark Matter Results from 225 Live Days of XENON100 Data. *Phys. Rev. Lett.*, 109:181301, 2012.

[109] E. Aprile et al. XENON100 Dark Matter Results from a Combination of 477 Live Days. *Phys. Rev. D*, 94(12):122001, 2016.

[110] T. Haruyama, K. Kasami, H. Nishiguchi, S. Mihara, T. Mori, W. Otani, R. Sawada, Y. Maruno, and T. Nishitani. LN2-free Operation of the MEG Liquid Xenon Calorimeter by using a High-power Pulse Tube Cryocooler. *AIP Conference Proceedings*, 823(1):1695–1702, 2006.

[111] E. Aprile et al. Conceptual design and simulation of a water Cherenkov muon veto for the XENON1T experiment. *Journal of Instrumentation*, 9:P11006, 2014.

[112] M. Aglietta et al. Muon “depth-intensity” relation measured by the LVD underground experiment and cosmic-ray muon spectrum at sea level. *Phys. Rev. D*, 58:092005, Oct 1998.

[113] W.R. Leo. *Techniques for Nuclear and Particle Physics Experiments: A How-to Approach.* Springer, 1994.

[114] E. Aprile et al. Response of the XENON100 Dark Matter Detector to Nuclear Recoils. *Phys. Rev. D*, 88:012006, 2013.

[115] R. F. Lang, J. Pienaar, E. Hogenbirk, D. Masson, R. Nolte, A. Zimbal, S. Röttger, M. L. Benabderrahmane, and G. Bruno. Characterization of a deuterium–deuterium plasma fusion neutron generator. *Nucl. Instrum. Meth. A*, 879:31–38, 2018.

[116] S. Westerdale and P. D. Meyers. Radiogenic Neutron Yield Calculations for Low-Background Experiments. *Nucl. Instrum. Meth. A*, 875:57–64, 2017.

[117] S. Agostinelli et al. GEANT4: A Simulation toolkit. *Nucl. Instrum. Meth. A*, 506:250–303, 2003.

[118] Peter Diehl. Wise uranium project.

[119] D.G. Madland, E.D. Arthur, G.P. Estes, J.E. Stewart, M. Bozoian, R.T. Perry, T.A. Parish, T.H. Brown, T.R. England, W.B. Wilson, and W.S. Charlton. Sources 4a: A code for calculating (alpha,n), spontaneous fission, and delayed neutron sources and spectra. *tech. rep.*, Los Alamos(LA-13639), 9 1999.

[120] E. Aprile et al. Material radioassay and selection for the XENON1T dark matter experiment. *Eur. Phys. J. C*, 77(12):890, 2017.

[121] K. Lung et al. Characterization of the Hamamatsu R11410-10 3-Inch Photomultiplier Tube for Liquid Xenon Dark Matter Direct Detection Experiments. *Nucl. Instrum. Meth. A*, 696:32–39, 2012.

[122] E. Aprile et al. Lowering the radioactivity of the photomultiplier tubes for the XENON1T dark matter experiment. *Eur. Phys. J. C*, 75(11):546, 2015.

[123] Evaluated nuclear structure data. `http://www.nndc.bnl.gov/ensdf/`, Feb 2018.

[124] Credit/citations for data files distributed with geant4. `http://www.http://geant4.cern.ch/support/datafiles_origin.shtml`, Dec 2015.

[125] L. Baudis, A. D. Ferella, A. Askin, J. Angle, E. Aprile, T. Bruch, A. Kish, M. Laubenstein, A. Manalaysay, T. Marrodán Undagoitia, and M. Schumann. Gator: a low-background counting facility at the Gran Sasso Underground Laboratory. *Journal of Instrumentation*, 6:8010, August 2011.

[126] Turkevich, Anthony and Winsberg, Lester and Flotow, Howard and M. Adams, Richard. The radioactivity of atmospheric krypton in 1949-1950. 94:7807–10, 08 1997.

[127] K. Winger, J. Feichter, M.B. Kalinowski, H. Sartorius, and C. Schlosser. A new compilation of the atmospheric 85krypton inventories from 1945 to 2000 and its evaluation in a global transport model. *Journal of Environmental Radioactivity*, 80(2):183 – 215, 2005.

[128] X. Du, K. Bailey, Z.-T. Lu, P. Mueller, T. P. O'Connor, and L. Young. An atom trap system for practical ^{81}Kr dating. *Rev. Sci. Instrum.*, 75:3224–3232, October 2004.

[129] Marc Weber. *Gentle Neutron Signals and Noble Background in the XENON100 Dark Matter Search Experiment*. PhD thesis, Heidelberg U., 2013.

[130] J. B. Albert et al. Improved measurement of the $2\nu\beta\beta$ half-life of ^{136}Xe with the EXO-200 detector. *Phys. Rev. C*, 89(1):015502, 2014.

[131] C. Patrignani et al. Review of Particle Physics. *Chin. Phys.*, C40(10):100001, 2016.

[132] Aldo M. Serenelli, W. C. Haxton, and Carlos Pena-Garay. Solar models with accretion. I. Application to the solar abundance problem. *Sov. Phys. – JETP*, 743:24, 2011.

[133] F. Boehm and P. Vogel. *Physics of Massive Neutrinos.* Cambridge University Press, 1992.

[134] O. A. Ponkratenko, V. I. Tretyak, and Yu. G. Zdesenko. The Event generator DECAY4 for simulation of double beta processes and decay of radioactive nuclei. *Phys. Atom. Nucl.*, 63:1282–1287, 2000. [Yad. Fiz.63,1355(2000)].

[135] Fabio Valerio Massoli. *The XENON1T experiment: Monte Carlo background estimation and sensitivity curves study.* PhD thesis, alma, Febbraio 2015.

[136] J. Kotila and F. Iachello. Phase space factors for double-β decay. *Phys. Rev. C*, 85:034316, 2012.

[137] Double beta decay phase-space factors. `https://nucleartheory.yale.edu/double-beta-decay-phase-space-factors`.

[138] J. Thomas and D. A. Imel. Recombination of electron-ion pairs in liquid argon and liquid xenon. *Phys. Rev. A*, 36:614–616, Jul 1987.

[139] F. James and M. Roos. Minuit: A System for Function Minimization and Analysis of the Parameter Errors and Correlations. *Comput. Phys. Commun.*, 10:343–367, 1975.

[140] D. S. Akerib et al. Radiogenic and Muon-Induced Backgrounds in the LUX Dark Matter Detector. *Astropart. Phys.*, 62:33–46, 2015.

[141] E. Aprile et al. Study of the electromagnetic background in the XENON100 experiment. *Phys. Rev. D*, 83(8):082001, April 2011.